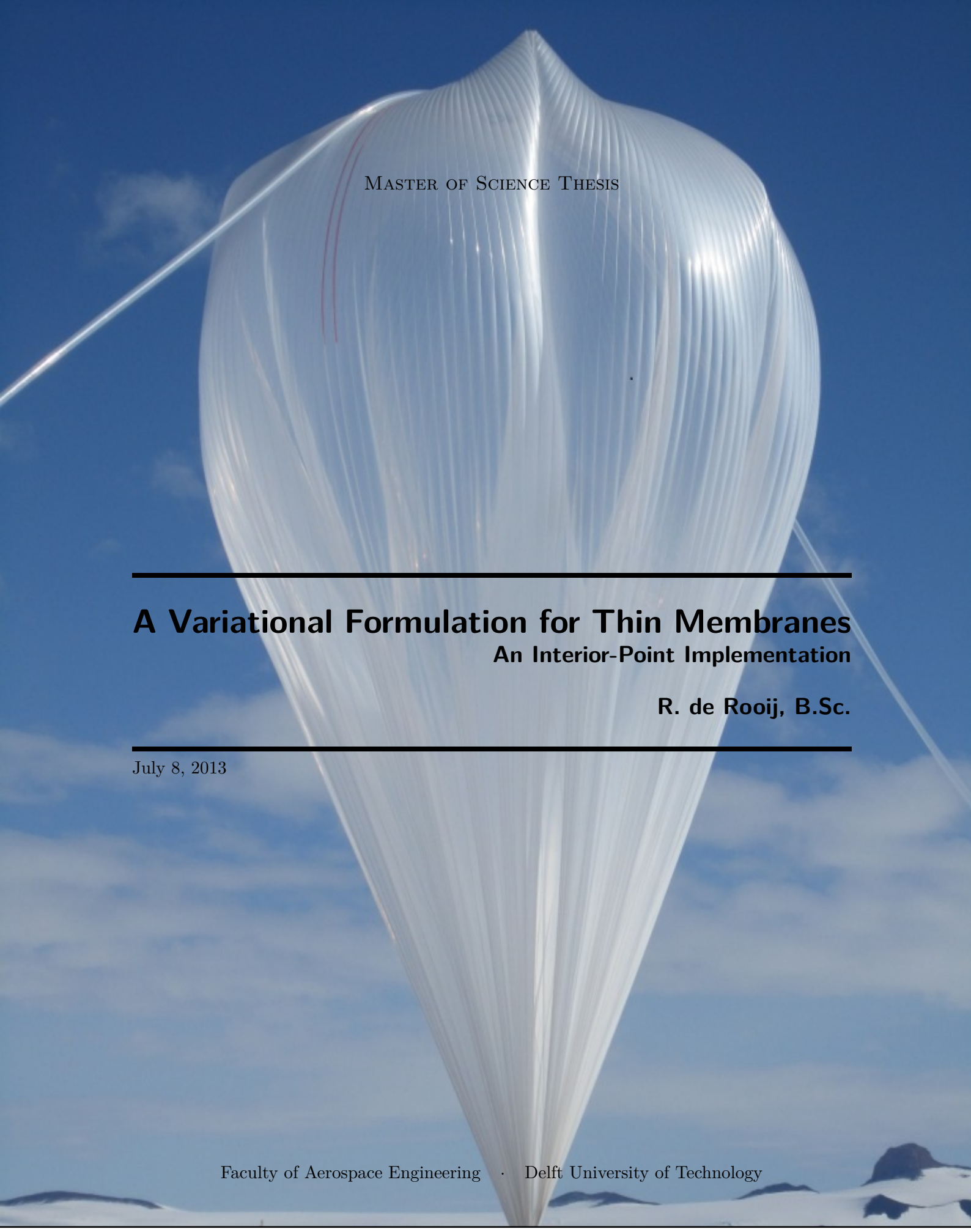

Master of Science Thesis

A Variational Formulation for Thin Membranes

An Interior-Point Implementation

R. de Rooij, B.Sc.

July 8, 2013

Faculty of Aerospace Engineering · Delft University of Technology

TU Delft Delft University of Technology

A Variational Formulation for Thin Membranes

An Interior-Point Implementation

Master of Science Thesis

For obtaining the degree of Master of Science in Aerospace Engineering
at Delft University of Technology

R. de Rooij, B.Sc.

July 8, 2013

Faculty of Aerospace Engineering · Delft University of Technology



Copyright © R. de Rooij, B.Sc.
All rights reserved.

Delft University of Technology
Department of
Aerospace Structures and Materials

The undersigned hereby certify that they have read and recommend to the Faculty of Aerospace Engineering for acceptance a thesis entitled

A Variational Formulation for Thin Membranes

by

R. de Rooij, B.Sc.

in partial fulfillment of the requirements for the degree of

Master of Science

Dated: July 8, 2013

Supervisor(s):

Dr. M.M. Abdalla

Reader(s):

Dr. S.R. Turteltaub

Dr. F. Cirak

Summary

Membranes are applied in a large variety of structures such as atmospheric balloons and parachutes. One can even find these thin foils at a cellular level in humans where they protect the cells from their environment. Membranes are applied in structural applications because of their high flexibility and low mass to surface ratio. A limitation of membranes is that they are restricted to carrying tensile loads only, as they wrinkle under the slightest compressive load. As these wrinkles affect the load carrying capabilities of the membrane it is important to model the stress distribution in the membrane accurately to assess these capabilities. To be able to model these wrinkles, the mesh size in a numerical model needs to be at least as small as the wrinkles to detect them. Considering the small scale of the wrinkles with respect to the membrane as a whole, this requirement often results in unacceptably high computational costs.

This issue can be solved by modeling the wrinkles as a continuous in-plane contraction of the membrane, this is known as the tension field theory method. Pipkin [24, 25] in his work incorporates this method into the theory of finite deformations by defining a relaxed strain energy function. The work discussed in this thesis is based on this relaxed strain energy and an investigation of whether a variational formulation of the relaxed strain energy function can be used to obtain a robust and efficient method to model the stress distribution in membranes in the presence of wrinkles. The variational formulation was developed first, then it was tested, verified and validated using different numerical examples. The efficiency and robustness of the method arises from the mathematical properties of the formulation and the numerical results.

In order to obtain the variational formulation of the relaxed strain energy function, first several mathematical preliminaries were considered. This included tensor analysis in arbitrary coordinate frames, for which the distinction between covariance and contravariance of components and basis vectors was established. The transformation of the stress and strain tensor between different coordinate frames was derived based on this distinction. Several aspects of convexity analysis were also considered. Different kinds of convexity listed from strong to weak are pure convexity, quasi-convexity and rank-one convexity. Quasi-convexity of the strain energy function with respect to the membrane deformation was required to ob-

tain a stable minimization of the total potential energy. Sufficient conditions for this type of convexity are seen in a convex and non-decreasing strain energy as function of the the strain tensor and a necessary condition is a non-decreasing strain energy. The latter condition states that a positive stress tensor is required to have a stable energy minimization. When assuming a convex strain energy as a function of the strain tensor, it was shown that the relaxed strain energy function resulted in the required quasi-convexity for a stable energy minimization. The relaxed strain energy was obtained by a relaxation of the known strain energy function. In the mathematical preliminaries a definition of this relaxation is presented and proven to be the lower, convex and non-decreasing envelope of the strain energy function.

Next, the kinematics of the membranes were considered to find the relation between the displacement of the membranes and the strains. In the tension field theory method the wrinkling of the membrane is modeled as an in-plane contraction, which means that when describing the kinematics of the membrane only the corresponding strain effects need to be considered. The strain-displacement is derived and used to define the Green-Lagrange strain tensor. This relationship between strains and displacements is presented in convected coordinates using the Voigt notation of engineering stresses and strains.

The mathematical preliminaries and kinematic relations of a membrane are required to formulate the equilibrium conditions of this membrane under applied loading. In order to determine these conditions first the three different membrane states must be presented: taut, wrinkled and slack. When the membrane is taut both principal stresses are positive and the membrane behaves as a regular shell. The slack state is characterized by a purely compressive deformation, which corresponds to zero stresses in the membrane. For a wrinkled membrane one principal stress is positive whereas the other equals zero. The wrinkles occur along this zero stress direction.

The equilibrium conditions for a membrane are obtained from a minimization of total potential energy which includes the relaxed strain energy. This relaxed strain energy in itself is an optimization problem in which the stress tensor is constrained to be positive definite everywhere in the membrane. As constrained optimization problems are inherently difficult to solve, the interior point method is applied to replace the constraint with a barrier function which approaches zero when the constrained is satisfied and infinity is elsewhere. The barrier function contains a penalty parameter which represents the extent to which the solution is affected by the barrier function. This penalty parameter approaches zero in the limit. By minimizing the total potential energy in the membrane using the variational principle, three governing equations are obtained which uniquely describe displacement of the membrane as well as the stresses and strains in the membrane. The three possible states of the membrane are implicit in the governing equations and do not need to be obtained by an $if-else$ statement.

The three governing equations are highly non-linear and defined on the global level of the membrane structure. For this reason the membrane structure is discretized into finite elements and the equations are linearized. This process results in the updates for the displacements, stresses and strains for a given non-converged configuration. The updates for displacements are computed on a global level by constructing and assembling the individual contributions of each elements. The updates for the stresses and strains are applied to every integration point in the finite element model separately.

The numerical implementation of the three governing equations is performed using the interior point method. First a step size is introduced for updates of the wrinkling strains and stresses in the membrane. This step size is computed for each integration point separately and ensures that the constraints on the wrinkling strain and stress tensor remain satisfied.

The interior point method also describes an efficient algorithm to drive the penalty parameter of the, earlier mentioned, barrier function to zero. This includes a predictor-corrector update in the solution algorithm. Both in the predictor and corrector the penalty parameter is multiplied by a centering parameter which drives its value to zero.

In order to start up the numerical algorithm first the wrinkling stresses and strains need to be initialized to be a positive definite tensor to satisfy their constraints. Any positive definite tensor suffices in a mathematical sense, but to obtain an efficient algorithm the initialization is performed carefully. For this purpose the stresses in the membrane are computed as if the membrane is a regular shell structure. The resulting positive stresses are directly used as stress initialization in the membrane, whereas the negative stresses are transformed to the positive regime by adding a multiple of the unity tensor. These modified stresses are then used as initialization in the membrane.

Applying the numerical implementation of the governing equations finally requires the finite elements. The triangular and quadrilateral isoparametric elements are presented. In the standard formulation of the quadrilateral element membrane locking occurs due to in-plane bending modes in the strains ands stresses. To alleviate this problem a modified hybrid quardrilateral element was developed based on the Hu-Washizu variational principle. Subsequently the isogeometric finite elemensts were introduced, based on the representation of the initial configuration of the membrane by NURBS basis functions, which were directly applied to the finite element analysis. Important advantages of these basis functions are their polynomial order which can be increased relatively easily and the continuity of their derivatives over the elements. The latter characteristic is equivalent to a continuous stress distribution in the membrane.

Several numerical examples were used to assess, verify and validate the performance of the proposed method. This included a rectangular membrane strip with applied shear/tension displacement loading. The induced stress field was relatively complex as stress singularities occur in the membrane. Verification of the method was performed using an analytical solution for the stress field and convergence was proven using the energy norm of the error. The cut-off level of the error was relatively high, however, a first order rate of convergence was observed.

Validation of the method was performed using an inflatable membrane beam under bending displacement. The load-deflection curve agrees well with experimental data, although wrinkling occurred at a slightly lower applied loading in the numerical model. This is a result of the main assumption of zero bending stiffness of the membrane.

Despite this underestimation of the bending stiffness of the membrane and difficulties in representing highly slacked membrane regions, the numerical results and mathematical characteristics of the governing equations show that the proposed method is both efficient and robust. Only low computational costs are required to model the stress distribution in the membrane in the presence of wrinkles accurately.

Table of Contents

Summary i

List of Figures ix

List of Tables xi

List of Symbols xiii

1 Introduction 1

2 Literature Review 3
- 2-1 Analytical Methods . . . 3
- 2-2 Numerical Methods . . . 5
- 2-3 Proposed Method . . . 7

3 Mathematical Preliminaries 9
- 3-1 Tensor Analysis . . . 9
  - 3-1-1 Vectors . . . 9
  - 3-1-2 Tensors . . . 11
- 3-2 Stress and Strain Transformation . . . 12
- 3-3 Convexity Analysis . . . 13
  - 3-3-1 Convexity . . . 13
  - 3-3-2 Rank-One Convexity . . . 14
  - 3-3-3 Quasi-Convexity . . . 14
  - 3-3-4 Conditions for Convexity of Strain Energy . . . 14
- 3-4 Relaxation Formulation . . . 17

4 Membrane Kinematics 21
- 4-1 Strain-Displacement Relation . . . 21
- 4-2 Convected Coordinates . . . 23

5 Membrane Equilibrium **25**
5-1 General Equilibrium Equations . . . 25
5-2 Membrane States . . . 26
5-3 Relaxed Strain Energy Function . . . 27
5-4 Potential Energy Minimization . . . 30
5-5 Discretization and Linearization . . . 31
5-5-1 Discretization . . . 31
5-5-2 Linearization . . . 32
5-6 Hu-Washizu Principle . . . 35
5-7 Constitutive Laws . . . 37

6 Numerical Implementation **39**
6-1 Semidefinite Programming Algorithm . . . 39
6-2 Numerical Algorithm . . . 41

7 Triangular Elements **45**
7-1 2D Elements . . . 45
7-2 3D Elements . . . 47

8 Quadrilateral Elements **49**
8-1 2D Elements . . . 49
8-2 Hybrid Element . . . 51
8-2-1 Consistent Hybrid Element . . . 52
8-2-2 Stress Positiveness . . . 55
8-2-3 Modified Hybrid Element . . . 56
8-3 3D Elements . . . 56

9 Isogeometric Analysis **59**
9-1 B-Spline Basis Functions . . . 59
9-2 NURBS Basis Functions . . . 61
9-3 NURBS Geometries . . . 62
9-4 Finite Element Analysis . . . 64

10 Numerical Results **69**
10-1 Sheared Membrane Strip . . . 69
10-1-1 Isoparametric Analysis . . . 70
10-1-2 Isogeometric Analysis . . . 78
10-2 Annular Ring . . . 79
10-2-1 Isoparametric Analysis . . . 80
10-2-2 Isogeometric Analysis . . . 82
10-3 Annular Square . . . 84
10-4 Sheared Membrane with Hole . . . 85
10-5 Pressurized Beam under Bending . . . 88
10-5-1 Volume Dependent Pressure Loading . . . 88
10-5-2 Beam Model Description . . . 90
10-5-3 Numerical Results . . . 92

11 Conclusions and Recommendations **99**
11-1 Conclusions 99
11-2 Recommendations 101

A Alternative Convexity Analysis **103**
A-1 Hessian Tensor of Strain Energy Function 103
A-2 Convexity Conditions 105
A-2-1 Convexity 105
A-2-2 Rank-One Convexity 106
A-2-3 Quasi-Convexity 106

B Finite Element Matrices **107**
B-1 2D Triangular Elements 107
B-2 2D Quadrilateral Elements 108

C Mansfield Solution **109**

Bibliography **115**

List of Figures

3-1 Sketch of a convex function. 14
3-2 Sketch of two lower envelopes of $f(x)$ 19

5-1 Overview of membrane states: taut, wrinkled and slack [11]. 27
5-2 Membrane wrinkling modeled as in-plane contraction [11]. 27
5-3 Saint-Venant and neo-Hookean material laws. 38

7-1 2D triangular finite element in $\mathbb{R}^2$. 46
7-2 3D triangular finite element in $\mathbb{R}^3$. 47

8-1 2D quadrilateral finite element in different coordinates systems in $\mathbb{R}^3$. 50
8-2 Quadrilateral element in its element coordinate system. 52
8-3 3D quadrilateral finite element in $\mathbb{R}^3$. 57

9-1 B-spline shape functions for $\boldsymbol{\xi}^* = [0, \frac{1}{3}, \frac{2}{3}, 1]$. 61
9-2 Representation of a quarter circle with NURBS. 62
9-3 p-refinement on quarter-circle for $\boldsymbol{\xi}^* = [0, 1]$. 63
9-4 h-refinement on quarter-circle for $p = 2$, $k = 1$. 64
9-5 Isogeometric analysis results for ODE for $\boldsymbol{\xi}^* = [0, \frac{1}{32}, \frac{2}{32}, ..., 1]$, $p = 3$, $k = 2$. . 66
9-6 Convergence analysis for 1D isogeometric finite elements. 67

10-1 Sketch of rectangular membrane strip under displacement loading. 70
10-2 Example meshes of rectangular membrane strip. 72
10-3 Membrane deformation under shear deformation with $a = 50$mm, $L = 100$mm, $u = 15$mm, $v = 0$mm. 72
10-4 Contour plot of first principal stresses σ_1 for two different load cases with $a = 50$mm, $L = 100$mm. 73

10-5 Contour plot of normalized second principal stresses $\sigma_2/\max\{1,\sigma_1\}$ for two different load cases with $a = 50$mm, $L = 100$mm. 74
10-6 States of the membrane under different load cases with $a = 50$mm, $L = 100$mm. 75
10-7 Mesh convergence for rectangular membrane strip with $a = 50$mm, $L = 100$mm. 77
10-8 Contour plot of first principal stresses σ_1 from isogeometric analysis with $p = 2$ and $k = 1$. 78
10-9 Mesh convergence of isogeometric analysis for rectangular membrane strip with $a = 50$mm, $L = 100$mm. 79
10-10 Mesh of annular membrane ring with $R_{out} = 100$mm and $R_{in} = 50$mm. 80
10-11 Deformed configuration of annular ring with first and second principal stresses under axisymmetric loading. 81
10-12 States of the annular membrane ring under axisymmetric loading. 81
10-13 Deformed configuration of annular ring with first and second principal stresses under non-symmetric loading. 82
10-14 Input mesh for isogeometric analysis on quarter annular ring. 83
10-15 Deformed configuration of quarter annular ring with first principal stresses from isogeometric analysis with $p = 2$ and $k = 1$. 83
10-16 Mesh of annular membrane square with $W_{out} = 50$mm and $W_{in} = 17.5$mm. . . 84
10-17 Deformed configuration of annular ring with first and second principal stresses. 85
10-18 Mesh of square membrane with a hole with $W = 100$mm and $R_{in} = 10$mm. . . 86
10-19 Deformed configuration of square membrane with hole with first and second principal stresses under shear deformation with $\gamma = 1/\sqrt{3}$. 87
10-20 First principal stresses and membrane states near the deformed hole. 87
10-21 Sketch of beam model 90
10-22 Mesh of membrane beam with $L = 1000$mm, $r = 50$mm and $t = 0.06$mm. . . . 93
10-23 First and second principal stresses of cylindrical beam under pure pressure loading with $p = 0.02$MPa. 93
10-24 First and second principal stresses of cylindrical beam with $p = 0.02$MPa and a tip deflection of 100mm. 94
10-25 Load deflection curves for cylindrical pressurized membrane beam under bending used for validation of numerical results with experimental data. The beam has $L = 1000$mm, $r = 50$mm and $t = 0.06$mm. 95
10-26 First and second principal stresses of tapered beam with $p = 0.02$MPa and a tip deflection of 100mm. 96
10-27 Load deflection curves for pressurized membrane beam under bending with $p = 0.02$MPa. The cylindrical beam has $L = 1000$mm, $r = 50$mm and $t = 0.06$mm and the tapered beam has $L = 1000$mm, $r_{root} = 56.8$mm and $t = 0.0703$mm. . 96

C-1 Tension ray lines in membrane under shear loading. 109

List of Tables

3-1 Comparison of notations 11

5-1 Overview of the parameter descriptions 28
5-2 Overview of fourth-order stiffness tensors. 33

9-1 Overview of knots vectors $\boldsymbol{\xi}$ for $\boldsymbol{\xi}^* = [0, \frac{1}{3}, \frac{2}{3}, 1]$ and different values of p and k. 60
9-2 Overview of connection between elements and nodes for $\boldsymbol{\xi}^* = [0, \frac{1}{3}, \frac{2}{3}, 1]$, $p = 3$, $k = 2$. 65

10-1 Characteristics of membrane states 75

List of Symbols

Upper Case Symbols

Symbol	Definition
C, $C^{\alpha\beta\gamma\delta}$, $\boldsymbol{C}$	Material stiffness tensor
C^*, $\boldsymbol{C}^*$	Effective membrane stiffness tensor
$\boldsymbol{B}$	Gradient of strain with respect to displacement
$\boldsymbol{E}$, $E_{\alpha\beta}$	Strain tensor
$\hat{\boldsymbol{E}}$	Wrinkling strain tensor
$\tilde{\boldsymbol{E}}$	Slack strain tensor
$\breve{\boldsymbol{E}}$	Assumed train tensor
$\boldsymbol{F}$, F^i_α	Deformation gradient
$\boldsymbol{G}$, G_{ij}	Metric tensor in current configuration
$\boldsymbol{G}_0$, $G_{0\alpha\beta}$	Metric tensor in reference configuration
H	Wrinkling stiffness tensor
H (App. A)	Hessian tensor
$\boldsymbol{J}$	Jacobian matrix
$\boldsymbol{K}_e$	Element stiffness matrix
$\boldsymbol{N}$	Shape function matrix
$N_{i,p}\,((\xi)$ (Ch. 9)	B-spline basis function
$\boldsymbol{P}$, P^α_i	First Piola-Kirchhoff stress tensor
$\boldsymbol{P}_e$ (Ch. 8)	Projection matrix for strains in hybrid element
$\boldsymbol{P}_i$ (Ch. 9)	Control point location
$\boldsymbol{R}_e$	Element residual vector
$R_{i,p}\,((\xi)$ (Ch. 9)	NURBS basis function
$\boldsymbol{S}$, $S^{\alpha\beta}$	Second Piola-Kirchhoff stress tensor
$\boldsymbol{S}$ (Ch. 8)	Projection matrix for in-plane bending modes
$\hat{\boldsymbol{S}}$	Actual Second Piola-Kirchhoff stress in the membrane
$\breve{\boldsymbol{S}}$	Assumed Second Piola-Kirchhoff stress in the membrane

Symbol	Definition
$\boldsymbol{T}$	Transformation matrix for strains
$\boldsymbol{T}_\sigma$	Transformation matrix for stresses
V (Ch. 10-5)	Enclosed volume

Lower Case Symbols

Symbol	Definition
$\boldsymbol{a}_\alpha$	Covariant basis vector in reference configuration
$\boldsymbol{b}$	Body forces applied to the membrane
$\boldsymbol{b}_i$	Covariant basis vector in current configuration
$\boldsymbol{f}$	Force vector applied to the membrane
k	Element connectivity for NURBS basis functions
p	Polynomial order of NURBS basis functions
p (Ch. 10-5)	Pressure
$\boldsymbol{r}$	Position vector
$\boldsymbol{r}_0$	Position vector in reference configuration
t	Thickness of membrane
$\boldsymbol{t}$	Tractions applied to the membrane
$\boldsymbol{u}$	Displacement vector
$\boldsymbol{v}$	Nodal displacement vector

Greek Symbols

Symbol	Definition
β_1, β_2, β_c, β_{aux}	Centering parameters for interior point method
$\boldsymbol{\varepsilon}$	Engineering strains in Voigt form
$\boldsymbol{\eta}$ (Ch. 8)	Coordinates (r, s) in element coordinate frame
κ (Ch. 10-5)	Isentropy constant
μ	Penalty parameter for wrinkling slack
$\boldsymbol{\xi}$	Coordinates (x, y) in reference configuration
$\boldsymbol{\xi}$ (Ch. 9)	Knot vector
$\boldsymbol{\xi}^*$ (Ch. 9)	Unrepeated knot vector
$\mathit{\Pi}$	Potential energy in the membrane
$\boldsymbol{\rho}_0$	Nodal position vector in reference configuration
$\boldsymbol{\sigma}$	Stresses in Voigt form
$\phi(\boldsymbol{E})$	Strain energy as function of $\boldsymbol{E}$
$\phi^*(\boldsymbol{S})$	Complementary strain energy as function of $\boldsymbol{S}$
$\phi^\sharp(\boldsymbol{E})$	Relaxed strain energy function
$\psi(\boldsymbol{F})$	Strain energy as function of $\boldsymbol{F}$

Chapter 1

Introduction

Membrane structures are widely present in nature and used in human applications. Many of the cells in the human body are protected from their surroundings by membranes and developing fetuses are protected in this way. On a larger scale, membrane structures have a rich history of use across many disciplines and are widely used in aerospace and structural engineering applications. A few examples can be found in solar sails, atmospheric balloons and parachutes. These membranes have many advantages, including their ability to take complex shapes and their low mass to surface ratio, which is especially important in aerospace engineering, however, although membranes can carry tensile loads very well, they tend to wrinkle under the slightest compressive load. These wrinkles may cause a failure of the membrane structure as they affect the load carrying capabilities of the membrane. In order to assess these load carrying capabilities it is important to predict the stress distribution in the membrane taking into account the possible presence of wrinkles.

In structural engineering applications wrinkles in a structure are often of a much smaller scale than the structure itself. In order to model these wrinkles the mesh size in e.g. a finite element model needs to be smaller than the wrinkle size, leading to high computational costs. For large but reasonable membrane structures too many computations are then required for existing computers to solve within an acceptable time and at an acceptable cost.

A solution to these high computational costs is to model the wrinkles as a continuous in-plane contraction of the membrane. The exact geometry of the wrinkles is lost by this procedure, however the stress field in the membrane is modeled accurately and the computational costs are reduced significantly. This solution, known as the tension field theory method is widely used and was first introduced by Wagner [38]. This method has been incorporated into the known theory of finite deformation by Pipkins [24, 25] using a relaxed strain energy function, which forms the basis of the method presented in this thesis. It is investigated whether a variational formulation of the relaxed strain energy function can be used to obtain a robust and efficient method to model the stress distribution in membranes in the presence of wrinkles.

The first objective was to obtain the variation formulation of the relaxed strain energy

function and its mathematical properties. Secondly this formulation was applied to the finite element method and tested for different membrane configurations. Simultaneously the method was verified and validated. The efficiency and robustness of the method was assessed using a combination of the mathematical properties of the governing equations and the numerical results of the analyzed examples.

The thesis is structured as follows. An overview of the available literature on the modeling of membrane wrinkling is presented in Chapter 2. The mathematical preliminaries required to obtain the variational formulation of the relaxed strain energy are considered in Chapter 3. The kinematics and equilibrium conditions are the topics of Chapters 4 and 5 respectively. The latter contains the variational formulation of the relaxed strain energy. In Chapter 6 the numerical implementation of this formulation is discussed after which Chapters 7 and 8 are dedicated to the application of the numerical implementation to triangular and quadrilateral finite elements respectively. The principles of isogeometric analysis are presented in Chapter 9. Then the method is tested in Chapter 10 where the numerical results are presented for different membrane loading cases. The verification and validation of the method is also done in this Chapter 10. Finally the conclusions and recommendations for future research are presented in Chapter 11.

Chapter 2

Literature Review

In this chapter an outline of the research performed on membrane wrinkling is presented by investigating several of the available methods used to model this phenomenon. These methods are divided into analytical and numerical methods. Many of the available numerical methods are applications of the most general analytical method based on the tension field theory first described by Wagner [38]. In this theory the bending stiffness of the membrane is fully neglected which means that any compression immediately results in out of plane deformation of the membrane. Both the analytical and numerical methods are categorized based on whether the tension field theory method is applied.

2-1 Analytical Methods

Without Tension Field Theory

The first analytical solution is for a thin sheet under stretching load as proposed by Puntel [26]. Even when the whole sheet is under tension it still wrinkles at the clamps, because at these clamps the Poisson's effect of the material is restricted. Puntel develops an analytical solution for the wrinkling geometry and the membrane stresses by minimizing the bending and membranal energy of the sheet. It is shown that wrinkling of the membrane occurs above a certain threshold stress. The aspect ratio of the sheet determines the number of wrinkles.

As these results have not been verified or validated further experiments are required to assess the performance of this model. A further limitation of this solution is that the membrane sheet is perfectly flat, which means that curvatures cannot be taken into account.

The second analytical model is presented in Vella et al. [37]. In this model a pressurized, spherical, elastic membrane under a point loading is analyzed. The pressure inside the shell is a variable in the model, which shows a clear transition from a polygonal balloon structure for low internal pressure to a wrinkled balloon structure at high internal pressure. A relation between this wrinkling transition and the internal pressure is established. Numerical simulations

are applied to verify this analytical model, which show a good agreement between the finite elements (FE) and the analytical solution. A limitation of the model is its restriction to spherical membranes only, which means that it can only be applied in very limited number of cases.

Apparently, the main disadvantage of the analytical models discussed is their restriction to specific membrane structures and loading conditions. This means that to understand the wrinkling of more complicated membrane structures a general set of equations is required. The tension field of Wagner [38] theory provides this governing set of equations.

With Tension Field Theory

The tension field theory, introduced by Wagner [38], presents the general differential equations governing the load carrying capabilities of a wrinkled sheet. It is assumed that the membrane does not have any bending stiffness. For this reason any compressive stress immediately cause wrinkling of the membrane. The wrinkling is then modeled as an in-plane contraction of the membrane and the shear load is modeled by a tension field in the direction of the principal stress. The differential equations are obtained by applying minimization of energy. It should be noted that the exact geometry of the wrinkles is lost in this theory, as this is modeled as in-plane contraction.

A solution to the governing equations of tension field theory for specific load cases is presented in Mansfield [14, 15]. He shows that for infinitesimal deformation the tension rays in a membrane are straight lines. Based on this the stresses and strains in the membrane are obtained by deriving a case dependent potential function which, when integrated over the membrane area, yields the strain energy. The membrane stresses and strains are then obtained by equating the derivative of this potential function with respect to change in tension ray orientation to a constant. Mansfield presents the potential function for several different load cases such as a rectangular membrane strip under shear/tension load and an annular ring under torsion. The results of this model are verified with experiments and show good qualitative agreements.

An important advantage of the Mansfield solution is that it serves very well as a verification for numerical methods, as it is able to model relatively complicated stress distributions, or tension fields, in the membrane. This includes the sheared membrane strip for which the tension field contains large gradients near the corners of the membrane. In fact the stresses are singular under pure shear loading. A disadvantage of this analytical solution is the relatively high costs of implementation as the governing equation is highly non-linear and the solution is given in the form of an indefinite surface integral.

Pipkin [24, 25] in his work incorporates the tension field theory method into the known theory of finite deformations as a special case of non-linear elasticity. A modified stored energy function is developed by relaxing the strain energy function of the material to obtain a non-decreasing and convex relaxed strain energy function. It is proven that this relaxation results in a compression-free stress field and is quasi-convex with respect to the deformation of the membrane. The latter means that minimization of the relaxed strain energy is stable and has a unique solution.

Based on this work Steigmann [34] presents the tension field theory in terms of two poten-

tial functions, a stretch and a force potential. The configuration of a membrane in terms of strains and stresses is described by these potential functions. Different membrane states are derived and it is demonstrated that application of the relaxed strain energy leads to stable solutions for the stress distribution in the membrane. Steigmann et al. [10] also present the first numerical results based on the tension field theory.

2-2 Numerical Methods

Without Tension Field Theory

The wrinkling behavior of membranes can be modeled using standard numerical methods including e.g. non-linear shell elements in which buckling is taken into account. This approach does not require any modifications, such as the tension field theory method, of the standard theory of non-linear mechanics. It does however, require the finite elements to be smaller than the wrinkles to capture them, which can quickly lead to very large models.

A geometrically exact numerical method specifically designed for membranes is proposed by Weinberg et al. [40]. In order to model the detailed geometry of the wrinkles, an artificial viscosity is introduced. This viscosity ensures the governing equations remain elliptic and it is related to the out of plane displacement and rotations, i.e. to the wrinkles. Using this method the exact geometry of the wrinkles and the membrane stresses are computed based on the principal of virtual work.

Another method for modeling membrane wrinkling without applying the tension field theory is proposed by Flores et al. [8]. This method includes the design of a thin three-noded rotation-free shell element. The difference between this finite element and other triangular elements is that the strain in neighboring elements is used in the calculations, which has as advantage that a coarser mesh can be applied for the modeling, however, the finite element mesh still has to be smaller than the wrinkle to detect it. The element can be applied to both isotropic and anisotropic materials.

An important characteristic of the non-linear method is it utilizes an explicit solver. This has as an advantage that e.g. contact problems can be dealt with easier, which is important in modeling the draping of membranes.

These two geometrically exact numerical methods are attractive when the exact geometry of the wrinkles is required or when the wrinkles are large, e.g. when simulating the draping behavior of a fabric. In other cases where the wrinkle geometry is of marginal importance, applying these methods is not cost efficient because the finite elements have to be smaller than the wrinkles, which become smaller when the membrane thickness decreases [21]. A possible solution is to model the wrinkles as a continuous in-plane contraction of the membrane. The exact geometry of the wrinkles is lost by this procedure, however, the stress field in the membrane is modeled accurately and the computational costs are reduced significantly. This solution, known as the earlier mentioned tension field theory, is widely used to model the load carrying capabilities of a membrane.

With Tension Field Theory

The tension field theory models the wrinkles as a continuous in-plane contraction field, which measures the 'intensity' of the wrinkles but is independent of individual wrinkles. Consequently the size of the finite elements is not governed by the wrinkles and thus can be larger, which will increase the cost efficiency of the numerical methods. The implementation of the tension field theory is not trivial, which is why several different methods have been proposed.

The first class of method implementing the tension field theory rely on a modification of the material law of the membrane. This includes the projection technique presented by Akita et al. [1], which is based on splitting the total deformation into two parts. The first part represents the elastic deformation which carries strain energy and the second part of the deformation is wrinkling deformation which is assumed to have zero-strain energy, i.e. no strain energy. This zero-strain part is projected out of the 'classical' elasticity matrix, resulting in the effective elasticity matrix.

This projection techniques is further investigated by Jarasjarungkiat et al. [11]. They modify the projection method to enable modeling of both isotropic and orthotropic materials by modifying the stress-strain relations within the element to handle the compressive stresses. The results obtained from this method are verified using some relatively simple analytical problems. The rate of convergence is improved with respect to the original projection technique whereas the number of equilibrium iterations can be reduced.

In the second class of numerical methods for modeling the tension field in membranes maintains the constitutive law is maintained, but the deformation gradient is modified. Roddeman et al. [29] develop the theory and analysis for this modification in isotropic materials. Two wrinkling parameters are introduced which represent the direction of the wrinkles an the in-plane contraction they induce. The working principle of this technique is based on dividing the total strain into an elastic part and a wrinkling part. These wrinkling strains are introduced to eliminate the compressive stresses. Based on this division the governing equations are developed. Relatively simple load cases are modeled to verify the the theory. Epstein [7] extends the method to enable the modeling of general anisotropic materials. A thorough finite element implementation of this work is performed by Schoop et al. [32]. Several numerical studies are performed including the pressurization of an airship.

Raible et al. [27] extend the method for orthotropic membrane materials. The reason for taking this into account is that many membrane structures are reinforced by fibres, which causes orthotropy of the material. The regions in the structure that are wrinkled or slack are given an extra strain contribution, whereas the taut region is computed using standard stress-strain relations. As a consequence each element contains an *if-else* statement to check whether the state of the material is either taut, wrinkled or slack.

None of the methods which have been treated so far is designed to model inelastic material behavior, which is where the method of Mosler et al. [19] comes in. In order to model inelastic membranes a formulation of the wrinkling problem is presented, again by means of dividing the strain into an elastic and a wrinkling part. This formulation is then coupled to standard formulations of plasticiity. The energy minimization is performed by developing a potential function of the stresses in the sheet. The advantage of the model is it allows modeling of both the elastic and plastic region of a material. The model is validated with experiments and other numerical models for the annular membrane ring under torsion. The results show

to agree well with the experimental data.

The theory presented by Roddeman et al. [29] is extended to a dynamics model by Kang [12]. An explicit scheme is applied to analyze the dynamics response of the stress state in a wrinkled membrane. The method makes it possible to model contact between the membrane and a rigid body and its performance is verified using modeling the inflation of an orthotropic airbag which is impacted onto a rigid plane. A similar dynamic model is proposed by Miyazaka [18]. In his work a virtual shear displacement is included in addition to the in-plane contraction due to wrinkling. This results only in an approximation of the wrinkle directions, but yields a more stable and cost efficient method.

A finite element specifically designed to model the stress distribution in a wrinkled membrane is proposed by Pagitz et al. [21]. This three-node membrane element has one extra rotational degree of freedom (DOF) which controls the tension direction and enforces continuity in the stress distribution. Energy minimization is applied to solve for displacements and stress directions. The element is verified with the analytical model of Mansfield [14] presented earlier in this chapter. The element is capable of modeling the tension directions accurately even in the nearly slacked regions, which are challenging due to their very low stress and high wrinkle density. A drawback of this method is in the fact that in taut or slacked regions the stress field does not have a single principal direction, but two and zero respectively. Therefore the DOF controlling the tension direction is not defined in these regions and the element is only applicable in wrinkled regions.

2-3 Proposed Method

The objective of the research reported in this thesis was to design a robust and efficient method to model the load carrying capabilities of wrinkled membranes. The tension field theory method was applied as this allows us to model complex membrane structures whilst still keeping the computational costs within acceptable limits. Effectively the objective was to fill the gaps left open in the numerical methods described in this chapter.

The relaxation of the strain energy function proposed by Pipkin [25] is of vital importance in this thesis. Applying this relaxed strain energy function consistently results in a set of convex equations describing the tension field in the membrane. These convexity properties are not exploited by the available methods, and it is this that will be dealt with in the research reported here. This will increase the efficiency of the method as efficient minimization algorithms exist for convex functions.

The numerical methods described in the literature all require an *if-else* statement to check whether the membrane is in a taut, wrinkled or slack stated and to act accordingly. Performing these checks costs time and in the case where a membrane changes its state during the simulation, completely new information has to be computed or old information is thrown away. The *if-else* statements also make the methods unattractive for implementation into FEM software. The method proposed in this thesis does not require *if-else* statements, this can be achieved whilst still preserving the convexity properties of the equations. As a result the computations are more efficient and the method could potentially be implemented into FEM software more easily.

With the exception of the method described by Mosler et al. [19], all the presented numerical methods have a specified material law. Consistent application of Pipkin's relaxed

strain energy function in this thesis allows us to implement any material law as long as its stress-strain relation is unique. As this requirement is satisfied by most material laws the restriction on materials is only very small, which leads to a robust method.

The final gap in the literature to be filled is to verify the method proposed using a relatively complicated analytical model. Many numerical models have been verified with a simple analytical model, with other numerical methods or by qualitative comparisons with experiments. A verification of the stress distribution in a membrane with the relatively complex Mansfield method has been performed by Pagitz et al. [21], however without a convergence analysis; for the research discussed in this thesis a convergence study using the Mansfield solution was performed for the standard finite elements with linear shape functions, and for higher order spline based shape functions.

Chapter 3

Mathematical Preliminaries

The main objective of the research discussed in this thesis was to design a method to model the stress distribution in membranes based on a robust and efficient application of the tension field theory method of Wagner [38]. This required several mathematical tools which are presented in this chapter. Some aspects of tensor analysis are presented in Section 3-1. Next the transformation of the stress and strain tensor into a different reference frame is considered in Section 3-2. The concept of a relaxed strain energy function is implemented in the development of the method. This concept relies heavily on the convexity properties of a function and its relaxation, which are treated in Sections 3-3 and 3-4 respectively.

3-1 Tensor Analysis

The concepts of vectors and tensors are important in continuum mechanics as they are used to represent physical quantities such as forces, stresses and strains. In order to represent e.g. a force vector one requires a coordinate frame and the components of the vector. In a different coordinate frame the vector components will be different, but the the physical force vector remains the same. Similarly, the physical quantity which is represented by a tensor is independent of the chosen coordinate frame. The distinction between a matrix and a tensor follows from this as a matrix contains the components of the tensor in a specific coordinate frame. Changing this frame will affect the components and thus the matrix but will leave the tensor unaffected.

In this section some basic concepts about tensor analysis are presented [13]. In this analysis vectors and tensors are discussed for general coordinate frames which allows a more direct and efficient representation of physical phenomena.

3-1-1 Vectors

Consider a coordinate frame in $\mathbb{R}^3$ with the basis vectors $\boldsymbol{e}_i$ $(i = 1, 2, 3)$. These basis vectors are linearly independent, but they can have any length and are not required to be orthogonal.

The vector $\boldsymbol{x}$ can be represented in this coordinate frame as:

$$\boldsymbol{x} = x^i \boldsymbol{e}_i = \sum_{i=1}^{3} x^i \boldsymbol{e}_i \tag{3-1}$$

The repeated index represents a summation when it appears as a sub- and superscript combination. The distinction between this sub- and superscript is important in non-Cartesian coordinate frames. From Equation (3-1) it is not possible to extract the components x^i directly for a given vector $\boldsymbol{x}$ and basis $\boldsymbol{e}_i$. For this purpose a set of dual basis vectors $\boldsymbol{e}^i$ is defined such that for $i = 1, 2, 3$:

$$x^i = \boldsymbol{x} \cdot \boldsymbol{e}^i \tag{3-2}$$

The basis vectors $\boldsymbol{e}^i$ are determined uniquely by Equation (3-2) and are usually referred to as the contravariant basis vectors, whereas $\boldsymbol{e}_i$ represent the covariant basis vectors. The vector $\boldsymbol{x}$ can be represented in the coordinate frame with basis vectors $\boldsymbol{e}^i$:

$$\boldsymbol{x} = x^i \boldsymbol{e}_i = x_i \boldsymbol{e}^i \tag{3-3}$$

The components x^i and x_i are not the same in general and they are referred to as the contravariant and covariant components respectively. The relation between $\boldsymbol{e}_i$ and $\boldsymbol{e}^j$ is obtained by rewriting Equation (3-2):

$$x^i = \boldsymbol{x} \cdot \boldsymbol{e}^i = \left(x^j \boldsymbol{e}_j\right) \cdot \boldsymbol{e}^i = x^j \left(\boldsymbol{e}_j \cdot \boldsymbol{e}^i\right) \tag{3-4}$$

which shows:

$$\boldsymbol{e}_j \cdot \boldsymbol{e}^i = \delta^i_j = \begin{cases} 1 & \text{if } i = j \\ 0 & \text{if } i \neq j \end{cases} \tag{3-5}$$

Using the two representations of $\boldsymbol{x}$ in Equation (3-3) one can write the inner product of two arbitrary vectors $\boldsymbol{a}$ and $\boldsymbol{b}$ in multiple different forms. Equation (3-6) presents this inner product using covariant basis vectors:

$$\boldsymbol{a} \cdot \boldsymbol{b} = a^i \boldsymbol{e}_i \cdot b^j \boldsymbol{e}_j = a^i b^j \boldsymbol{e}_i \cdot \boldsymbol{e}_j = a^i b^j g_{ij} \tag{3-6}$$

in which g_{ij} are the covariant components of the metric tensor:

$$g_{ij} = \boldsymbol{e}_i \cdot \boldsymbol{e}_j \tag{3-7}$$

Writing $\boldsymbol{a} \cdot \boldsymbol{b}$ using contravariant basis vectors gives:

$$\boldsymbol{a} \cdot \boldsymbol{b} = a_i \boldsymbol{e}^i \cdot b_j \boldsymbol{e}^j = a_i b_j \boldsymbol{e}^i \cdot \boldsymbol{e}^j = a_i b_j g^{ij} \tag{3-8}$$

with:

$$g^{ij} = \boldsymbol{e}^i \cdot \boldsymbol{e}^j \tag{3-9}$$

Finally the dot product can be represented using mixed basis vectors:

$$\boldsymbol{a} \cdot \boldsymbol{b} = a^i \boldsymbol{e}_i \cdot b_j \boldsymbol{e}^j = a^i b_j \delta^j_i = a^i b_i \tag{3-10}$$

Equations (3-6), (3-8) and (3-10) give three equivalent expressions for the dot product as:

$$\boldsymbol{a} \cdot \boldsymbol{b} = a^i b^j g_{ij} = a_i b_j g^{ij} = a^i b_i = a_i b^i \tag{3-11}$$

From these equalities the relation between covariant and contravariant components of a vector becomes:

$$\begin{aligned} x_j &= x^i g_{ij} \\ x^j &= x_i g^{ij} \end{aligned} \tag{3-12}$$

A special coordinate frame is the Cartesian frame in which the basis vectors are orthonormal. In this case the components of the metric tensor become $g_{ij} = \delta_{ij}$, which results in $x^i = x_i$ and $\boldsymbol{e}_i = \boldsymbol{e}^i$.

3-1-2 Tensors

Vectors can be considered to be first order tensors as they have only one index. Second order tensors follow naturally from these vectors by the introduction of the tensor product $\boldsymbol{a} \otimes \boldsymbol{b} \equiv \boldsymbol{ab}$. Using index notation this tensor product $\boldsymbol{ab}$ can be written as:

$$\boldsymbol{ab} = a^i \boldsymbol{e}_i b^j \boldsymbol{e}_j = a^i b^j \boldsymbol{e}_i \boldsymbol{e}_j \tag{3-13}$$

The result of this tensor product is the second order tensor $\boldsymbol{A}$ which, using the concepts of Section 3-1-1, can be written in different forms such as:

$$\boldsymbol{A} = A^{ij} \boldsymbol{e}_i \boldsymbol{e}_j = A^i{}_j \boldsymbol{e}_i \boldsymbol{e}^j = g_{ik} A^k{}_j \boldsymbol{e}^i \boldsymbol{e}^j \tag{3-14}$$

Higher order tensors can be obtained by applying the tensor product multiple times. A fourth order tensor C is shown in Equation (3-15).

$$\mathsf{C} = C^{ijkl} \boldsymbol{e}_i \boldsymbol{e}_j \boldsymbol{e}_k \boldsymbol{e}_l \tag{3-15}$$

In Table 3-1 several tensor operations are presented in tensor, index and matrix notation. The matrix notation, denoted by [..], contains the tensor components in a specified coordinate frame which are required to do the actual numerical computations. Note that the fourth order tensor product $\boldsymbol{AB}$ cannot be written in matrix notation.

Tensor Notation	**Index Notation**	**Matrix Notation**
$\boldsymbol{ab}$	$a^i b^j \boldsymbol{e}_i \boldsymbol{e}_j$	$[\boldsymbol{a}][\boldsymbol{b}]^T$
$\boldsymbol{a} \cdot \boldsymbol{b}$	$a^i b_i$	$[\boldsymbol{a}]^T[\boldsymbol{b}]$
$\boldsymbol{AB}$	$A^{ij} B^{kl} \boldsymbol{e}_i \boldsymbol{e}_j \boldsymbol{e}_k \boldsymbol{e}_l$	-
$\boldsymbol{A} \cdot \boldsymbol{B}$	$A^{ij} B_j{}^k \boldsymbol{e}_i \boldsymbol{e}_k$	$[\boldsymbol{A}][\boldsymbol{B}]$
$\boldsymbol{A}^T \cdot \boldsymbol{B}$	$A^{ji} B_j{}^k \boldsymbol{e}_i \boldsymbol{e}_k$	$[\boldsymbol{A}]^T[\boldsymbol{B}]$
$\boldsymbol{A} : \boldsymbol{B}$	$A^{ij} B_{ij}$	$\mathrm{tr}[\boldsymbol{A}]^T[\boldsymbol{B}]$

Table 3-1: Comparison of notations

3-2 Stress and Strain Transformation

As mentioned in the previous section many physical quantities are represented by tensors. Two of these tensors required in this thesis are the Green-Lagrange strain tensor $\boldsymbol{E}$ and the second Piola-Kirchhoff stress tensor $\boldsymbol{S}$. These tensors needed to be represented in different coordinate frames in Chapter 8. The transformation of the strains and stresses between two coordinate frames is considered in this section.

The second Piola-Kirchhoff stress tensor $\boldsymbol{S}$ is given as:

$$\boldsymbol{S} = S^{ij}\boldsymbol{e}_i\boldsymbol{e}_j \qquad i,j = 1,2 \tag{3-16}$$

in which $\boldsymbol{e}_i$ form the covariant basis vectors of the coordinate frame. Note that $\boldsymbol{S}$ is generally presented with contravariant components as is derived in Appendix A. It is also shown in Appendix A that $\boldsymbol{S}$ is symmetric, meaning $S^{ij} = S^{ji}$.

The stress transformation to be considered is from a Cartesian frame with coordinates x, y to an arbitrary reference frame with coordinates r, s. The relation between these components is given as:

$$\begin{pmatrix} dx \\ dy \end{pmatrix} = \begin{bmatrix} \frac{\partial x}{\partial r} & \frac{\partial x}{\partial s} \\ \frac{\partial y}{\partial r} & \frac{\partial y}{\partial s} \end{bmatrix} \begin{pmatrix} dr \\ ds \end{pmatrix} = \boldsymbol{J} \begin{pmatrix} dr \\ ds \end{pmatrix} \tag{3-17}$$

For the Cartesian reference frame the components of the basis vectors $\boldsymbol{e}_i$ are as shown in Equation (3-18):

$$\boldsymbol{e}_x = \begin{bmatrix} 1 \\ 0 \end{bmatrix} \qquad \boldsymbol{e}_y = \begin{bmatrix} 0 \\ 1 \end{bmatrix} \tag{3-18}$$

In the arbitrary coordinate system the basis vectors are:

$$\boldsymbol{e}_r = \frac{\partial x}{\partial r}\boldsymbol{e}_x + \frac{\partial y}{\partial r}\boldsymbol{e}_y = \begin{bmatrix} \frac{\partial x}{\partial r} \\ \frac{\partial y}{\partial r} \end{bmatrix} = \begin{bmatrix} J_{11} \\ J_{21} \end{bmatrix}; \qquad \boldsymbol{e}_s = \begin{bmatrix} J_{12} \\ J_{22} \end{bmatrix} \tag{3-19}$$

Using these basis vectors the stress tensor can be written in Cartesian x, y and arbitrary r, s coordinates by applying Equation (3-16). With the notation $S^{xx} = \sigma_x$, $S^{yy} = \sigma_y$ and $S^{xy} = S^{yx} = \tau_{xy}$, this gives:

$$\begin{aligned} \boldsymbol{S} &= \sigma_x\boldsymbol{e}_x\boldsymbol{e}_x + \sigma_y\boldsymbol{e}_y\boldsymbol{e}_y + \tau_{xy}\left(\boldsymbol{e}_x\boldsymbol{e}_y + \boldsymbol{e}_y\boldsymbol{e}_x\right) \\ &= \sigma_r\boldsymbol{e}_r\boldsymbol{e}_r + \sigma_s\boldsymbol{e}_s\boldsymbol{e}_s + \tau_{rs}\left(\boldsymbol{e}_r\boldsymbol{e}_s + \boldsymbol{e}_s\boldsymbol{e}_r\right) \end{aligned} \tag{3-20}$$

Equating the components of these two formulations of the stress tensor gives the transformation matrix $\boldsymbol{T}_\sigma$ for the stresses as given in Equation (3-21):

$$\begin{pmatrix} \sigma_x \\ \sigma_y \\ \tau_{xy} \end{pmatrix} = \underbrace{\begin{bmatrix} J_{11}^2 & J_{12}^2 & 2J_{11}J_{12} \\ J_{21}^2 & J_{22}^2 & 2J_{21}J_{22} \\ J_{11}J_{21} & J_{12}J_{22} & J_{11}J_{22} + J_{12}J_{21} \end{bmatrix}}_{\boldsymbol{T}_\sigma} \begin{pmatrix} \sigma_r \\ \sigma_s \\ \tau_{rs} \end{pmatrix} \tag{3-21}$$

Note that in this notation the stress components are listed in vector form, which is known as the Voigt notation. The transformation of the stress components can now be written as:

$$\boldsymbol{\sigma}_{xy} = \boldsymbol{T}_\sigma\boldsymbol{\sigma}_{rs} \tag{3-22}$$

In contrast to the stress tensor $\boldsymbol{S}$, the Green-Lagrange strain tensor $\boldsymbol{E}$ is denoted by its covariant components E_{ij}. Its components therefore transform differently from the stress tensor as follows:

$$\boldsymbol{\varepsilon}_{xy} = \boldsymbol{T}\boldsymbol{\varepsilon}_{rs} \tag{3-23}$$

With $\boldsymbol{\varepsilon}_{xy} = [\varepsilon_x, \varepsilon_y, \gamma_{xy}]^T$ being the Voigt form of the engineering strains. To find the expression for $\boldsymbol{T}$ it should be realized that the internal strain energy ϕ resulting from $\boldsymbol{S}$ and $\boldsymbol{E}$ is independent of the coordinate frame. This strain energy is given as:

$$\phi = \boldsymbol{S} : \boldsymbol{E} = S^{ij}E_{ij} \tag{3-24}$$

This expression can be written using both the Cartesian x, y and arbitrary r, s components. Using the Voigt form and transformation matrices this yields:

$$\begin{aligned} \boldsymbol{\varepsilon}_{xy}^T\boldsymbol{\sigma}_{xy} &= \boldsymbol{\varepsilon}_{rs}^T\boldsymbol{\sigma}_{rs} \\ \boldsymbol{\varepsilon}_{rs}^T\boldsymbol{T}^T\boldsymbol{T}_\sigma\boldsymbol{\sigma}_{rs} &= \boldsymbol{\varepsilon}_{rs}^T\boldsymbol{\sigma}_{rs} \end{aligned} \tag{3-25}$$

which states that $\boldsymbol{T}^T\boldsymbol{T}_\sigma = \boldsymbol{I}$. Solving this equality for $\boldsymbol{T}$ gives the transformation of the strain components:

$$\boldsymbol{T} = \boldsymbol{T}_\sigma^{-T} = \frac{1}{(\det\boldsymbol{J})^2}\begin{bmatrix} J_{22}^2 & J_{21}^2 & -J_{21}J_{22} \\ J_{12}^2 & J_{11}^2 & -J_{11}J_{12} \\ -2J_{12}J_{22} & -2J_{11}J_{21} & J_{11}J_{22} + J_{12}J_{21} \end{bmatrix} \tag{3-26}$$

3-3 Convexity Analysis

The principle of minimizing the total potential energy function is often applied to find the deformed configuration of a general structure under specific loading conditions. When minimizing a function it is important to know its convexity properties as these may guarantee e.g. existence and uniqueness of the solution. An analysis of convexity characteristics and the conditions for a convex strain energy function is performed in this section. The latter was used to define the relaxed strain energy function in Chapter 5.

3-3-1 Convexity

A scalar valued function $f(\boldsymbol{X})$ is called convex if and only if for all $\boldsymbol{X}_1$ and $\boldsymbol{X}_2$:

$$f((1-\alpha)\boldsymbol{X}_1 + \alpha\boldsymbol{X}_2) \leq (1-\alpha)f(\boldsymbol{X}_1) + \alpha f(\boldsymbol{X}_2) \qquad 0 \leq \alpha \leq 1 \tag{3-27}$$

Convex functions have many advantages in optimization problems where the minimum of the function needs to be obtained. As this minimum can simply be found by searching in the direction of descend of the function, many efficient numerical algorithms exist to find the minimum of a convex function. Note that the convexity property guarantees that when a local minimum of the function is found, this is the global minimum of the function. A graphical interpretation of this definition for the case where the argument of the function is a scalar is shown in Figure 3-1.

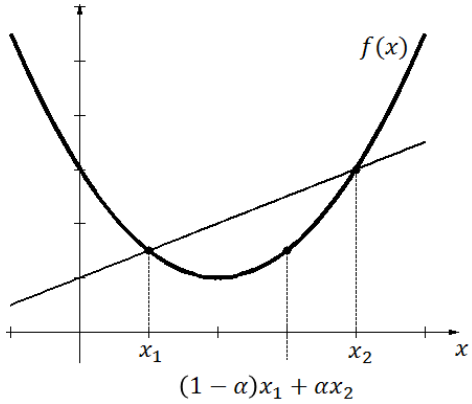

Figure 3-1: Sketch of a convex function.

3-3-2 Rank-One Convexity

A weaker form of convexity is rank-one convexity, which means that all convex functions are rank-one convex. Rank-one convexity occurs in case Equation (3-27) holds for all $\boldsymbol{X}_1$ and $\boldsymbol{X}_2$ such that $\text{rank}(\boldsymbol{X}_2 - \boldsymbol{X}_1) \leq 1$, this means $\boldsymbol{X}_2$ can be chosen to be:

$$\boldsymbol{X}_2 = \boldsymbol{X}_1 + \boldsymbol{a}\boldsymbol{b}^T$$

where $\boldsymbol{a}$ and $\boldsymbol{b}$ are arbitrary vectors. Substitution of $\boldsymbol{X}_2$ gives:

$$f((1-\alpha)\boldsymbol{X}_1 + \alpha\boldsymbol{X}_2) = f(\boldsymbol{X}_1 + \alpha\boldsymbol{a}\boldsymbol{b}^T) \tag{3-28}$$

which can be substituted into Equation (3-27) to yield the condition for rank-one convexity:

$$f(\boldsymbol{X}_1 + \alpha\boldsymbol{a}\boldsymbol{b}^T) \leq (1-\alpha)f(\boldsymbol{X}_1) + \alpha f(\boldsymbol{X}_1 + \boldsymbol{a}\boldsymbol{b}^T) \qquad 0 \leq \alpha \leq 1 \tag{3-29}$$

Note that in the case of a scalar-valued argument, rank-one convexity is equivalent to convexity.

3-3-3 Quasi-Convexity

Quasi-convexity is a type of convexity which is weaker than convexity but at least as strong as rank-one convexity [33]. This type of convexity is important as a quasi-convex function has a unique minimum which is the global minimum [4]. Consequently, a local minimum is guaranteed to be the global minimum if the function is at least quasi-convex. Quasi-convexity is equivalent to convexity and rank-one convexity for functions with a scalar-valued argument.

3-3-4 Conditions for Convexity of Strain Energy

The total potential energy function in a membrane was minimized to find the deformed configuration of the membrane as described in Chapter 5. One of the contributions to this potential energy is the internal strain energy of the membrane which depends on the deformation gradient $\boldsymbol{F}$ and is denoted by $\psi(\boldsymbol{F})$. The total potential energy function has a unique minimum

if $\psi(\boldsymbol{F})$ is at least quasi-convex. Using several propositions the conditions for this property are shown in the following.

The Green-Lagrange strain tensor is a function of the deformation gradient as shown in Equation (3-30).

$$\boldsymbol{E} = \frac{1}{2}\left(\boldsymbol{F}^T\boldsymbol{F} - \boldsymbol{I}\right) \tag{3-30}$$

This definition can be applied to express the strain energy as function of $\boldsymbol{E}$ to give $\phi(\boldsymbol{E}) = \psi(\boldsymbol{F})$. For the following, define a function $f(\boldsymbol{X})$ to be non-decreasing if and only if:

$$f(\boldsymbol{X} + \boldsymbol{Z}) \geq f(\boldsymbol{X}) \qquad \forall \boldsymbol{Z} \geq \boldsymbol{0}$$

Proposition 3.1. *If $\phi(\boldsymbol{E})$ is convex and non-decreasing, then $\psi(\boldsymbol{F})$ is convex.*

Proof.
The following equality is applied to prove this proposition:

$$\begin{aligned}&\left((1-\alpha)\,\boldsymbol{F}_1 + \alpha\boldsymbol{F}_2\right)^T\left((1-\alpha)\,\boldsymbol{F}_1 + \alpha\boldsymbol{F}_2\right)\\ &\qquad = (1-\alpha)\,\boldsymbol{F}_1^T\boldsymbol{F}_1 + \alpha\boldsymbol{F}_2^T\boldsymbol{F}_2 - \alpha\,(1-\alpha)\,\Delta\boldsymbol{F}^T\Delta\boldsymbol{F}\end{aligned} \tag{3-31}$$

with $\Delta\boldsymbol{F} = \boldsymbol{F}_1 - \boldsymbol{F}_2$. From the definition of the Green-Lagrange strain in (3-30), and (3-31) one gets:

$$\begin{aligned}&\psi\left((1-\alpha)\,\boldsymbol{F}_1 + \alpha\boldsymbol{F}_2\right)\\ &= \phi\left(\frac{1}{2}\left[\left((1-\alpha)\,\boldsymbol{F}_1 + \alpha\boldsymbol{F}_2\right)^T\left((1-\alpha)\,\boldsymbol{F}_1 + \alpha\boldsymbol{F}_2\right) - \boldsymbol{I}\right]\right)\\ &= \phi\left(\frac{1}{2}\left[(1-\alpha)\left(\boldsymbol{F}_1^T\boldsymbol{F}_1 - \boldsymbol{I}\right) + \alpha\left(\boldsymbol{F}_2^T\boldsymbol{F}_2 - \boldsymbol{I}\right) - \alpha\,(1-\alpha)\,\Delta\boldsymbol{F}^T\Delta\boldsymbol{F}\right]\right)\\ &= \phi\left((1-\alpha)\,\boldsymbol{E}_1 + \alpha\boldsymbol{E}_2 - \frac{1}{2}\alpha\,(1-\alpha)\,\Delta\boldsymbol{F}^T\Delta\boldsymbol{F}\right)\end{aligned} \tag{3-32}$$

for $0 \leq \alpha \leq 1$. The last term in this argument is positive and given that $\phi(\boldsymbol{E})$ is non-decreasing and convex, this expression can be written as:

$$\begin{aligned}\psi\left((1-\alpha)\,\boldsymbol{F}_1 + \alpha\boldsymbol{F}_2\right) &\leq \phi\left((1-\alpha)\,\boldsymbol{E}_1 + \alpha\boldsymbol{E}_2\right)\\ &\leq (1-\alpha)\,\phi\left(\boldsymbol{E}_1\right) + \alpha\phi\left(\boldsymbol{E}_2\right)\\ &= (1-\alpha)\,\psi\left(\boldsymbol{F}_1\right) + \alpha\psi\left(\boldsymbol{F}_2\right)\end{aligned} \tag{3-33}$$

which proves convexity of $\psi(\boldsymbol{F})$ by the definition in Equation (3-27). Note that in this expression the first inequality holds as $\phi(\boldsymbol{E})$ is non-decreasing and the second inequality exploits the convexity of $\phi(\boldsymbol{E})$. □

Proposition 3.2. *If $\psi(\boldsymbol{F})$ is rank-one convex, then $\phi(\boldsymbol{E})$ is non-decreasing.*

Proof.
Rank-one convexity of $\psi(\boldsymbol{F})$ means that for $\boldsymbol{F}_1 = \boldsymbol{F}$ and $\boldsymbol{F}_2 = \boldsymbol{F} + \boldsymbol{u}\boldsymbol{e}^T$ convexity conditions are satisfied, with $\boldsymbol{u}$ and $\boldsymbol{e}$ being any arbitrary vectors:

$$\psi\left(\boldsymbol{F} + \alpha\boldsymbol{u}\boldsymbol{e}^T\right) \leq (1-\alpha)\,\psi(\boldsymbol{F}) + \alpha\psi\left(\boldsymbol{F} + \boldsymbol{u}\boldsymbol{e}^T\right) \tag{3-34}$$

with $0 \leq \alpha \leq 1$. Using the definition of the Green-Lagrange strain in Equation (3-30) the left hand side of this expression can be rewritten as:

$$\begin{aligned}\psi\left(\boldsymbol{F}+\alpha\boldsymbol{u}\boldsymbol{e}^T\right) &= \phi\left(\frac{1}{2}\left[\left(\boldsymbol{F}+\alpha\boldsymbol{u}\boldsymbol{e}^T\right)^T\left(\boldsymbol{F}+\alpha\boldsymbol{u}\boldsymbol{e}^T\right)-\boldsymbol{I}\right]\right)\\ &= \phi\left(\frac{1}{2}\left[\boldsymbol{F}^T\boldsymbol{F}-\boldsymbol{I}+\alpha^2\boldsymbol{u}^T\boldsymbol{u}\boldsymbol{e}\boldsymbol{e}^T+\alpha\left(\boldsymbol{F}^T\boldsymbol{u}\boldsymbol{e}^T+\left(\boldsymbol{F}^T\boldsymbol{u}\boldsymbol{e}^T\right)^T\right)\right]\right)\end{aligned} \tag{3-35}$$

In order to further simplify this expression the kinematics of a membrane need to be considered, which will be done in detail in Chapter 4. For now it suffices to note that the membrane is a two-dimensional object which exists in three-dimensional space $\mathbb{R}^3$, this means that the initial configuration can be described by only two coordinates. In the deformed configuration the membrane can have deformed normal to its initial configuration, therefore three coordinates are required to describe this configuration when using the same coordinate frame as for the initial configuration. Consequently, the deformation gradient $\boldsymbol{F}$ of the membrane is represented by a 3×2 matrix, which means that the vector $\boldsymbol{u}$ in Equation (3-35) can be chosen such that $\boldsymbol{F}^T\boldsymbol{u} = \boldsymbol{0}$. In fact this holds when $\boldsymbol{u}$ is normal to the initial configuration as $\boldsymbol{F}^T\boldsymbol{u}$ represents the pull-back of $\boldsymbol{u}$.

Without loss of generality choose $\boldsymbol{u}^T\boldsymbol{u} = 2$ in Equation (3-35) and substitute to get:

$$\psi\left(\boldsymbol{F}+\alpha\boldsymbol{u}\boldsymbol{e}^T\right) = \phi\left(\boldsymbol{E}+\alpha^2\boldsymbol{e}\boldsymbol{e}^T\right) \tag{3-36}$$

This equality is substituted into Equation (3-34) which after rewriting results in:

$$\alpha\frac{\phi\left(\boldsymbol{E}+\alpha^2\boldsymbol{e}\boldsymbol{e}^T\right)-\phi\left(\boldsymbol{E}\right)}{\alpha^2} \leq \phi\left(\boldsymbol{E}+\boldsymbol{e}\boldsymbol{e}^T\right)-\phi\left(\boldsymbol{E}\right) \tag{3-37}$$

Taking the limit $\alpha \to 0_+$ on both sides causes the left hand side of this expression to approach zero, which follows as:

$$\lim_{\alpha\to 0_+}\frac{\phi\left(\boldsymbol{E}+\alpha^2\boldsymbol{e}\boldsymbol{e}^T\right)-\phi\left(\boldsymbol{E}\right)}{\alpha^2}$$

represents the directional derivative of $\phi(\boldsymbol{E})$ in the direction $\boldsymbol{e}$, which is bounded provided $\phi(\boldsymbol{E})$ is Lipschitz continuous. In the limit Equation (3-37) then becomes:

$$\phi\left(\boldsymbol{E}+\boldsymbol{e}\boldsymbol{e}^T\right) \geq \phi\left(\boldsymbol{E}\right)$$

Any semi-positive definite (spd) tensor $\Delta\boldsymbol{E} \geq \boldsymbol{0}$ can be written as $\Delta\boldsymbol{E} = \boldsymbol{a}\boldsymbol{a}^T + \boldsymbol{b}\boldsymbol{b}^T$, meaning:

$$\phi\left(\boldsymbol{E}+\Delta\boldsymbol{E}\right) = \phi\left(\boldsymbol{E}+\boldsymbol{a}\boldsymbol{a}^T+\boldsymbol{b}\boldsymbol{b}^T\right) \geq \phi\left(\boldsymbol{E}\right)$$

This expression proves that $\phi(\boldsymbol{E})$ is non-decreasing when $\psi(\boldsymbol{F})$ is rank-one convex. □

For the next proposition the notion of quasi-convexification is introduced. The quasi-convexification of $\psi(\boldsymbol{F})$ is the largest quasi-convex function which does not exceed $\psi(\boldsymbol{F})$.

The lower, non-decreasing envelope of $\phi(\boldsymbol{E})$ is the largest non-decreasing function which does not exceed $\phi(\boldsymbol{E})$ and is denoted by $\phi^\sharp(\boldsymbol{E}) = \psi^\sharp(\boldsymbol{F})$.

Proposition 3.3. *If $\phi(\boldsymbol{E})$ is convex, then its lower, non-decreasing envelope $\phi^\sharp(\boldsymbol{E})$ is the quasi-convexification of $\psi(\boldsymbol{F})$.*

Proof.
Using the convexity properties presented in this section as well as propositions 3.1 and 3.2, the following line of implications is obtained:

$$\begin{aligned}
&\text{convex + non-decreasing } \phi(\boldsymbol{E}) \\
&\quad \Rightarrow \text{convex } \psi(\boldsymbol{F}) \\
&\quad\quad \Rightarrow \text{quasi-convex } \psi(\boldsymbol{F}) \\
&\quad\quad\quad \Rightarrow \text{rank-one convex } \psi(\boldsymbol{F}) \\
&\quad\quad\quad\quad \Rightarrow \text{non-decreasing } \phi(\boldsymbol{E})
\end{aligned}$$

When $\psi(\boldsymbol{F})$ is quasi-convex, this guarantees the existence and uniqueness of a displacement field in the membrane which carries the minimum total potential energy. The sufficient condition for this quasi-convexity is a convex and non-decreasing $\phi(\boldsymbol{E})$ and the necessary condition that $\phi(\boldsymbol{E})$ is non-decreasing.

A special case occurs when $\phi(\boldsymbol{E})$ is convex, as in this case the lower non-decreasing envelope is both sufficient and necessary for quasi-convexity. This envelope, denoted by $\phi^\sharp(\boldsymbol{E})$, is thus the quasi-convexification of $\psi(\boldsymbol{F})$ exactly, which proves the proposition. □

3-4 Relaxation Formulation

It was shown that quasi-convexification of the strain energy function is given by its lower, convex and non-decreasing envelope $\phi^\sharp(\boldsymbol{E})$ in Section 3-3. In the remainder of this thesis the quasi-convexification will be referred to as the relaxation. How to obtain the relaxation of an arbitrary function $f(\boldsymbol{X})$, which was applied to obtain the relaxed strain energy function presented in Chapter 5, is shown in this section.

Proposition 3.4. *Let $f(\boldsymbol{X})$ be any scalar-valued function of a symmetric tensor $\boldsymbol{X}$ and let $f^\sharp(\boldsymbol{X})$ be the its relaxation, then:*

$$f^\sharp(\boldsymbol{X}) = \sup_{\boldsymbol{Y} \geq \boldsymbol{0}} [\boldsymbol{X} : \boldsymbol{Y} - f^*(\boldsymbol{Y})] \tag{3-38}$$

with $f^*(\boldsymbol{Y})$ being the complementary function of $f(\boldsymbol{X})$ defined by the Legendre-Fenchel transform:

$$f^*(\boldsymbol{Y}) = \sup_{\boldsymbol{X}} [\boldsymbol{X} : \boldsymbol{Y} - f(\boldsymbol{X})]$$

Proof.
An important property of the Legendre-Fenchel transform is that it always returns a convex function $f^*(\boldsymbol{Y})$ [28], which is shown by applying the definition from Equation (3-27):

$$\begin{aligned}
\alpha f^*(\boldsymbol{Y}_1) + (1-\alpha) f^*(\boldsymbol{Y}_2) &= \alpha \sup_{\boldsymbol{X}} [\boldsymbol{X} : \boldsymbol{Y}_1 - f(\boldsymbol{X})] + (1-\alpha) \sup_{\boldsymbol{X}} [\boldsymbol{X} : \boldsymbol{Y}_2 - f(\boldsymbol{X})] \\
&\geq \sup_{\boldsymbol{X}} [\boldsymbol{X} : (\alpha \boldsymbol{Y}_1 + (1-\alpha)\boldsymbol{Y}_2) - f(\boldsymbol{X})] \\
&= f^*(\alpha \boldsymbol{Y}_1 + (1-\alpha)\boldsymbol{Y}_2)
\end{aligned} \tag{3-39}$$

To prove the proposed definition of $f^\sharp(\boldsymbol{X})$ in Equation (3-38) is indeed the relaxation of $f(\boldsymbol{X})$, all four properties of the relaxation need to be demonstrated. First of all the convexity of

$f^\sharp(\boldsymbol{X})$ is proven by repeating the steps in Equation (3-39) for the proposed definition.

The second property of the relaxation is that $f^\sharp(\boldsymbol{X})$ needs to be non-decreasing. To prove this, let $\boldsymbol{Z} \geq \boldsymbol{0}$:

$$\begin{aligned} f^\sharp(\boldsymbol{X}) &= \sup_{\boldsymbol{Y}\geq\boldsymbol{0}} [\boldsymbol{Y} : \boldsymbol{X} - f^*(\boldsymbol{Y})] \\ &= \sup_{\boldsymbol{Y}\geq\boldsymbol{0}} [\boldsymbol{Y} : (\boldsymbol{X}+\boldsymbol{Z}) - f^*(\boldsymbol{Y}) - \boldsymbol{Y} : \boldsymbol{Z}] \\ &\leq \sup_{\boldsymbol{Y}\geq\boldsymbol{0}} [\boldsymbol{Y} : (\boldsymbol{X}+\boldsymbol{Z}) - f^*(\boldsymbol{Y})] + \sup_{\boldsymbol{Y}\geq\boldsymbol{0}} [-\boldsymbol{Y} : \boldsymbol{Z}] \\ &= f^\sharp(\boldsymbol{X}+\boldsymbol{Z}) \end{aligned} \tag{3-40}$$

which shows that $f^\sharp(\boldsymbol{X}+\boldsymbol{Z}) \geq f^\sharp(\boldsymbol{X})$ for $\forall \boldsymbol{Z} \geq \boldsymbol{0}$. Next it needs to be proven that $f^\sharp(\boldsymbol{X})$ does not exceed $f(\boldsymbol{X})$. For this purpose first the double complementary function $f^{**}(\boldsymbol{X})$ is defined in Equation (3-41):

$$\begin{aligned} f^{**}(\boldsymbol{X}) &= \sup_{\boldsymbol{Y}} \left[\boldsymbol{Y} : \boldsymbol{X} - \sup_{\boldsymbol{Z}} [\boldsymbol{Y} : \boldsymbol{Z} - f(\boldsymbol{Z})]\right] \\ &= \sup_{\boldsymbol{Y}} \left[\boldsymbol{Y} : \boldsymbol{X} + \inf_{\boldsymbol{Z}} [f(\boldsymbol{Z}) - \boldsymbol{Y} : \boldsymbol{Z}]\right] \\ &= \sup_{\boldsymbol{Y}} \inf_{\boldsymbol{Z}} [f(\boldsymbol{Z}) - \boldsymbol{Y} : (\boldsymbol{Z}-\boldsymbol{X})] \\ &\leq \inf_{\boldsymbol{Z}} \sup_{\boldsymbol{Y}} [f(\boldsymbol{X}+\boldsymbol{Z}) - \boldsymbol{Y} : \boldsymbol{Z}] \\ &= f(\boldsymbol{X}) \end{aligned} \tag{3-41}$$

The inequality in this expression follows from the weak duality principle:

$$\sup_{\boldsymbol{Y}} \inf_{\boldsymbol{X}} h(\boldsymbol{X},\boldsymbol{Y}) \leq \inf_{\boldsymbol{X}} \sup_{\boldsymbol{Y}} h(\boldsymbol{X},\boldsymbol{Y}) \qquad \forall h(\boldsymbol{X},\boldsymbol{Y})$$

Note that when $h(\boldsymbol{X},\boldsymbol{Y})$ is convex the inequality becomes an equality sign. Equation (3-41) shows $f^{**}(\boldsymbol{X}) \leq f(\boldsymbol{X})$ which results in $f^\sharp(\boldsymbol{X}) \leq f(\boldsymbol{X})$ as follows:

$$\begin{aligned} f^\sharp(\boldsymbol{X}) &= \sup_{\boldsymbol{Y}\geq\boldsymbol{0}} [\boldsymbol{Y} : \boldsymbol{X} - f^*(\boldsymbol{Y})] \\ &\leq \sup_{\boldsymbol{Y}} [\boldsymbol{Y} : \boldsymbol{X} - f^*(\boldsymbol{Y})] \\ &= f^{**}(\boldsymbol{X}) \leq f(\boldsymbol{X}) \end{aligned} \tag{3-42}$$

Finally the relaxation requires that the proposed definition in Equation (3-38) is the largest function with the three proven properties. For this, let $g(\boldsymbol{X})$ be any convex, non-decreasing function with $g(\boldsymbol{X}) \leq f(\boldsymbol{X})\ \forall \boldsymbol{X}$, meaning $g(\boldsymbol{X})$ satisfies all proven properties and can be shown to have $g^\sharp(\boldsymbol{X}) = g(\boldsymbol{X})$. Using the definition of the Legendre-Fenchel transformation one gets:

$$\begin{aligned} f^*(\boldsymbol{Y}) &= \sup_{\boldsymbol{X}} [\boldsymbol{X} : \boldsymbol{Y} - f(\boldsymbol{X})] \\ &\leq \sup_{\boldsymbol{X}} [\boldsymbol{X} : \boldsymbol{Y} - g(\boldsymbol{X})] + \sup_{\boldsymbol{X}} [g(\boldsymbol{X}) - f(\boldsymbol{X})] \\ &\leq g^*(\boldsymbol{Y}) \end{aligned} \tag{3-43}$$

Similarly it can be shown that $g^\sharp(\boldsymbol{X}) \leq f^\sharp(\boldsymbol{X})$, and therefore $g^\sharp(\boldsymbol{X}) = g(\boldsymbol{X}) \leq f^\sharp(\boldsymbol{X}) \leq f(\boldsymbol{X})$. This relation holds for all functions $g(\boldsymbol{X})$ with the mentioned properties, which means that $f^\sharp(\boldsymbol{X})$ needs to be the largest function with these properties. □

A special case occurs when $f(\boldsymbol{X})$ is convex, which is considered in Proposition 3.5.

Proposition 3.5. *Let $f(\boldsymbol{X})$ be a* convex*, scalar-valued function of a symmetric tensor $\boldsymbol{X}$ and let $f^\sharp(\boldsymbol{X})$ be its relaxation, then:*

$$f^\sharp(\boldsymbol{X}) = \inf_{\boldsymbol{Z}} \sup_{\boldsymbol{Y} \geq \boldsymbol{0}} [f(\boldsymbol{X} + \boldsymbol{Z}) - \boldsymbol{Y} : \boldsymbol{Z}] \tag{3-44}$$

Proof.
For any convex function $h(x)$ it holds $\sup \inf h(x) = \inf \sup h(x)$. Applying the definition of the relaxation in Equation (3-38) then yields for a convex $f(\boldsymbol{X})$:

$$\begin{aligned} f^\sharp(\boldsymbol{X}) &= \sup_{\boldsymbol{Y} \geq \boldsymbol{0}} \left[\boldsymbol{Y} : \boldsymbol{X} - \sup_{\boldsymbol{Z}} [\boldsymbol{Y} : \boldsymbol{Z} - f(\boldsymbol{Z})] \right] \\ &= \sup_{\boldsymbol{Y} \geq \boldsymbol{0}} \left[\boldsymbol{Y} : \boldsymbol{X} + \inf_{\boldsymbol{Z}} [f(\boldsymbol{Z}) - \boldsymbol{Y} : \boldsymbol{Z}] \right] \\ &= \sup_{\boldsymbol{Y} \geq \boldsymbol{0}} \inf_{\boldsymbol{Z}} [f(\boldsymbol{Z}) - \boldsymbol{Y} : (\boldsymbol{Z} - \boldsymbol{X})] \\ &= \inf_{\boldsymbol{Z}} \sup_{\boldsymbol{Y} \geq \boldsymbol{0}} [f(\boldsymbol{X} + \boldsymbol{Z}) - \boldsymbol{Y} : \boldsymbol{Z}] \end{aligned} \tag{3-45}$$

□

An example of two lower envelopes of an arbitrary non-convex function $f(x)$ is shown in Figure 3-2. The lower and convex envelope in Figure 3-2a is obtained from the double Legender-Fenchel transform and the quasi-convexification in Figure 3-2b from its definition in Equation (3-38).

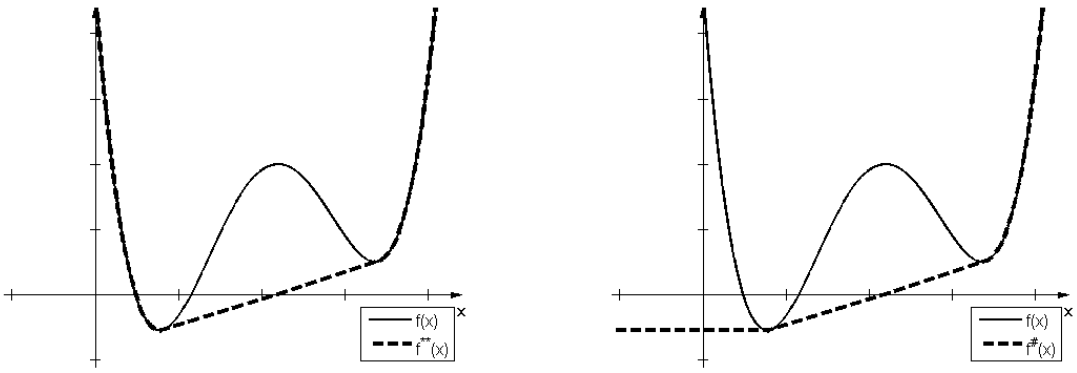

(a) Lower and convex envelope $f^{**}(x)$

(b) Lower, convex and non-decreasing envelope $f^\sharp(x)$

Figure 3-2: Sketch of two lower envelopes of $f(x)$

Chapter 4

Membrane Kinematics

Membranes are very thin shells and thus have a small bending stiffness, which is neglected in the analysis of the tension field in membranes. This causes the membrane to wrinkle under the slightest compressive deformation. In tension field theory these wrinkles are modeled as in-plane contraction, meaning that all strains are membranal. As a result only in-plane strains need to be considered for membranes. In this chapter the kinematics of the membrane is presented by the strain-displacement relation in Section 4-1 and its application to convected coordinates in Section 4-2.

4-1 Strain-Displacement Relation

The relation between the displacement of the membrane and the total strain in the membrane is developed in this section. This relation is required as the strains determine the stresses in the membrane by the material law and consequently these strains affect the state of the membrane.

A membrane is a two-dimensional surface in three dimensional space $\mathbb{R}^3$, which means that a material point inside the membrane can be described by only two coordinates when choosing the first to basis vectors of the coordinate frame parallel to the membrane. The reference, or initial, configuration of the membrane is described by the vector $\boldsymbol{r}_0(\xi^\alpha)$, $\alpha = 1, 2$. Note that Greek indices are used to denote the reference configuration. The coordinates ξ^α uniquely defines a certain material point of the membrane in the coordinate system whose covariant basis vectors $\boldsymbol{a}_\alpha$ are defined by:

$$\boldsymbol{a}_\alpha = \frac{\partial \boldsymbol{r}_0}{\partial \xi^\alpha} \tag{4-1}$$

Note that these basis vectors are not unit vectors in general nor are they orthogonal. The vector pointing towards a neighboring material point in the reference configuration is given

in Equation (4-2):

$$\begin{aligned} d\boldsymbol{r}_0 &= \boldsymbol{r}_0\left(\xi^\alpha + d\xi^\alpha\right) - \boldsymbol{r}_0\left(\xi^\alpha\right) \\ &= \boldsymbol{r}_0\left(\xi^\alpha\right) + \boldsymbol{a}_\alpha d\xi^\alpha - \boldsymbol{r}_0\left(\xi^\alpha\right) \\ &= \boldsymbol{a}_\alpha d\xi^\alpha \end{aligned} \tag{4-2}$$

The inner product of this vector with itself yields the squared norm of this vector dl_0^2:

$$dl_0^2 = d\boldsymbol{r}_0 \cdot d\boldsymbol{r}_0 = \boldsymbol{a}_\alpha \cdot \boldsymbol{a}_\beta d\xi^\alpha d\xi^\beta = G_{0\alpha\beta} d\xi^\alpha d\xi^\beta \tag{4-3}$$

with $G_{0\alpha\beta}$ being the metric tensor in the reference configuration:

$$G_{0\alpha\beta} = \boldsymbol{a}_\alpha \cdot \boldsymbol{a}_\beta \tag{4-4}$$

Upon the application of a force or displacement loading the membrane deforms from its reference configuration into the current configuration. When this configuration is described in the same coordinate system as the initial configuration, three coordinates are required since the membrane may have deformed in the normal direction. In general a different coordinate frame is applied in the current configuration in which three coordinates are required to describe the position of the membrane: $\boldsymbol{r}\left(x^i\right)$, $i = 1, 2, 3$. The covariant basis vectors of this current coordinate frame $\boldsymbol{b}_i$ are then:

$$\boldsymbol{b}_i = \frac{\partial \boldsymbol{r}}{\partial x^i} \tag{4-5}$$

A vector pointing towards a neighboring material point in the current configuration is given as shown in Equation (4-6):

$$d\boldsymbol{r} = \boldsymbol{b}_i dx^i \tag{4-6}$$

The squared norm dl^2 of this vector then becomes:

$$dl^2 = d\boldsymbol{r} \cdot d\boldsymbol{r} = \boldsymbol{b}_i \cdot \boldsymbol{b}_j dx^i dx^j = G_{ij} dx^i dx^j = d\boldsymbol{x}^T \boldsymbol{G} d\boldsymbol{x} \tag{4-7}$$

with G_{ij} being the metric tensor in the current configuration:

$$G_{ij} = \boldsymbol{b}_i \cdot \boldsymbol{b}_j \tag{4-8}$$

The strain induced by the motion from the reference to the current configuration consists of two parts. First the change in coordinates from ξ^α to x^i contributes to the strain and secondly the change in basis vectors has an effect. The change in coordinates is represented by the deformation gradient $\boldsymbol{F} = F^i_\alpha \boldsymbol{a}^\alpha \boldsymbol{b}_i$ as defined in Equation (4-9):

$$dx^i = \frac{\partial x^i}{\partial \xi^\alpha} d\xi^\alpha = F^i_\alpha d\xi^\alpha \tag{4-9}$$

The ranges of the indices α and i show that the deformation gradient is represented by a 3×2 matrix, as has been applied in Section 3-3. Consequently, $\boldsymbol{F}$ has a null space along the normal of the membrane. This null space is spanned by the vectors $\boldsymbol{u}$ for which the pull back by the deformation gradient equals zero: $\boldsymbol{F}^T \boldsymbol{u} = \boldsymbol{0}$.

The strain in the membrane is related to the change in length of the fibers from the reference to the current configuration, which have been calculated in Equations (4-3) and

(4-7) respectively. Equation (4-10) shows the definition of the Green-Lagrange strain tensor $\boldsymbol{E} = E_{\alpha\beta}\boldsymbol{a}^{\alpha}\boldsymbol{a}^{\beta}$ based on this change in length of fibers:

$$\begin{aligned}\frac{1}{2}\left(dl^2 - dl_0^2\right) &= \frac{1}{2}\left(G_{ij}dx^i dx^j - G_{0\alpha\beta}d\xi^{\alpha}d\xi^{\beta}\right)\\ &= \frac{1}{2}\left(G_{ij}F^i_{\alpha}F^j_{\beta} - G_{0\alpha\beta}\right)d\xi^{\alpha}d\xi^{\beta}\\ &= E_{\alpha\beta}d\xi^{\alpha}d\xi^{\beta}\end{aligned} \tag{4-10}$$

Using the concepts of tensor analysis $\boldsymbol{E}$ is written in tensor and matrix notation:

$$\boldsymbol{E} = \frac{1}{2}\left(\boldsymbol{F}^T\boldsymbol{F} - \boldsymbol{I}\right); \qquad [\boldsymbol{E}] = \frac{1}{2}\left([\boldsymbol{F}]^T[\boldsymbol{G}][\boldsymbol{F}] - [\boldsymbol{G}_0]\right) \tag{4-11}$$

which shows $\boldsymbol{E}$ is defined in the reference configuration and is a 2×2 symmetric tensor, meaning $E_{\alpha\beta} = E_{\beta\alpha}$. Equation (4-11) contains the most general relation between strain and displacement in the membrane. The matrix notation shows that the strain is described by the change in coordinates $[\boldsymbol{F}]$ and by the change in coordinate bases, represented by $[\boldsymbol{G}]$ and $[\boldsymbol{G}_0]$.

4-2 Convected Coordinates

The coordinate frame in the reference configuration in Section 4-1 was chosen such that the first two basis vectors are parallel to the membrane. In convected coordinates this same choice is made in the current configuration. More specifically the coordinates in the current configuration are chosen to be the same as in the initial configuration, i.e. $x^i = \xi^{\alpha}$, $i = 1, 2$ and $x^3 = 0$. Consequently the components of the deformation gradient and the term $[\boldsymbol{F}]^T[\boldsymbol{G}][\boldsymbol{F}]$ become:

$$[\boldsymbol{F}] = \begin{bmatrix}1 & 0\\ 0 & 1\\ 0 & 0\end{bmatrix}; \qquad [\boldsymbol{F}]^T[\boldsymbol{G}][\boldsymbol{F}] = [\boldsymbol{G}]_{2\times 2} \tag{4-12}$$

This choice of coordinates means that the basis vectors in the current configuration need to be chosen such that the correct deformation field is represented. For this purpose note that the position vector in the current configuration can be written as:

$$\boldsymbol{r}(\boldsymbol{\xi}) = \boldsymbol{r}_0(\boldsymbol{\xi}) + \boldsymbol{u}(\boldsymbol{\xi}) \tag{4-13}$$

in which $\boldsymbol{u}$ is the displacement vector. The basis vectors $\boldsymbol{b}_1$ and $\boldsymbol{b}_2$ follow from this expression to be:

$$\boldsymbol{b}_1 = \boldsymbol{a}_1 + \frac{\partial \boldsymbol{u}}{\partial \boldsymbol{\xi}_1} = \boldsymbol{a}_1 + \boldsymbol{u}_{,1} \tag{4-14}$$

$$\boldsymbol{b}_2 = \boldsymbol{a}_2 + \boldsymbol{u}_{,2} \tag{4-15}$$

The basis vectors are combined in matrix form as shown in Equations (4-16) and (4-17) for the reference and current configuration respectively. Note that in the remaining of this section the the matrix notation is applied, whilst omitting the [..] brackets:

$$\boldsymbol{A}_0 = \begin{bmatrix}\boldsymbol{a}_1 & \boldsymbol{a}_2\end{bmatrix} \tag{4-16}$$

$$\boldsymbol{A} = \begin{bmatrix}\boldsymbol{b}_1 & \boldsymbol{b}_2\end{bmatrix} = \begin{bmatrix}\boldsymbol{a}_1 & \boldsymbol{a}_2\end{bmatrix} + \begin{bmatrix}\boldsymbol{u}_{,1} & \boldsymbol{u}_{,2}\end{bmatrix} = \boldsymbol{A}_0 + \boldsymbol{D} \tag{4-17}$$

The components of the strain tensor can now be expressed from Equations (4-11) and (4-12):

$$\begin{aligned}\boldsymbol{E} &= \frac{1}{2}\left(\boldsymbol{G} - \boldsymbol{G}_0\right) \\ &= \frac{1}{2}\left[\left(\boldsymbol{A}_0 + \boldsymbol{D}\right)^T\left(\boldsymbol{A}_0 + \boldsymbol{D}\right) - \boldsymbol{A}_0^T\boldsymbol{A}_0\right] \\ &= \frac{1}{2}\left(\boldsymbol{A}_0^T\boldsymbol{A}_0 + \boldsymbol{A}_0^T\boldsymbol{D} + \boldsymbol{D}^T\boldsymbol{A}_0 + \boldsymbol{D}^T\boldsymbol{D} - \boldsymbol{A}_0^T\boldsymbol{A}_0\right) \\ &= \frac{1}{2}\left(\boldsymbol{A}_0^T\boldsymbol{D} + \boldsymbol{D}^T\boldsymbol{A}_0\right) + \frac{1}{2}\boldsymbol{D}^T\boldsymbol{D}\end{aligned} \tag{4-18}$$

Writing out the components of this strain tensor gives Equation (4-19):

$$\boldsymbol{E} = \frac{1}{2}\begin{bmatrix} 2\boldsymbol{a}_1\cdot\boldsymbol{u}_{,1} & \boldsymbol{a}_1\cdot\boldsymbol{u}_{,2} + \boldsymbol{a}_2\cdot\boldsymbol{u}_{,1} \\ \boldsymbol{a}_1\cdot\boldsymbol{u}_{,2} + \boldsymbol{a}_2\cdot\boldsymbol{u}_{,1} & 2\boldsymbol{a}_2\cdot\boldsymbol{u}_{,2}\end{bmatrix} + \frac{1}{2}\begin{bmatrix}\boldsymbol{u}_{,1}\cdot\boldsymbol{u}_{,1} & \boldsymbol{u}_{,1}\cdot\boldsymbol{u}_{,2} \\ \boldsymbol{u}_{,2}\cdot\boldsymbol{u}_{,1} & \boldsymbol{u}_{,2}\cdot\boldsymbol{u}_{,2}\end{bmatrix} \tag{4-19}$$

In practice the strain tensor is written in Voigt form where engineering strains are used. This gives the engineering strains as shown in Equation (4-20):

$$\boldsymbol{\varepsilon} = \begin{pmatrix}\varepsilon_1 \\ \varepsilon_2 \\ \gamma_{12}\end{pmatrix} = \begin{pmatrix}E_{11} \\ E_{22} \\ 2E_{12}\end{pmatrix} = \begin{pmatrix}\boldsymbol{a}_1\cdot\boldsymbol{u}_{,1} \\ \boldsymbol{a}_2\cdot\boldsymbol{u}_{,2} \\ \boldsymbol{a}_1\cdot\boldsymbol{u}_{,2} + \boldsymbol{a}_2\cdot\boldsymbol{u}_{,1}\end{pmatrix} + \frac{1}{2}\begin{pmatrix}\boldsymbol{u}_{,1}\cdot\boldsymbol{u}_{,1} \\ \boldsymbol{u}_{,2}\cdot\boldsymbol{u}_{,2} \\ \boldsymbol{u}_{,1}\cdot\boldsymbol{u}_{,2} + \boldsymbol{u}_{,2}\cdot\boldsymbol{u}_{,1}\end{pmatrix} \tag{4-20}$$

Chapter 5

Membrane Equilibrium

In its deformed configuration the physical membrane is considered to be in equilibrium. The equilibrium conditions which uniquely describe this deformed configuration are presented in this chapter. First, the general equilibrium equations in mechanics are considered in Section 5-1 by formulating the total potential energy which is to be minimized. For membranes this energy minimization is unstable in case compressive stresses occur, which leads to the different membrane states described in Section 5-2. The definition of the relaxed strain energy function in Section 5-3 solves the instability in energy minimization. The minimization of total potential energy is then performed in Section 5-4. The membrane structure is discretized and the governing equations derived from the energy minimization are linearized in Section 5-5. Finally, the Hu-Washizu principle is presented in Section 5-6 as an alternative for the principle of minimizing total potential energy.

5-1 General Equilibrium Equations

The general equilibrium conditions in continuum mechanics are considered in this section. The same notation is used as before, meaning that the strain energy in the material is denoted by $\phi(\boldsymbol{E}) = \phi(\boldsymbol{E}(\boldsymbol{F})) = \psi(\boldsymbol{F})$. In the remainder of this thesis it is assumed that $\phi(\boldsymbol{E})$ is convex, which is the case when the stress-stain relation is one-to-one [2, 25]. The first and second Piola-Kirchhoff stress tensors are given as in (5-1) and (5-2) respectively:

$$\boldsymbol{P} = P_i^\alpha \boldsymbol{a}_\alpha \boldsymbol{b}^i \qquad\qquad P_i^\alpha = \frac{d\psi}{dF_\alpha^i} \tag{5-1}$$

$$\boldsymbol{S} = S^{\alpha\beta} \boldsymbol{a}_\alpha \boldsymbol{a}_\beta \qquad\qquad S^{\alpha\beta} = \frac{d\phi}{dE_{\alpha\beta}} \tag{5-2}$$

Note that the symmetry of $\boldsymbol{E}$ implies that $\boldsymbol{S}$ is symmetric as well. The relation between $\boldsymbol{P}$ and $\boldsymbol{S}$ has been shown in Appendix A to be:

$$P_i^\alpha = G_{ij} F_\gamma^j S^{\gamma\alpha} \qquad \Rightarrow \quad \boldsymbol{P} = \boldsymbol{F}\boldsymbol{S} \tag{5-3}$$

The strong form of the equilibrium equations, which need to be satisfied for each material point, is given as [16]:

$$P^{\alpha}_{i,\alpha} + b_i = 0 \qquad \Rightarrow \qquad \nabla \cdot \boldsymbol{P} + \boldsymbol{b} = \boldsymbol{0} \tag{5-4}$$

with $\boldsymbol{b}$ being the external force and $\nabla\cdot$ denoting the divergence operator. Solving this equation for each material point exactly is not possible in general. Alternatively a weak form of this equilibrium equation can be formulated, which in this case is the minimization of the total potential energy $\mathit{\Pi}(\boldsymbol{u})$ in the membrane:

$$\mathit{\Pi}(\boldsymbol{u}) = \int_{\Omega} \phi(\boldsymbol{E}(\boldsymbol{u}))d\Omega - \int_{\Omega} \boldsymbol{b}\cdot\boldsymbol{u}d\Omega - \int_{\partial\Omega} \boldsymbol{t}\cdot\boldsymbol{u}d\partial\Omega \tag{5-5}$$

in which Ω is the reference domain of the membrane and $\partial\Omega$ is the boundary of this domain. The parameter $\boldsymbol{u}$ denotes the displacement field and $\boldsymbol{b}$ and $\boldsymbol{t}$ represent body forces and boundary tractions respectively. The displacement field minimizing the potential energy is a physically stable state of the membrane:

$$\boldsymbol{u} = \underset{\bar{\boldsymbol{u}}}{\operatorname{arginf}}\, \mathit{\Pi}(\bar{\boldsymbol{u}})$$

A unique solution for this displacement field can only exist when boundary conditions are prescribed:

$$\boldsymbol{P}\cdot\boldsymbol{n} = \boldsymbol{t}_p \qquad \text{at } \partial\Omega_{\sigma} \tag{5-6}$$

$$\boldsymbol{u} = \boldsymbol{u}_p \qquad \text{at } \partial\Omega_{u} \tag{5-7}$$

in which $\partial\Omega_{\sigma}$ and $\partial\Omega_{u}$ represent the parts of the boundary where tractions $\boldsymbol{t}_p$ or displacements $\boldsymbol{u}_p$ are prescribed and $\boldsymbol{n}$ is the normal vector to the boundary.

The existence and uniqueness of the energy minimizing displacement field requires quasi-convexity of $\psi(\boldsymbol{F})$, which is weaker than convexity and stronger than rank-one convexity as shown in Chapter 3. Pipkin [25] shows that when compressive stresses ($\boldsymbol{S} < \boldsymbol{0}$) develop in membranes this requirement of quasi-convexity is violated and the energy minimization becomes unstable. This results from the zero bending stiffness of the membranes causing immediate wrinkling upon compression. Based on this characteristic three different states of the membrane are distinguished which have been presented in the next section.

5-2 Membrane States

Any compressive stresses in the membrane immediately lead to wrinkling as mentioned previously. Consequently, also the post-buckling bending stiffness of the membrane equals zeros and the only load carrying capabilities of the membrane are along the tension direction. As a result the membrane exists in one of its three possible states: taut, wrinkled or slack. In the taut state the membrane is under pure tension and behaves as a regular shell, the slack state represents a pure compression in which the membrane has no load carrying capabilities. In the wrinkled state the membrane is tense in one direction and slack in the perpendicular direction and can thus only carry loads along the tensile direction. An overview of the three different possible membrane states is given in Figure 5-1.

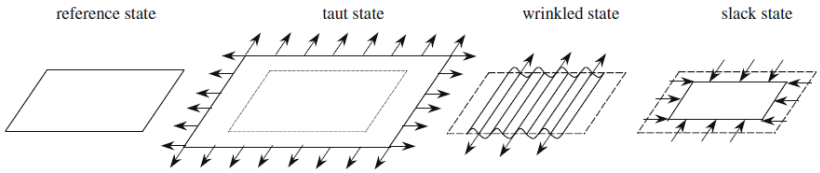

Figure 5-1: Overview of membrane states: taut, wrinkled and slack [11].

From Figure 5-1 it can be seen that the wrinkles are of out of plane displacements, which are modeled as a continuous in-plane contraction of the membrane in the tension field theory as visualized in Figure 5-2.

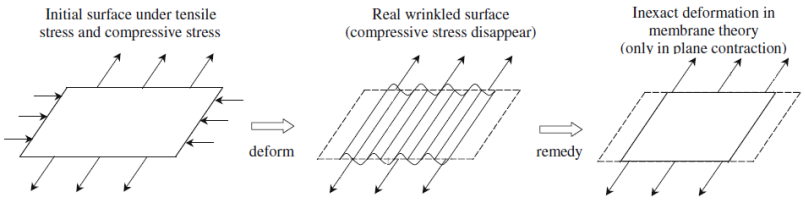

Figure 5-2: Membrane wrinkling modeled as in-plane contraction [11].

In the wrinkled region of the membrane there are no stresses in the direction of the in-plane contraction and the stresses in the perpendicular stresses are tensile. Consequently, the slack regions of the membrane carry zero stresses. Note that in the tension field theory method the plane stress assumption is applied to the membrane. Modeling the wrinkled membrane using this tension field theory method allows the mesh size in e.g. a finite element method to be much larger than individual wrinkles, which leads to significant savings in computational costs.

5-3 Relaxed Strain Energy Function

Compressive stresses in membranes ($\boldsymbol{S} < \boldsymbol{0}$) lead to an unstable potential energy minimization as $\psi(\boldsymbol{F})$ is not quasi-convex. The introduction of the relaxed strain energy function leads to the required quasi-convexity of $\psi(\boldsymbol{F})$ as has been demonstrated in Section 3-3. This enables a stable energy minimization, whereas wrinkling of the membrane is taken into account using an in-plane contraction with zero strain energy. The minimum of the relaxation is equal to the minimum of $\psi(\boldsymbol{F})$ given that $\phi(\boldsymbol{E})$ is convex as assumed.

The relaxed strain energy function $\phi^\sharp(\boldsymbol{E})$ which leads to the required quasi-convexification of $\psi(\boldsymbol{F})$ is presented in this section. The definition of the relaxed strain energy function results in governing equations for stresses and strains in the membrane in the form of an optimization problem.

The displacement field $\boldsymbol{F}$ is assumed to be known in this section, which results in the strain tensor $\boldsymbol{E}$ from Equation (3-30). This strain tensor contains the total strain in the membrane, part of which may be wrinkling strain which carries zero strain energy. This wrinkling strain, denoted by $\hat{\boldsymbol{E}}$, is a variable whose value is determined by the equations presented in this

section. A wrinkle causes $\hat{\boldsymbol{E}}$ to be positive, therefore the total elastic strain in the membrane is given as $\boldsymbol{E} + \hat{\boldsymbol{E}}$. The stresses in the membrane are caused by these elastic strains only, meaning that the second Piola-Kirchhoff stress tensor is as shown in Equation (5-8).

$$\boldsymbol{S} = \left.\frac{\partial \phi}{\partial \boldsymbol{E}}\right|_{\boldsymbol{E}+\hat{\boldsymbol{E}}} \tag{5-8}$$

Note that $\boldsymbol{S}$ is not a variable in itself as it follows directly from the known strain energy function, however, the actual stress in the membrane is a variable and denoted by $\hat{\boldsymbol{S}}$. In the equilibrium state the actual stress in the membrane is equal to the stress tensor obtained from the strain energy function in Equation (5-8).

The final variable used in this section is the slack strain $\tilde{\boldsymbol{E}}$, which will be needed to formulate the governing equations. As the name already indicates this strain will be related to the wrinkling strain $\hat{\boldsymbol{E}}$. An overview of the definitions given in this section is shown in Table 5-1.

Parameter	Description
$\boldsymbol{F}$	Deformation gradient which is assumed to be known.
$\boldsymbol{E}$	Total strain in membrane as a function $\boldsymbol{F}$.
$\hat{\boldsymbol{E}}$	Variable defining the wrinkling strain.
$\tilde{\boldsymbol{E}}$	Variable defining the slack strain.
$\boldsymbol{S}$	Second Piola-Kirchhoff stress tensor as derived from the known strain energy function.
$\hat{\boldsymbol{S}}$	Variable defining the actual stress in the membrane.

Table 5-1: Overview of the parameter descriptions

The expression for the relaxation of any function $f(\boldsymbol{X})$ was presented in Section 3-4. This relaxation $f^\sharp(\boldsymbol{X})$ was shown to be the lower, convex and non-decreasing envelope of $f(\boldsymbol{X})$. In the former Section 3-3 it was shown that the relaxation of the strain energy function is sufficient to guarantee a stable equilibrium state in a membrane.

Combining these results leads to the relaxed strain energy function $\phi^\sharp(\boldsymbol{E})$ which forms the lower, convex and non-decreasing bound of the strain energy function. The expression for $\phi^\sharp(\boldsymbol{E})$ is obtained from Equation (3-38) by substituting $\boldsymbol{X} = \boldsymbol{E}$, $\boldsymbol{Y} = \hat{\boldsymbol{S}}$ and $\boldsymbol{Z} = \hat{\boldsymbol{E}}$:

$$\phi^\sharp(\boldsymbol{E}) = \sup_{\hat{\boldsymbol{S}} \geq \boldsymbol{0}} \left[\hat{\boldsymbol{S}} : \boldsymbol{E} - \phi^*(\hat{\boldsymbol{S}}) \right] \tag{5-9}$$

As mentioned in Section 5-1, the strain energy function is assumed to be convex. Under this assumption $\phi^\sharp(\boldsymbol{E})$ can be rewritten based on Equation (3-45):

$$\phi^\sharp(\boldsymbol{E}) = \sup_{\hat{\boldsymbol{S}} \geq \boldsymbol{0}} \inf_{\hat{\boldsymbol{E}}} \left[\phi(\boldsymbol{E} + \hat{\boldsymbol{E}}) - \hat{\boldsymbol{S}} : \hat{\boldsymbol{E}} \right] \tag{5-10}$$

This is a constrained optimization problem with the variables $\hat{\boldsymbol{S}}$ and $\hat{\boldsymbol{E}}$. The constraint $\hat{\boldsymbol{S}} > \boldsymbol{0}$ states that the stress has to be positive, which is the same result as obtained by Pipkin [25]. In standard optimization terminology $\hat{\boldsymbol{E}}$ is the primal and $\hat{\boldsymbol{S}}$ is the dual variable.

Due to the constraint this optimization problem cannot be solved by equating the derivatives

with respect to the variables $\hat{\boldsymbol{S}}$ and $\hat{\boldsymbol{E}}$ to zero. To resolve this the slack strain $\tilde{\boldsymbol{E}}$ is introduced in the expression for the relaxed strain energy:

$$\begin{aligned}\phi^\sharp(\boldsymbol{E}) &= \sup_{\hat{\boldsymbol{S}}} \inf_{\hat{\boldsymbol{E}}} \left[\phi(\boldsymbol{E}+\hat{\boldsymbol{E}}) - \hat{\boldsymbol{S}} : \hat{\boldsymbol{E}} + \inf_{\tilde{\boldsymbol{E}}\geq \boldsymbol{0}} \hat{\boldsymbol{S}} : \tilde{\boldsymbol{E}} \right] \\ &= \sup_{\hat{\boldsymbol{S}}} \inf_{\hat{\boldsymbol{E}},\tilde{\boldsymbol{E}}\geq \boldsymbol{0}} \left[\phi(\boldsymbol{E}+\hat{\boldsymbol{E}}) - \hat{\boldsymbol{S}} : \left(\hat{\boldsymbol{E}} - \tilde{\boldsymbol{E}} \right) \right] \end{aligned} \tag{5-11}$$

This is equivalent to Equation (5-10), which follows from:

$$\inf_{\tilde{\boldsymbol{E}}\geq \boldsymbol{0}} \hat{\boldsymbol{S}} : \tilde{\boldsymbol{E}} = \begin{cases} 0 & \text{if } \hat{\boldsymbol{S}} \geq 0 \\ -\infty & \text{if } \hat{\boldsymbol{S}} < 0 \end{cases} \tag{5-12}$$

and hence:

$$\sup_{\hat{\boldsymbol{S}}} \left[\inf_{\tilde{\boldsymbol{E}}\geq \boldsymbol{0}} \hat{\boldsymbol{S}} : \tilde{\boldsymbol{E}} \right] = 0 \quad \text{with } \hat{\boldsymbol{S}} \geq 0 \tag{5-13}$$

So the extra contribution of Equation (5-12) is merely the addition of zero and it ensures that $\hat{\boldsymbol{S}} \geq 0$ as shown in Equation (5-13), however, with this addition the optimization problem is still a constrained problem. For this reason the problem is to be rewritten as an unconstrained optimization problem, for which the interior point method [4, 35, 41] is applied. In this method a barrier function which equals 0 in the feasible region ($\tilde{\boldsymbol{E}} \geq 0$) and ∞ elsewhere, is added to the objective function. A convex function $\kappa(\tilde{\boldsymbol{E}})$ which approaches these properties is shown below:

$$\kappa(\tilde{\boldsymbol{E}}) = \begin{cases} -\lim_{\mu\to 0_+} \mu \ln \left| \tilde{\boldsymbol{E}} \right| & \text{if } \tilde{\boldsymbol{E}} > 0 \\ \infty & \text{elsewhere} \end{cases} \tag{5-14}$$

Note that because this function is convex the optimization problem retains its convexity properties. This is also the reason for introducing the slack strain instead of applying the barrier function on $\hat{\boldsymbol{S}}$ directly in Equation (5-10). In that case the barrier function would be concave.

The case of $\tilde{\boldsymbol{E}} \leq 0$ can be ignored provided that in the implementation the initial choice for $\tilde{\boldsymbol{E}}$ is positive. The optimization algorithm then prevents $\tilde{\boldsymbol{E}}$ to become negative as the barrier function goes to infinity when $\tilde{\boldsymbol{E}}$ approaches zero in the limit. By ignoring the case of $\tilde{\boldsymbol{E}} \leq 0$, the unconstrained form of the relaxed strain energy becomes as shown in Equation (5-15):

$$\phi^\sharp(\boldsymbol{E}) = \lim_{\mu\to 0_+} \sup_{\hat{\boldsymbol{S}}} \inf_{\hat{\boldsymbol{E}},\tilde{\boldsymbol{E}}} \left[\phi(\boldsymbol{E}+\hat{\boldsymbol{E}}) - \hat{\boldsymbol{S}} : \left(\hat{\boldsymbol{E}} - \tilde{\boldsymbol{E}} \right) - \mu \ln \left| \tilde{\boldsymbol{E}} \right| \right] \tag{5-15}$$

It should be noted that this formulation is not fully equivalent to Equation (5-11). The reason being that the case of $\tilde{\boldsymbol{E}} = \boldsymbol{0}$ leads to infinite relaxed strain energy in the current formulation whereas it does not in Equation (5-11), however, this issue resolves itself when linearizing the governing equations in Section 5-5. Rewriting Equation (5-15) gives:

$$\phi^\sharp(\boldsymbol{E}) = \lim_{\mu\to 0_+} \sup_{\hat{\boldsymbol{S}}} \inf_{\hat{\boldsymbol{E}},\tilde{\boldsymbol{E}}} \chi(\boldsymbol{E}, \hat{\boldsymbol{E}}, \tilde{\boldsymbol{E}}, \hat{\boldsymbol{S}}; \mu) \tag{5-16}$$

with:

$$\chi(\boldsymbol{E}, \hat{\boldsymbol{E}}, \tilde{\boldsymbol{E}}, \hat{\boldsymbol{S}}; \mu) = \phi(\boldsymbol{E}+\hat{\boldsymbol{E}}) - \hat{\boldsymbol{S}} : \left(\hat{\boldsymbol{E}} - \tilde{\boldsymbol{E}} \right) - \mu \ln \left| \tilde{\boldsymbol{E}} \right| \tag{5-17}$$

This relaxed strain energy contributes to the total potential energy in the membrane, which is be minimized to obtain the equilibrium state of the membrane.

5-4 Potential Energy Minimization

The relaxed strain energy function $\phi^\sharp(\boldsymbol{E})$ which leads to a stable solution of the total potential energy minimization in the membrane, has been presented in Section 5-3. In this section this minimization is performed with respect to the four variables $\hat{\boldsymbol{E}}$, $\tilde{\boldsymbol{E}}$, $\hat{\boldsymbol{S}}$ and $\boldsymbol{E}(\boldsymbol{u})$.

The total potential energy in the membrane is obtained by replacing the strain energy function in Equation (5-5) by its relaxation $\phi^\sharp(\boldsymbol{E})$:

$$\mathit{\Pi}(\boldsymbol{u}) = \int_\Omega \phi^\sharp(\boldsymbol{E}(\boldsymbol{u}))d\Omega - \int_\Omega \boldsymbol{b}\cdot\boldsymbol{u}d\Omega - \int_{\partial\Omega} \boldsymbol{t}\cdot\boldsymbol{u}d\partial\Omega \tag{5-18}$$

With the definition of the relaxation in Equations (5-16) and (5-17), the potential energy functional becomes:

$$\mathit{\Pi}(\hat{\boldsymbol{E}},\tilde{\boldsymbol{E}},\hat{\boldsymbol{S}},\boldsymbol{u};\mu) = \int_\Omega \chi(\boldsymbol{E},\hat{\boldsymbol{E}},\tilde{\boldsymbol{E}},\hat{\boldsymbol{S}};\mu)d\Omega - \int_\Omega \boldsymbol{b}\cdot\boldsymbol{u}d\Omega - \int_{\partial\Omega} \boldsymbol{t}\cdot\boldsymbol{u}d\partial\Omega \tag{5-19}$$

and the minimum potential energy is then defined as:

$$\lim_{\mu\to 0_+} \sup_{\hat{\boldsymbol{S}}} \inf_{\hat{\boldsymbol{E}},\tilde{\boldsymbol{E}},\boldsymbol{u}} \mathit{\Pi}(\hat{\boldsymbol{E}},\tilde{\boldsymbol{E}},\hat{\boldsymbol{S}},\boldsymbol{u};\mu) \tag{5-20}$$

The equilibrium configuration of the membrane is represented by the values of the variables for which these *sup* and *inf* operators are obtained. These operators are satisfied if the first order variation of the potential energy equals zeros, which gives:

$$\begin{aligned}\delta\Pi = &\int_\Omega \left(\boldsymbol{S}-\hat{\boldsymbol{S}}\right) : \delta\hat{\boldsymbol{E}}d\Omega \\ &+ \int_\Omega \left(\hat{\boldsymbol{S}}-\mu\tilde{\boldsymbol{E}}^{-1}\right) : \delta\tilde{\boldsymbol{E}}d\Omega \\ &+ \int_\Omega \left(\hat{\boldsymbol{E}}-\tilde{\boldsymbol{E}}\right) : \delta\hat{\boldsymbol{S}}d\Omega \\ &+ \int_\Omega \frac{\partial\phi}{\partial\boldsymbol{u}}\cdot\delta\boldsymbol{u}d\Omega - \int_\Omega \boldsymbol{b}\cdot\delta\boldsymbol{u}d\Omega - \int_{\partial\Omega}\boldsymbol{t}\cdot\delta\boldsymbol{u}d\partial\Omega = 0\end{aligned} \tag{5-21}$$

Applying the localization theorem to the first three integrals yields that all terms within the brackets in these integrals need to be equal to zero. After eliminating $\tilde{\boldsymbol{E}}$, the first two governing equations for $\hat{\boldsymbol{S}}$ and $\hat{\boldsymbol{E}}$ are then obtained:

$$\boldsymbol{S}-\hat{\boldsymbol{S}} = \boldsymbol{0} \tag{5-22}$$

$$\hat{\boldsymbol{E}}\hat{\boldsymbol{S}} = \mu\boldsymbol{I} \tag{5-23}$$

The physical interpretation of Equation (5-22) is merely the confirmation of the fact that in equilibrium the actual stress in the membrane $\hat{\boldsymbol{S}}$ is equal to the value obtained from the strain energy function at an elastic strain of $\boldsymbol{E}+\hat{\boldsymbol{E}}$.

In the limit of μ going to zero, Equation (5-23) can be interpreted to be $\hat{\boldsymbol{E}}\hat{\boldsymbol{S}} = \boldsymbol{0}$, which can be satisfied in three different ways, corresponding to the three different states of the membrane. First this equation is satisfied when the wrinkling strain $\hat{\boldsymbol{E}} = \boldsymbol{0}$, which corresponds to the taut membrane state. Secondly the equation is satisfied when $\hat{\boldsymbol{S}} = 0$, corresponding to the slack state of the membrane. In between these two states is the wrinkled state, which occurs when $\hat{\boldsymbol{E}}$ and $\hat{\boldsymbol{S}}$ are rank-one tensors with perpendicular eigenvectors. In this case the

stress is perpendicular to the wrinkling strain and Equation (5-23) is satisfied. Note that in standard optimization terms, satisfying Equation (5-23) means that the duality gap of the primal-dual optimization problem is zero.

For a given displacement field in the membrane, Equations (5-22) and (5-23) can be solved for $\hat{\boldsymbol{E}}$ and $\hat{\boldsymbol{S}}$ using the relations given in Equations (4-11) and (5-8). In order to determine the displacement which minimizes the total potential energy, the integrals containing $\delta \boldsymbol{u}$ in Equation (5-21) are considered. Let $\boldsymbol{B} = \frac{\partial \boldsymbol{E}}{\partial \boldsymbol{u}}$ and $\boldsymbol{f}$ be the force vector containing the integrations over $\boldsymbol{b}$ and $\boldsymbol{t}$ to give the third governing equation:

$$\int_{\Omega} \boldsymbol{B}^T \boldsymbol{S} d\Omega - \boldsymbol{f} = 0 \tag{5-24}$$

Note that this equation contains an integral over the domain, i.e. the volume, of the membrane and is thus defined on a global level. After applying consistent boundary conditions, Equations (5-22), (5-23) and (5-24) uniquely describe the displacements, wrinkling strains and stresses in the membrane. The solution to this set of non-linear equations is obtained by linearization of the equations.

5-5 Discretization and Linearization

Discretization and linearization of the governing equations is required to find the solution for the membrane displacements, stresses and strains. The former is needed as the governing equations contain an integral over the volume of the membrane which cannot be evaluated directly. The non-linearity of the governing equations requires a linearization of these equations.

5-5-1 Discretization

The third governing equation presented in (5-24) is defined as an integral over the complete volume of the membrane and consequently needs to be satisfied on a global level. In general it is not possible to evaluate the integral over the complete membrane directly, which is why discretization of the membrane structure is applied. The discretization is performed using finite elements which are widely used in mechanics as they can provide good approximations for the behavior of complex structures. The position of a material point in the reference configuration $\boldsymbol{r}_0$ and its displacements $\boldsymbol{u}$ are represented by a set of shape functions $\boldsymbol{N}$ for each finie element:

$$\boldsymbol{r}_0(\boldsymbol{\xi}) = \boldsymbol{N}(\boldsymbol{\xi})\, \boldsymbol{\rho}_0 \tag{5-25}$$

$$\boldsymbol{u}(\boldsymbol{\xi}) = \boldsymbol{N}(\boldsymbol{\xi})\, \boldsymbol{v} \tag{5-26}$$

in which $\boldsymbol{\rho}_0$ and $\boldsymbol{v}$ are the nodal position and displacement vectors respectively. Two distinct branches of finite elements exist, the first of which contains the isoparametric finite element. This branch includes the standard finite elements such as triangular and quadrilateral elements as presented in Chapters 7 and 8 respectively. These isoparametric elements represent the initial configuration only as an approximation and the shape functions are non-zero on a

single element only.

The second branch of finite elements contains the isogeometric element, in which the initial configuration of the membrane is represented exactly. The shape functions are B-splines or NURBS, which are non-zero over multiple elements. These isogeometric elements are presented in Chapter 9.

By substituting the expressions for $\boldsymbol{r}_0$ and $\boldsymbol{u}$ into Equation (4-20) the engineering strains in Voigt form are derived:

$$\boldsymbol{\varepsilon} = \begin{pmatrix} \boldsymbol{\rho}_0^T \boldsymbol{P}_1 \boldsymbol{v} \\ \boldsymbol{\rho}_0^T \boldsymbol{P}_2 \boldsymbol{v} \\ \boldsymbol{\rho}_0^T \boldsymbol{P}_{12} \boldsymbol{v} \end{pmatrix} + \frac{1}{2} \begin{pmatrix} \boldsymbol{v}^T \boldsymbol{P}_1 \boldsymbol{v} \\ \boldsymbol{v}^T \boldsymbol{P}_2 \boldsymbol{v} \\ \boldsymbol{v}^T \boldsymbol{P}_{12} \boldsymbol{v} \end{pmatrix} \tag{5-27}$$

in which:

$$\boldsymbol{P}_1 = \boldsymbol{N}_{,1}^T \boldsymbol{N}_{,1} \tag{5-28a}$$

$$\boldsymbol{P}_2 = \boldsymbol{N}_{,2}^T \boldsymbol{N}_{,2} \tag{5-28b}$$

$$\boldsymbol{P}_{12} = \boldsymbol{N}_{,1}^T \boldsymbol{N}_{,2} + \boldsymbol{N}_{,2}^T \boldsymbol{N}_{,1} \tag{5-28c}$$

The derivative of the strain with respect to the displacement, denoted by $\boldsymbol{B}$ in Section 5-4, can be derived from Equation (5-27) to be:

$$\boldsymbol{B} = \frac{\partial \boldsymbol{\varepsilon}}{\partial \boldsymbol{v}} = \underbrace{\begin{bmatrix} \boldsymbol{\rho}_0^T \boldsymbol{P}_1 \\ \boldsymbol{\rho}_0^T \boldsymbol{P}_2 \\ \boldsymbol{\rho}_0^T \boldsymbol{P}_{12} \end{bmatrix}}_{\boldsymbol{B}_L} + \underbrace{\begin{bmatrix} \boldsymbol{v}^T \boldsymbol{P}_1 \\ \boldsymbol{v}^T \boldsymbol{P}_2 \\ \boldsymbol{v}^T \boldsymbol{P}_{12} \end{bmatrix}}_{\boldsymbol{B}_{NL}} \tag{5-29}$$

In this equation $\boldsymbol{B}_L$ and $\boldsymbol{B}_{NL}$ represent the derivatives of the linear and non-linear part of the strain respectively. An expression which is required for the linearization of the governing equations in Section 5-5-2 is given below:

$$\frac{\partial \boldsymbol{B}^T}{\partial \boldsymbol{v}} \boldsymbol{S} = \begin{bmatrix} \boldsymbol{P}_1 & \boldsymbol{P}_2 & \boldsymbol{P}_{12} \end{bmatrix} \boldsymbol{\sigma} = \sigma_1 \boldsymbol{P}_1 + \sigma_2 \boldsymbol{P}_2 + \tau_{12} \boldsymbol{P}_{12} \tag{5-30}$$

After discretizing the membrane the integral in the governing equation (5-24) is replaced by a numerical integration over the finite elements. This yields the discretized governing equation for a single finite element as:

$$\sum_i \boldsymbol{B}_i^T \boldsymbol{S}_i w_i - \boldsymbol{f} = 0 \tag{5-31}$$

in which i represents the integration points of the element and w_i the numerical weight which is related to the volume of the element and the numerical integration scheme.

5-5-2 Linearization

The governing Equations (5-22), (5-23) and (5-31) form a non-linear set of equations describing the membrane configuration. The solution to this set of equations is obtained by linearization followed by an iterative solving procedure. The linearization of the equations requires three different stiffness tensors to be introduced, which are shown in Table 5-2.

Parameter	Description
C	Material stiffness tensor $= \frac{\partial \boldsymbol{S}}{\partial \boldsymbol{E}}\Big\vert_{\boldsymbol{E}+\hat{\boldsymbol{E}}}$.
H	Wrinkling 'stiffness' tensor s.t. $\mathsf{H}\boldsymbol{A} = \hat{\boldsymbol{E}}^{-1}\boldsymbol{A}\hat{\boldsymbol{S}}\ \forall \boldsymbol{A}$.
C^*	Effective membrane stiffness tensor $= \mathsf{C} - \mathsf{C}\left(\mathsf{C}+\mathsf{H}\right)^{-1}\mathsf{C}$.

Table 5-2: Overview of fourth-order stiffness tensors.

From Table 5-2 it can be seen that when the membrane is unwrinkled, i.e. $\hat{\boldsymbol{E}} = \boldsymbol{0}$, then H approaches infinity and consequently $\mathsf{C}^* = \mathsf{C}$. This demonstrates that the unwrinkled membrane behaves as a regular shell. Linearizing the first governing Equation (5-22) about a current state yields:

$$\begin{aligned} \boldsymbol{S} - \hat{\boldsymbol{S}} &= 0 \\ \Delta\left(\boldsymbol{S} - \hat{\boldsymbol{S}}\right) &= \boldsymbol{R}_\sigma \\ \mathsf{C}\left(\Delta\boldsymbol{E} + \Delta\hat{\boldsymbol{E}}\right) - \Delta\hat{\boldsymbol{S}} &= \boldsymbol{R}_\sigma \end{aligned} \tag{5-32}$$

in which $\boldsymbol{R}_\sigma$ is the stress residue of the governing equation in a particular (non-converged) iteration and C is the fourth order stiffness tensor as defined in Table 5-2. Performing the same linearization procedure on Equation (5-23) gives:

$$\begin{aligned} \hat{\boldsymbol{E}}\hat{\boldsymbol{S}} - \mu\boldsymbol{I} &= 0 \\ \Delta\left(\hat{\boldsymbol{E}}\hat{\boldsymbol{S}} - \mu\boldsymbol{I}\right) &= \boldsymbol{R}_\mu \\ \Delta\hat{\boldsymbol{E}}\hat{\boldsymbol{S}} + \hat{\boldsymbol{E}}\Delta\hat{\boldsymbol{S}} &= \boldsymbol{R}_\mu \end{aligned} \tag{5-33}$$

in which $\boldsymbol{R}_\mu$ is the residue which also contains the $\Delta\hat{\boldsymbol{E}}\Delta\hat{\boldsymbol{S}}$ term. From Equation (5-32) $\Delta\hat{\boldsymbol{E}}$ can be isolated to be:

$$\mathsf{C}\Delta\hat{\boldsymbol{E}} = \Delta\hat{\boldsymbol{S}} + \boldsymbol{R}_\sigma - \mathsf{C}\Delta\boldsymbol{E} \tag{5-34a}$$

$$\Delta\hat{\boldsymbol{E}} = \mathsf{C}^{-1}\Delta\hat{\boldsymbol{S}} + \mathsf{C}^{-1}\boldsymbol{R}_\sigma - \Delta\boldsymbol{E} \tag{5-34b}$$

The same parameter is isolated from Equation (5-33):

$$\hat{\boldsymbol{E}}^{-1}\Delta\hat{\boldsymbol{E}}\hat{\boldsymbol{S}} + \Delta\hat{\boldsymbol{S}} = \hat{\boldsymbol{E}}^{-1}\boldsymbol{R}_\mu \tag{5-35a}$$

$$\mathsf{H}\Delta\hat{\boldsymbol{E}} = -\Delta\hat{\boldsymbol{S}} + \hat{\boldsymbol{E}}^{-1}\boldsymbol{R}_\mu \tag{5-35b}$$

$$\Delta\hat{\boldsymbol{E}} = -\mathsf{H}^{-1}\Delta\hat{\boldsymbol{S}} + \mathsf{H}^{-1}\hat{\boldsymbol{E}}^{-1}\boldsymbol{R}_\mu \tag{5-35c}$$

in which H is the fourth order tensor as defined in Table 5-2. To find an expression for $\Delta\hat{\boldsymbol{E}}$ independent of $\Delta\hat{\boldsymbol{S}}$ one adds Equations (5-34a) and (5-35b) to get:

$$\begin{aligned} \left(\mathsf{C}+\mathsf{H}\right)\Delta\hat{\boldsymbol{E}} &= \boldsymbol{R}_\sigma + \hat{\boldsymbol{E}}^{-1}\boldsymbol{R}_\mu - \mathsf{C}\Delta\boldsymbol{E} \\ \Delta\hat{\boldsymbol{E}} &= \left(\mathsf{C}+\mathsf{H}\right)^{-1}\left(\boldsymbol{R}_\sigma + \hat{\boldsymbol{E}}^{-1}\boldsymbol{R}_\mu - \mathsf{C}\Delta\boldsymbol{E}\right) \end{aligned} \tag{5-36}$$

From this $\Delta\hat{\boldsymbol{S}}$ is obtained by substitution into Equation (5-35a) which results in:

$$\begin{aligned}\Delta\hat{\boldsymbol{S}} &= \hat{\boldsymbol{E}}^{-1}\boldsymbol{R}_\mu - \hat{\boldsymbol{E}}^{-1}\Delta\hat{\boldsymbol{E}}\hat{\boldsymbol{S}} \\ &= \hat{\boldsymbol{E}}^{-1}\left(\boldsymbol{R}_\mu - \Delta\hat{\boldsymbol{E}}\hat{\boldsymbol{S}}\right)\end{aligned} \tag{5-37}$$

To eliminate $\Delta\hat{\boldsymbol{E}}$ from this expression, Equation (5-36) can be substituted, however, a more convenient way is to equate Equations (5-34b) and (5-35c):

$$\begin{aligned}\mathsf{C}^{-1}\Delta\hat{\boldsymbol{S}} + \mathsf{C}^{-1}\boldsymbol{R}_\sigma - \Delta\boldsymbol{E} &= -\mathsf{H}^{-1}\Delta\hat{\boldsymbol{S}} + \mathsf{H}^{-1}\hat{\boldsymbol{E}}^{-1}\boldsymbol{R}_\mu \\ \left(\boldsymbol{C}^{-1} + \mathsf{H}^{-1}\right)\Delta\hat{\boldsymbol{S}} &= \boldsymbol{R}_w + \Delta\boldsymbol{E} \\ \mathsf{C}^{*-1}\Delta\hat{\boldsymbol{S}} &= \boldsymbol{R}_w + \Delta\boldsymbol{E} \\ \Delta\hat{\boldsymbol{S}} &= \mathsf{C}^*\left(\boldsymbol{R}_w + \Delta\boldsymbol{E}\right)\end{aligned} \tag{5-38}$$

with:

$$\boldsymbol{R}_w = \mathsf{H}^{-1}\hat{\boldsymbol{E}}^{-1}\boldsymbol{R}_\mu - \mathsf{C}^{-1}\boldsymbol{R}_\sigma \qquad \text{(only symmetric part)}$$

and C^* being the effective stiffness of the wrinkled membrane as defined in Table 5-2, for which it should be noted that:

$$\mathsf{C}^* = \left(\mathsf{C}^{-1} + \mathsf{H}^{-1}\right)^{-1} = \mathsf{C} - \mathsf{C}\left(\mathsf{C} + \mathsf{H}\right)^{-1}\mathsf{C} \tag{5-39}$$

which can be shown by deriving the expression for $\hat{\boldsymbol{S}}$ by combining Equations (5-34a) and (5-36).

The updates for $\hat{\boldsymbol{E}}$ and $\hat{\boldsymbol{S}}$ in the linearized equations are determined by Equations (5-36) and (5-38) respectively. It should be noted that these update are presented at material point level, which means that in a finite element model they are applied to every integration point separately. This is different for the update of the displacements which is considered next by linearizing the final, discretized governing Equation (5-31). The discretized equation is linearized to obtain an expression for the update of the nodal displacement vector $\Delta\boldsymbol{v}$:

$$\begin{aligned}\Delta\left(\sum_i \boldsymbol{B}_i^T\boldsymbol{S}_i w_i - \boldsymbol{f}\right) &= \boldsymbol{R}_v \\ \sum_i \left(\Delta\boldsymbol{B}_i^T\boldsymbol{S}_i + \boldsymbol{B}_i^T\Delta\boldsymbol{S}_i\right) w_i - \Delta\boldsymbol{f} &= \boldsymbol{R}_v\end{aligned} \tag{5-40}$$

in which $\boldsymbol{R}_v$ is the residue of Equation (5-31), which is often denoted as $\boldsymbol{f}^{ext} - \boldsymbol{f}^{int}$, and $\Delta\boldsymbol{f}$ represents the applied force which is usually non-zero only in the first iteration of the solving procedure. As explained in Section 5-3 the stress tensor $\boldsymbol{S}$ is not a variable and should therefore be replaced by the actual stress in the membrane $\hat{\boldsymbol{S}}$. These two are related by the stress residue $\boldsymbol{R}_\sigma$ introduced in Equation (5-32) as follows:

$$\boldsymbol{S}_i = \hat{\boldsymbol{S}}_i - \boldsymbol{R}_{\sigma_i} \tag{5-41}$$

From this it follows that $\Delta\boldsymbol{S}_i = \Delta\hat{\boldsymbol{S}}_i - \Delta\boldsymbol{R}_{\sigma_i}$, in which the expression $\Delta\boldsymbol{R}_{\sigma_i}$ can be interpreted as second order residue which is assumed to be zero. By applying Equation (5-38) the expression for $\Delta\boldsymbol{S}$ can then be written as shown in Equation (5-42):

$$\Delta\boldsymbol{S}_i = \mathsf{C}^*{}_i\boldsymbol{R}_{w_i} + \mathsf{C}^*{}_i\Delta\boldsymbol{E}_i \tag{5-42}$$

Substitution of Equations (5-41) and (5-42) into (5-40) yields:

$$\sum_i \left[\Delta \boldsymbol{B}_i^T \left(\hat{\boldsymbol{S}}_i - \boldsymbol{R}_{\sigma_i}\right) + \boldsymbol{B}_i^T \left(\mathsf{C}^*{}_i \boldsymbol{R}_{w_i} + \mathsf{C}^*{}_i \Delta \boldsymbol{E}_i\right)\right] w_i - \Delta \boldsymbol{f} = \boldsymbol{R}_v \tag{5-43}$$

which after rewriting results in Equation (5-44):

$$\boldsymbol{K}_e \Delta \boldsymbol{v} - \Delta \boldsymbol{f} = \boldsymbol{R}_e \tag{5-44}$$

with:

$$\boldsymbol{K}_e = \sum_i \left(\frac{\partial \boldsymbol{B}_i^T}{\partial \boldsymbol{v}} \hat{\boldsymbol{S}}_i + \boldsymbol{B}_i^T \mathsf{C}^*{}_i \boldsymbol{B}_i\right) w_i \tag{5-45}$$

$$\boldsymbol{R}_e = \boldsymbol{R}_v + \sum_i \left(\cancelto{0}{\frac{\partial \boldsymbol{B}_i^T}{\partial \boldsymbol{v}} \boldsymbol{R}_{\sigma_i} \Delta \boldsymbol{v}} - \boldsymbol{B}_i^T \mathsf{C}^*{}_i \boldsymbol{R}_{w_i}\right) w_i \tag{5-46}$$

$\boldsymbol{K}_e$ represents the local element stiffness matrix and $\boldsymbol{R}_e$ the effective residue vector. Note that in this $\boldsymbol{R}_e$ the term containing $\boldsymbol{R}_\sigma \Delta \boldsymbol{v}$ is neglected because it is second order small. Equations (5-45) and (5-46) contains zeroth, first, second, third and fourth order tensors which need to be converted to matrix notations to be implemented. This is achieved using the Voigt notation of stresses and strains as presented in Section 5-5-1.

In a finite element model of the membrane Equations (5-45) and (5-46) are applied to every element, and the results assembled into a global stiffness matrix, force vector and residual vector. Based on these entities the global displacement vector is determined equivalent to Equation (5-44). Subsequently, $\hat{\boldsymbol{E}}$ and $\hat{\boldsymbol{S}}$ are updated in all integration points using Equations (5-36) and (5-38) respectively. The convexity properties of the equations guarantee that applying these updates in an iterative procedure leads to the membrane configuration carrying the least amount of potential energy whilst satisfying the membrane constraints $\hat{\boldsymbol{S}} > \boldsymbol{0}$ and $\hat{\boldsymbol{E}} > \boldsymbol{0}$. These convexity properties allows efficient numerical solvers to be applied, which ensures the efficiency of the proposed method.

Note that the form of Equation (5-44) is standard in commercial finite element method (FEM) packages, which means that the proposed method is suitable to be implemented in such a software package. The form of Equation (5-44) also allows the proposed membrane element to be coupled with any other available type of finite elements such as a shell or solid element.

5-6 Hu-Washizu Principle

The potential energy function in the membrane, which represents the weak form of the balance of momentum, was formulated in Section 5-4. In the potential energy formulation the stress-strain and strain-displacement relations are implemented directly. A weaker form of representing the governing equations is obtained by applying the weak formulation also to these stress-strain and strain-displacement relations, which results in the Hu-Washizu principle [39].

The Hu-Washizu principle was used in quadrilateral finite elements as described in Chapter 8. These elements have a tendency to behave too stiffly which can partly be solved by

applying this principle.

Suppose $\breve{\boldsymbol{S}}$ is the assumed stress in the membrane, $\breve{\boldsymbol{E}}$ is the assumed total strain and $\boldsymbol{u}$ is the displacement field. These three variables should obey the balance of momentum, stress-strain relation and strain-displacement relation, which are written in Equation (5-47) respectively:

$$\nabla \cdot \boldsymbol{F}\breve{\boldsymbol{S}} + \boldsymbol{b} = \boldsymbol{0} \tag{5-47a}$$

$$\breve{\boldsymbol{S}} - \boldsymbol{S}(\breve{\boldsymbol{E}} + \hat{\boldsymbol{E}}) = \boldsymbol{0} \tag{5-47b}$$

$$\breve{\boldsymbol{E}} - \boldsymbol{E}(\boldsymbol{u}) = \boldsymbol{0} \tag{5-47c}$$

in which $\boldsymbol{b}$ is the body force and $\boldsymbol{F}$ the deformation gradient. Note that the wrinkling strain $\hat{\boldsymbol{E}}$ is not a variable in this formulation since it is determined by the relaxed strain energy function in Equation (5-15) already.

The three governing equations are written in the weak form by multiplying them with a test function and integrating over the domain of the membrane. The test function is a variation function such that its multiplication with the governing equation is a scalar with the unit of energy. Accordingly, Equation (5-47a) is multiplied by $\delta\boldsymbol{u}$, which for the first term gives:

$$\begin{aligned}\left(\nabla \cdot \boldsymbol{F}\breve{\boldsymbol{S}}\right) \cdot \delta\boldsymbol{u} &= \nabla \cdot \left(\boldsymbol{F}\breve{\boldsymbol{S}} \cdot \delta\boldsymbol{u}\right) - \boldsymbol{F}\breve{\boldsymbol{S}} : \nabla\delta\boldsymbol{u} \\ &= \nabla \cdot \left(\boldsymbol{F}\breve{\boldsymbol{S}} \cdot \delta\boldsymbol{u}\right) - \breve{\boldsymbol{S}} : \delta\boldsymbol{E}\end{aligned} \tag{5-48}$$

Using this result and performing the integration gives the weak form as shown in Equation (5-49):

$$\int_\Omega \breve{\boldsymbol{S}} : \delta\boldsymbol{E} d\Omega - \int_\Omega \boldsymbol{b} \cdot \delta\boldsymbol{u} d\Omega - \int_{\partial\Omega} \boldsymbol{t} \cdot \delta\boldsymbol{u} d\partial\Omega = 0 \tag{5-49}$$

in which $\boldsymbol{t} = \boldsymbol{F}\breve{\boldsymbol{S}} \cdot \boldsymbol{n}$ is the traction and $\boldsymbol{n}$ the outward normal unit vector to the domain. In the same way Equations (5-47b) and (5-47c) are written in weak form to give:

$$\int_\Omega \delta\breve{\boldsymbol{E}} : \left(\breve{\boldsymbol{S}} - \boldsymbol{S}\right) d\Omega = 0 \tag{5-50}$$

$$\int_\Omega \delta\breve{\boldsymbol{S}} : \left(\breve{\boldsymbol{E}} - \boldsymbol{E}\right) d\Omega = 0 \tag{5-51}$$

Adding Equations (5-49), (5-50) and (5-51) gives after rewriting:

$$\int_\Omega \boldsymbol{S} : \delta\breve{\boldsymbol{E}} d\Omega + \delta \int_\Omega \breve{\boldsymbol{S}} : \left(\boldsymbol{E} - \breve{\boldsymbol{E}}\right) d\Omega + \delta V(\boldsymbol{u}) = 0 \tag{5-52}$$

in which $V(\boldsymbol{u})$ is the potential of the external forces. Note that the term in the first integral is the variation of the relaxed strain energy function. The Hu-Washizu principle is obtained by rewriting Equation (5-52):

$$\delta \left[\int_\Omega \phi^\sharp(\breve{\boldsymbol{E}}) + \breve{\boldsymbol{S}} : \left(\boldsymbol{E} - \breve{\boldsymbol{E}}\right) d\Omega + V(\boldsymbol{u}) \right] = 0 \tag{5-53}$$

Taking variations of this principle with respect to the variables $\breve{\boldsymbol{S}}$, $\breve{\boldsymbol{E}}$ and $\boldsymbol{u}$ returns the weak forms of the governing equations. Writing the stresses and strains in Voigt form this yields Equations (5-54):

$$\int_{\Omega} \delta\breve{\boldsymbol{\sigma}} \cdot (\boldsymbol{\varepsilon} - \breve{\boldsymbol{\varepsilon}})\, d\Omega = 0 \tag{5-54a}$$

$$\int_{\Omega} \delta\breve{\boldsymbol{\varepsilon}} \cdot (\boldsymbol{\sigma} - \breve{\boldsymbol{\sigma}})\, d\Omega = 0 \tag{5-54b}$$

$$\int_{\Omega} \left(\frac{\partial \boldsymbol{\varepsilon}}{\partial \boldsymbol{u}}\right)^{T} \breve{\boldsymbol{\sigma}} d\Omega = \boldsymbol{f} \tag{5-54c}$$

5-7 Constitutive Laws

The strain energy function $\phi(\boldsymbol{E})$ was presented in previous sections as a known function. This function, also known as the constitutive of material law, is presented in this section for two different material models.

The first constitutive law to be considered is widely known as the linear elastic or the Saint-Venant material law. It relates the engineering stresses to the strains as:

$$\boldsymbol{\sigma} = \boldsymbol{C}\boldsymbol{\varepsilon} \qquad \Rightarrow \qquad \begin{pmatrix} \sigma_x \\ \sigma_y \\ \tau_{xy} \end{pmatrix} = \frac{E}{1-\nu^2} \begin{bmatrix} 1 & \nu & 0 \\ \nu & 1 & 0 \\ 0 & 0 & \frac{1-\nu^2}{2} \end{bmatrix} \begin{pmatrix} \varepsilon_x \\ \varepsilon_y \\ \gamma_{xy} \end{pmatrix} \tag{5-55}$$

in which E is the Young's modulus and ν the Poisson's ratio of the material. The strain energy function is then obtained by integrating the stresses over the strains:

$$\phi(\boldsymbol{\varepsilon}) = \int \boldsymbol{\sigma} d\boldsymbol{\varepsilon} = \frac{1}{2}\boldsymbol{\sigma}^{T}\boldsymbol{\varepsilon} = \frac{E}{2(1-\nu^2)} \left[\varepsilon_x^2 + 2\nu\varepsilon_x\varepsilon_y + \varepsilon_y^2 + \frac{1}{4}(1-\nu)^2 \gamma_{xy}^2\right] \tag{5-56}$$

Note that this expression defines the strain energy per unit of volume. The Saint-Venant material law has been applied for several numerical examples described in Chapter 10, however the incompressible neo-Hookean material law was applied in most cases. This material law represents a rubber-like material behavior which is also applicable to membranes. In order to formulate the strain energy function the principal stretches in the membrane are required, for which the right Cauchy-Green deformation tensor $\boldsymbol{C}_C$ is defined as:

$$\boldsymbol{C}_C = \boldsymbol{F}^{T}\boldsymbol{F} = 2\boldsymbol{E} + \boldsymbol{I} \tag{5-57}$$

in which $\boldsymbol{F}$ and $\boldsymbol{E}$ are the deformation gradient and Green-Lagrange strain tensor as defined in Equation (4-11). The principal stretches in the membrane are obtained by computing the eigenvalues of $\boldsymbol{C}_C$, which yields the the in-plane principal stretches λ_1 and λ_2. The third principal stretch λ_3 is obtained by the incompressibility condition:

$$\lambda_3 = \frac{1}{\lambda_1\lambda_2} \tag{5-58}$$

The strain energy function for the incompressible neo-Hookean constitutive law is then defined as [3]:

$$\phi(\boldsymbol{\varepsilon}) = \frac{E}{6}\left(\lambda_1^2 + \lambda_2^2 + \lambda_3^2 - 3\right) \tag{5-59}$$

in which a Poisson's ratio of $\nu = 0.5$ is assumed. Figure 5-3 shows the stress-strain curves and strain energy functions of both the Saint-Venant and neo-Hookean material law. From Figure 5-3b it is observed that both strain energy functions are convex as assumed in the derivation of the relaxed strain energy function of the membrane.

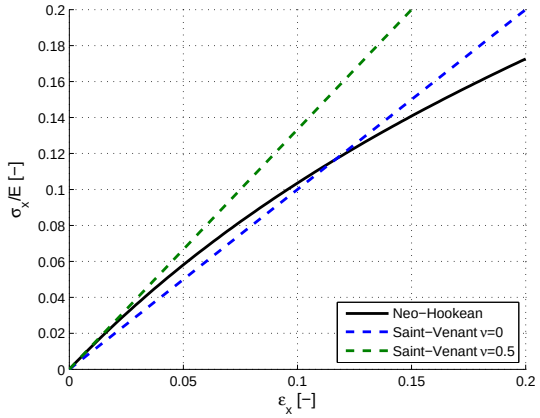

(a) Stress-strain curves; $\varepsilon_y = \gamma_{xy} = 0$.

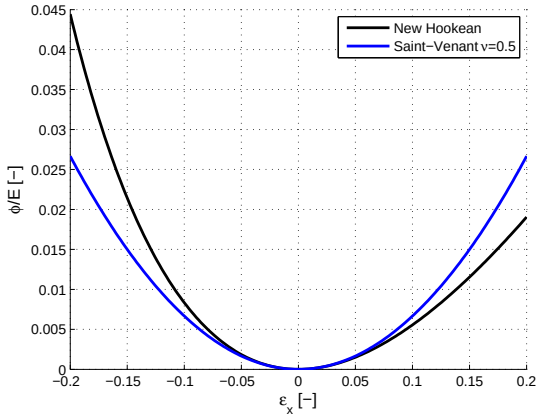

(b) Strain-energy functions; $\varepsilon_y = \gamma_{xy} = 0$.

Figure 5-3: Saint-Venant and neo-Hookean material laws.

Chapter 6

Numerical Implementation

To verify and validate the governing equations describing the configuration of the membrane, they need to be implemented into a numerical algorithm, which is considered in this chapter. An efficient numerical method to implement the governing equations is discussed in Section 6-1, whereas the complete numerical algorithm to model the deformed membrane configuration is presented in Section 6-2.

6-1 Semidefinite Programming Algorithm

An efficient numerical procedure is required to implement the results from Chapter 5, this is discussed in this section. This includes the updates of $\hat{\boldsymbol{E}}$ and $\hat{\boldsymbol{S}}$ and the reduction of the penalty parameter μ to go to zero. The semidefinite programming algorithm (SPDA) described by Fujiwasa et al. [9] and Yamashita et al. [41] is used as a reference.

The updates for wrinkling strains $\Delta\hat{\boldsymbol{E}}$ and stresses $\Delta\hat{\boldsymbol{S}}$ were expressed in Section 5-5. Adding these updates to $\hat{\boldsymbol{E}}$ and $\hat{\boldsymbol{S}}$ directly may result in wrinkling strains and stresses which are not semi-positive definite as required. To prevent this step sizes are introduced for both $\hat{\boldsymbol{E}}$ and $\hat{\boldsymbol{S}}$, which are denoted by α_ε and α_σ respectively. Equation (6-1) shows α_ε is chosen to maintain a semi-positive definite matrix after updating.

$$\hat{\boldsymbol{E}} + \alpha_\varepsilon \Delta\hat{\boldsymbol{E}} \geq \mathbf{0}, \qquad \text{with } 0 \leq \alpha_\varepsilon \leq 1 \tag{6-1}$$

Note that α_ε is not allowed to exceed 1 to prevent overrelaxation of the updates as calculated in Section 5-5. To compute the value of α_ε one could replace the inequality in Equation (6-1) by an equality sign and solve it. This would lead to $\hat{\boldsymbol{E}} = \mathbf{0}$ for the next iteration meaning that this tensor in not invertible any more. For this reason a safety margin κ is introduced resulting in Equation (6-2) to solve:

$$\kappa\hat{\boldsymbol{E}} + \alpha^*_\varepsilon \Delta\hat{\boldsymbol{E}} = \mathbf{0}, \qquad \text{with } 0 < \kappa < 1 \tag{6-2}$$

As can be seen $\kappa = 1$ returns Equation (6-1). From heuristics it is found that $\kappa \approx 0.9$ leads to best convergence of the penalty parameter. To solve Equation (6-2) for α^*_ε it is rewritten

as:

$$-\frac{1}{\kappa}\hat{\boldsymbol{E}}^{-1}\Delta\hat{\boldsymbol{E}}-\frac{1}{\alpha_\varepsilon^*}\boldsymbol{I}=\boldsymbol{0} \tag{6-3}$$

which is an eigenvalue problem, meaning that α_ε^* can be expressed as shown in Equation (6-4):

$$\frac{1}{\alpha_\varepsilon^*}=\mathrm{eig}_{max}\left(-\frac{1}{\kappa}\hat{\boldsymbol{E}}^{-1}\Delta\hat{\boldsymbol{E}}\right)=\frac{1}{\kappa}\mathrm{eig}_{max}\left(-\hat{\boldsymbol{E}}^{-1}\Delta\hat{\boldsymbol{E}}\right) \tag{6-4}$$

in which the operator eig_{max} computes the maximum eigenvalue. This eigenvalue is most critical as it determines the minimum allowed step size. As mentioned before the value of α_ε should not exceed 1, meaning:

$$\frac{1}{\alpha_\varepsilon}=\max\left\{1,\frac{1}{\alpha_\varepsilon^*}\right\}\qquad\Rightarrow\qquad\alpha_\varepsilon=\begin{cases}\alpha_\varepsilon^* & \text{if } 0<\alpha_\varepsilon^*<1\\ 1 & \text{otherwise}\end{cases} \tag{6-5}$$

The step size α_σ for the stresses is calculated in the same way using the matrices $\hat{\boldsymbol{S}}$ and $\Delta\hat{\boldsymbol{S}}$. With these step sizes the wrinkling strain and stress update can be performed directly, however, better convergence is obtained by a predictor-corrector method introduced by Mehrotra [17]. This method also describes an efficient algorithm to let the penalty parameter μ approach zero.

Suppose that for iteration $k-1$ the wrinkling strains and stresses are known. From Equation (5-33) the penalty parameter for this iteration is calculated to be:

$$\mu_{k-1}=\frac{1}{2}\hat{\boldsymbol{E}}:\hat{\boldsymbol{S}}=\frac{1}{2}\mathrm{tr}\hat{\boldsymbol{E}}\hat{\boldsymbol{S}} \tag{6-6}$$

For iteration k this penalty parameter is decreased by a user defined 'centering parameter' β_1, such that $\mu_k^{pred}=\beta_1\mu_{k-1}$. From heuristics good values for this parameter are $\beta_1=0$ if the solution is already feasible ($\boldsymbol{S}>0$ and $\boldsymbol{E}>0$) and $\beta_1=0.2$ otherwise [41]. In Section 6-2 it has been explained that in the iterative solution algorithm the variables are initialized in the feasible region, which means that $\beta_1=0$ is applied in the implementation.

Using μ_k^{pred} the residues in Section 5-5 can be calculated and the updates $\Delta\hat{\boldsymbol{E}}^{pred}$ and $\Delta\hat{\boldsymbol{S}}^{pred}$ are found from Equations (5-36) and (5-38) respectively. The step sizes α_ε and α_σ then follow from these results.

Next the corrector step for this iteration is entered. This is done by computing the updated centering parameter β_{aux} as defined by Mehrotra [17]:

$$\beta_{aux}=\left(\frac{\left(\hat{\boldsymbol{S}}+\alpha_\sigma\Delta\hat{\boldsymbol{S}}^{pred}\right):\left(\hat{\boldsymbol{E}}+\alpha_\varepsilon\Delta\hat{\boldsymbol{E}}^{pred}\right)}{\hat{\boldsymbol{S}}:\hat{\boldsymbol{E}}}\right)^2 \tag{6-7}$$

To prevent this parameter to cause instabilities by becoming too small, the applied updated centering parameter is β_c as defined in Equation (6-8):

$$\beta_c=\max\left\{\beta_{aux},\beta_2\right\} \tag{6-8}$$

in which β_2 again is a user defined parameter which turns out to perform best when $\beta_2=0.1$ if the solution is already feasible and $\beta_2=0.2$ otherwise. The corrected penalty parameter

for iteration k is then given as $\mu_k^{corr} = \beta_c \mu_{k-1}$. This parameter as well as $\Delta\hat{\boldsymbol{E}}^{pred}$ and $\Delta\hat{\boldsymbol{S}}^{pred}$ are needed to compute the residuals described in Section 5-5-2 for this iteration.

Solving Equations (5-36) and (5-38) again gives the wrinkling strains and stress updates for this iteration. By computing the corresponding step sizes, $\hat{\boldsymbol{E}}$ and $\hat{\boldsymbol{S}}$ are updated and iteration $k+1$ is entered.

6-2 Numerical Algorithm

The complete numerical procedure to find the equilibrium state of a membrane structure under a given applied loading or displacement is presented in this section. First it should be noted that the numerical procedure discussed in Section 6-1 is performed on integration point level within a finite element model. In a full model this procedure applies to each integration point, except for the computation of the penalty parameter in Equation (6-6) as μ is defined on global level rather than at integration point level. Suppose the membrane model consists of n_e finite elements and n_g integration points per element, then the global penalty parameter is computed as:

$$\mu = \frac{\frac{1}{2}\sum_{j=1}^{n_e}\sum_{i=1}^{n_g} A_j w_i \hat{\boldsymbol{E}}_i : \hat{\boldsymbol{S}}_i}{\sum_{j=1}^{n_e}\sum_{i=1}^{n_g} A_j w_i} \tag{6-9}$$

In the finite element model the load is applied in several steps which all consist of iterations to reach convergence of the results. For step j and iteration k the numerical procedure is presented in Algorithm 1. The procedure in this algorithms is complete, except for the first iteration in each step. As is the case in any Newton-iteration method an initialization must be specified to start the optimization. For the membrane this means that the wrinkling strains $\hat{\boldsymbol{E}}$ and $\hat{\boldsymbol{S}}$ have to be initialized in each integration point. Theoretically the choice of initialization is arbitrary given that $\hat{\boldsymbol{S}} > \boldsymbol{0}$ and $\hat{\boldsymbol{E}} > \boldsymbol{0}$, however, in order to obtain an efficient and numerically robust method the initialization is based on the total strain $\boldsymbol{E}$. Algorithm 2 shows the modifications in the pseudo-code for the first iteration of a step. The initialization of wrinkling strains and stresses is performed on integration point level and is based on the total strain $\boldsymbol{E}$. Let $\hat{\boldsymbol{S}}_0$ be the stress tensor computed from the strain energy function of the material without any wrinkling effects:

$$\hat{\boldsymbol{S}}_0 = \left.\frac{\partial \phi}{\partial \boldsymbol{E}}\right|_{\boldsymbol{E}} \tag{6-10}$$

which can be negative depending on the total strain. Note that $\hat{\boldsymbol{S}}_0$ represents the stress tensor computed as if the membrane is a regular shell structure. The initialization of the stress $\boldsymbol{S}$ is computed by shifting $\hat{\boldsymbol{S}}_0$ towards the positive regime:

$$\hat{\boldsymbol{S}} = \hat{\boldsymbol{S}}_0 + p\boldsymbol{I} \tag{6-11}$$

The value of p needs to be larger than the most negative eigenvalue of $\hat{\boldsymbol{S}}_0$ to get $\hat{\boldsymbol{S}} > \boldsymbol{0}$. Mathematically any value of p fulfilling this requirement is sufficient for the optimization procedure to converge. However taking numerical instability and numerical cost into account

Algorithm 1 Pseudo-code of numerical implementation.

Step j **, iteration** k

1. **Compute** $\boldsymbol{K}_e$ and $\boldsymbol{R}_e$ from (5-45) and (5-46) for each finite element using results from iteration $k-1$.
2. **Assemble** global stiffness matrix $\boldsymbol{K}_k$ and residual force vector $\boldsymbol{R}_k$.
3. **Obtain** applied force $\Delta \boldsymbol{f}$ which is non-zero if and only if $k = 1$.
4. **Predictor** step:
   - 4.1. **Compute** predictor displacement increment $\Delta \boldsymbol{v}_k^{pred} = \boldsymbol{K}_k^{-1} (\Delta \boldsymbol{f} + \boldsymbol{R}_k)$ and displacement vector $\boldsymbol{v}_k^{pred} = \boldsymbol{v}_{k-1} + \Delta \boldsymbol{v}_k^{pred}$.
   - 4.2. **Compute** in each integration point i the total strain $\boldsymbol{E}_{i,k}^{pred}$ from $\boldsymbol{v}_k^{pred}$, and $\Delta \boldsymbol{E}_{i,k}^{pred} = \boldsymbol{E}_{i,k}^{pred} - \boldsymbol{E}_{i,k-1}^{pred}$.
   - 4.3. Only if ($k = 1$ & $j = 1$), see Algorithm 2.
   - 4.4. **Reduce** penalty parameter $\mu_k^{pred} = \beta_1 \mu_{k-1}$.
   - 4.5. **Compute** residuals $\boldsymbol{R}_{\mu,i}^{pred}$ and $\boldsymbol{R}_{w,i}^{pred}$ at each integration point i based on μ_k^{pred}, and predict wrinkling updates $\Delta \hat{\boldsymbol{E}}_{i,k}^{pred}$ and $\Delta \hat{\boldsymbol{S}}_{i,k}^{pred}$ from (5-36) and (5-38).
   - 4.6. **Update** step sizes: $\Delta \hat{\boldsymbol{E}}_{i,k}^{pred} \leftarrow \alpha_\varepsilon \Delta \hat{\boldsymbol{E}}_{i,k}^{pred}$ and $\Delta \hat{\boldsymbol{S}}_{i,k}^{pred} \leftarrow \alpha_\sigma \Delta \hat{\boldsymbol{S}}_{i,k}^{pred}$.
   - 4.7. **Update** predictor wrinkling strains: $\hat{\boldsymbol{E}}_{i,k}^{pred} = \hat{\boldsymbol{E}}_{i,k-1} + \Delta \hat{\boldsymbol{E}}_{i,k}^{pred}$ and stresses: $\hat{\boldsymbol{S}}_{i,k}^{pred} = \hat{\boldsymbol{S}}_{i,k-1} + \Delta \hat{\boldsymbol{S}}_{i,k}^{pred}$.
5. **Corrector** step:
   - 5.1. **Update** $\boldsymbol{R}_k$ based on $\Delta \hat{\boldsymbol{E}}_{i,k}^{pred}$ and $\Delta \hat{\boldsymbol{S}}_{i,k}^{pred}$.
   - 5.2. **Compute** corrector displacement increment $\Delta \boldsymbol{v}_k$ and consequently $\boldsymbol{v}_k$.
   - 5.3. **Compute** total strain and strain increment in each integration point i: $\boldsymbol{E}_{i,k}$ and $\Delta \boldsymbol{E}_{i,k}$.
   - 5.4. **Reduce** penalty parameter $\mu_k^{corr} = \beta_c \mu_{k-1}$.
   - 5.5. **Compute**, based on μ_k^{corr}, the corrector wrinkling updates $\Delta \hat{\boldsymbol{E}}_{i,k}$ and $\Delta \hat{\boldsymbol{S}}_{i,k}$.
   - 5.6. **Update** step sizes: $\Delta \hat{\boldsymbol{E}}_{i,k} \leftarrow \alpha_\varepsilon \Delta \hat{\boldsymbol{E}}_{i,k}$ and $\Delta \hat{\boldsymbol{S}}_{i,k} \leftarrow \alpha_\sigma \Delta \hat{\boldsymbol{S}}_{i,k}$.
   - 5.7. **Update** wrinkling strains: $\hat{\boldsymbol{E}}_{i,k} = \hat{\boldsymbol{E}}_{i,k-1} + \Delta \hat{\boldsymbol{E}}_{i,k}$ and stresses: $\hat{\boldsymbol{S}}_{i,k} = \hat{\boldsymbol{S}}_{i,k-1} + \Delta \hat{\boldsymbol{S}}_{i,k}^{pred}$.
6. **Compute** internal force vector $\boldsymbol{f}_{int,k}$.
7. **Compute** penalty parameter μ_k as in (6-9).
8. **Check** convergence criteria on μ and strain energy ϕ as: $\mu_k < \epsilon_\mu = 10^{-6}$ and $\|\Delta \phi_k / \Delta \phi_1\| < \epsilon_\phi = 10^{-4}$.
9. **Proceed** to next iteration if not converged, proceed to next step/finish if converged.

end

Algorithm 2 Modifications in numerical implementation for first iteration.

if $k = 1$ and $j = 1$ **then** ▷ *First iteration in first step*

1. **Compute** $\boldsymbol{K}_e$ and $\boldsymbol{R}_e$ from (5-45) and (5-46) assuming for each integration point $\hat{\boldsymbol{S}}_{i,k-1} = \hat{\boldsymbol{E}}_{i,k-1} = \boldsymbol{0}$ and $\boldsymbol{R}_{w_i} = \boldsymbol{0}$.

4. **Predictor** step:

   4.3.1. **Initialize** $\hat{\boldsymbol{S}}_{i,k-1}$, $\hat{\boldsymbol{E}}_{i,k-1}$ in each integration point i based on $\boldsymbol{E}_i$ as computed in item 4.2. in Algorithm 1.

   4.3.2. **Initialize** μ_{k-1} from (6-9).

else if $k = 1$ **then** ▷ *First iteration in any other step*

0. **Initialization**:

   0.1. **Initialize** $\hat{\boldsymbol{S}}_{i,k-1}$, $\hat{\boldsymbol{E}}_{i,k-1}$ in each integration point i from converged $\boldsymbol{E}_i$ at the previous step $j-1$.

   0.2. **Initialize** μ_{k-1} from (6-9).

end if

one should choose p more carefully. Equation (6-12) shows the expression for p which has been used:

$$p = \max\{0, -\lambda_1 - k_p(\lambda_1 - \lambda_2)\} \tag{6-12}$$

in which λ_1 and λ_2 are the eigenvalues, i.e. principal stresses, of $\hat{\boldsymbol{S}}_0$ with $\lambda_1 \leq \lambda_2$. This expression for p states that if $\hat{\boldsymbol{S}}_0$ is positive it is directly applied as stress initialization of the membrane. Otherwise, if $\hat{\boldsymbol{S}}_0$ is not positive, the value of p is chosen such that $\hat{\boldsymbol{S}}_0 + p\boldsymbol{I}$ is positive which is then used as stress initialization. The value of k_p in the expression for p indicates the extent to which $\hat{\boldsymbol{S}}$ is made positive. From heuristics it has been found that $k_p \approx 3$ results in good convergence of the solution.

Note that choosing a different expression for p instead of Equation (6-12) is valid as long as it results in $\hat{\boldsymbol{S}} > \boldsymbol{0}$. The current expression was applied as it was shown to perform best up to total strains of at least 10%.

From this initialization of $\hat{\boldsymbol{S}}$ the wrinkling strain in the integration point can be found by applying $\hat{\boldsymbol{E}} = \mu\hat{\boldsymbol{S}}^{-1}$, however, the value for μ has not yet been defined in this first iteration and therefore it needs to be initialized. Any strictly positive value for $\mu = \mu_0$ leads to convergence from a mathematical point of view. From a numerical point of view it is proposed that choosing the μ_0 proportional to the strain energy of the computed strain prevents numerical instability:

$$\mu_0 = k_\mu \phi(\boldsymbol{E}) \tag{6-13}$$

in which $\phi(\boldsymbol{E})$ is the familiar strain energy function. The optimal value of k_μ has been found heuristically to be $k_\mu \approx 1$ for the choice of β_1 and β_2 of the Mehrotra update presented in Section 6-1. Note that only for this initialization procedure each integration point has its own μ_0 whereas in the computational procedure described in Algorithm 1 there is a single penalty parameter for the whole structure as presented in Equation (6-9).

Chapter 7

Triangular Elements

To model the deformed configuration and tension field of a membrane under applied loading, the membrane structure was discretized into finite elements as presented in Section 5-5. The displacement field over such an element was approximated using shape functions which were introduced in Section 5-5-1 in general. The next three chapters are devoted to presenting different shape functions depending on the type of finite elements applied.

The triangular finite element is presented in this chapter. In general the reference configuration of the membrane cannot be represented by triangles exactly, meaning that the triangular element is isoparametric. The two-dimensional element is introduced in Section 7-1 which is extended to three dimensions in Section 7-2.

7-1 2D Elements

The shape functions $\boldsymbol{N}$ for a two-dimensional triangular, T2, element are presented in this section. These shape functions have been introduced in Section 5-5-1 and depend on the coordinates $\boldsymbol{\xi}$ in the reference coordinate system. This will be chosen to be the Cartesian system with x, y coordinates:

$$\boldsymbol{\xi} = [x, y]^T \tag{7-1}$$

Figure 7-1 shows a sketch of a T2 element with u_i and v_i denoting the nodal displacements in x and y directions respectively.

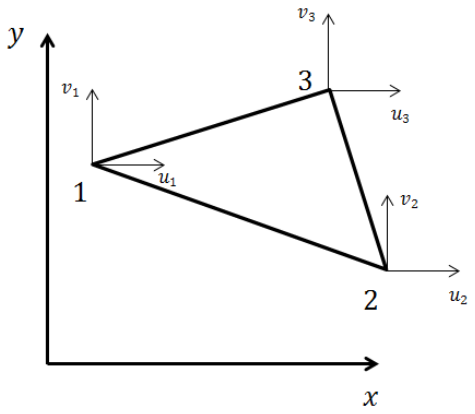

Figure 7-1: 2D triangular finite element in $\mathbb{R}^2$.

A shape function N_i has value 1 at node i and 0 at the other nodes, which results in the three shape functions as shown in Equation (7-2):

$$\begin{aligned} N_1(\boldsymbol{\xi}) &= \frac{1}{2A}\left[x_2y_3 - x_3y_2 + (y_2 - y_3)\,x + (x_3 - x_2)\,y\right] \\ N_2(\boldsymbol{\xi}) &= \frac{1}{2A}\left[x_3y_1 - x_1y_3 + (y_3 - y_1)\,x + (x_1 - x_3)\,y\right] \\ N_3(\boldsymbol{\xi}) &= \frac{1}{2A}\left[x_1y_2 - x_2y_1 + (y_1 - y_2)\,x + (x_2 - x_1)\,y\right] \end{aligned} \tag{7-2}$$

in which A is the area of the element. With these shape functions the shape function matrix $\boldsymbol{N}$ is constructed to be:

$$\boldsymbol{N}(\boldsymbol{\xi}) = \begin{bmatrix} N_1 & 0 & N_2 & 0 & N_3 & 0 \\ 0 & N_1 & 0 & N_2 & 0 & N_3 \end{bmatrix} \tag{7-3}$$

such that Equations (5-25) and (5-26) become:

$$\begin{pmatrix} x_0 \\ y_0 \end{pmatrix} = \boldsymbol{N}(\boldsymbol{\xi}) \begin{pmatrix} x_{1,0} \\ y_{1,0} \\ x_{2,0} \\ y_{2,0} \\ x_{3,0} \\ y_{3,0} \end{pmatrix}; \qquad \begin{pmatrix} u \\ v \end{pmatrix} = \boldsymbol{N}(\boldsymbol{\xi}) \begin{pmatrix} u_1 \\ v_1 \\ u_2 \\ v_2 \\ u_3 \\ v_3 \end{pmatrix} \tag{7-4}$$

By applying Section 5-5-1 these shape functions are used to compute the strain-displacement relation, i.e. the $\boldsymbol{B}$ matrix. The expressions for some of the matrices for this triangular element are shown in Appendix B.

It should be noted that these matrices are independent of the x, y coordinates and are therefore constant over the element. Integration over the element is therefore equivalent to multiplying the matrices by the volume of the element, which means that a single integration point in the element is sufficient.

Applying this to Equations (5-45) and (5-46), the element stiffness matrix and residual

force vector can be written as shown in Equation (7-5):

$$\boldsymbol{K}_e = tA\left(\frac{\partial \boldsymbol{B}^T}{\partial \boldsymbol{v}}\hat{\boldsymbol{S}} + \boldsymbol{B}^T\boldsymbol{C}^*\boldsymbol{B}\right) \tag{7-5a}$$

$$\boldsymbol{R}_e = \boldsymbol{R}_v - tA\boldsymbol{B}^T\boldsymbol{C}^*\boldsymbol{R}_w \tag{7-5b}$$

7-2 3D Elements

The triangular membrane element is placed in three dimensional space in this section, which yields the T3 element. The element remains a surface, therefore it can still be represented by the coordinates $\boldsymbol{\xi} = [x, y]^T$ by choosing the basis vectors $\boldsymbol{e}_x$ and $\boldsymbol{e}_y$ tangential to the surface. These x, y-coordinates are used to compute the shape functions over the T3 element in the exact same way as for the T2 element, and because the T3 element exists in $\mathbb{R}^3$, its position is described in a Cartesian reference system using the coordinates $\boldsymbol{\Xi} = [X, Y, Z]^T$. Note that in this section capital letters represent entities in $\mathbb{R}^3$. Figure 7-2 shows the triangular element in three dimensional space.

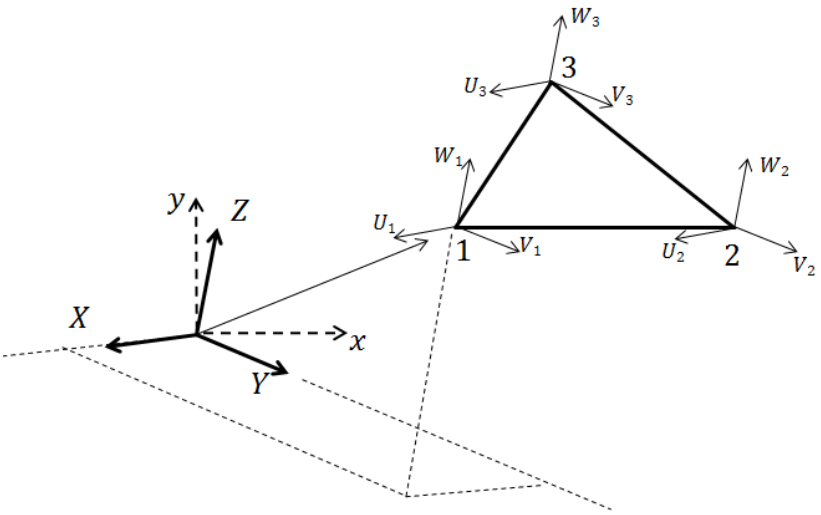

Figure 7-2: 3D triangular finite element in $\mathbb{R}^3$.

The T3 element in Figure 7-2 is arbitrarily oriented in $\mathbb{R}^3$, whereas the x, y coordinate system is parallel to the element with its origin at the origin of the (X, Y, Z) system. The x-axis is chosen to be parallel to the vector from node 1 to node 2. The displacement at the nodes is represented by its (U, V, W) components.

When applying the T3 element in a numerical model, its coordinates $\boldsymbol{\Xi}$ are specified by the user and thus known. To compute the $\boldsymbol{\xi}$ coordinates a transformation is required based on Figure 7-2. For this, first the normalized basis vectors $\boldsymbol{e}_x$ and $\boldsymbol{e}_y$ are computed as shown in

Equations (7-6) and (7-7):

$$\boldsymbol{e}_x = \frac{\boldsymbol{r}_{12}}{\|\boldsymbol{r}_{12}\|} \tag{7-6}$$

$$\boldsymbol{e}_y = \frac{\boldsymbol{r}_{13} - (\boldsymbol{r}_{13} \cdot \boldsymbol{e}_x)\, \boldsymbol{e}_x}{\|\boldsymbol{r}_{13} - (\boldsymbol{r}_{13} \cdot \boldsymbol{e}_x)\, \boldsymbol{e}_x\|} \tag{7-7}$$

$$\tag{7-8}$$

with:

$$\boldsymbol{r}_{ij} = \boldsymbol{r}_0(\boldsymbol{\Xi})_j - \boldsymbol{r}_0(\boldsymbol{\Xi})_i = \begin{pmatrix} X_{0,j} \\ Y_{0,j} \\ Z_{0,j} \end{pmatrix} - \begin{pmatrix} X_{0,i} \\ Y_{0,i} \\ Z_{0,i} \end{pmatrix} \tag{7-9}$$

For any material point inside the element the $\boldsymbol{\xi}$ coordinates are computed by projecting the $\boldsymbol{\Xi}$ coordinates on the plane spanned by $\boldsymbol{e}_x$ and $\boldsymbol{e}_y$:

$$\boldsymbol{\xi} = \boldsymbol{\Lambda}\boldsymbol{\Xi}; \qquad \boldsymbol{\Lambda} = \begin{bmatrix} \boldsymbol{e}_x^T \\ \boldsymbol{e}_y^T \end{bmatrix} \tag{7-10}$$

Using this transformation the x, y coordinates of any point inside the T3 element, including the nodes, can be computed. These are used to compute the shape functions N_1, N_2 and N_3 as shown in Equation (7-2). The shape function matrix $\boldsymbol{N}$ then becomes as given in (7-11), which differs from the 2D case in the third row which has been added because the T3 element exists in $\mathbb{R}^3$:

$$\boldsymbol{N}(\boldsymbol{\xi}) = \begin{bmatrix} N_1 & 0 & 0 & N_2 & 0 & 0 & N_3 & 0 & 0 \\ 0 & N_1 & 0 & 0 & N_2 & 0 & 0 & N_3 & 0 \\ 0 & 0 & N_1 & 0 & 0 & N_2 & 0 & 0 & N_3 \end{bmatrix} \tag{7-11}$$

Based on this shape function matrix all matrices as shown in Section 5-5-1 are computed using the same process as for the T2 element. By definition the reference position and the displacement of any material point inside the element is computed from the nodal position and nodal displacement vector respectively:

$$\boldsymbol{r}_0 = \boldsymbol{N}(\boldsymbol{\xi})\, \boldsymbol{\rho}_0 \qquad \boldsymbol{u} = \boldsymbol{N}(\boldsymbol{\xi})\, \boldsymbol{v} \tag{7-12}$$

with:

$$\boldsymbol{\rho}_0 = \begin{bmatrix} X_{0,1}, & Y_{0,1}, & Z_{0,1}, & \ldots, & X_{0,3}, & Y_{0,3}, & Z_{0,3} \end{bmatrix}^T$$

$$\boldsymbol{v} = \begin{bmatrix} U_1, & V_1, & W_1, & \ldots, & U_3, & V_3, & W_3 \end{bmatrix}^T$$

Chapter 8

Quadrilateral Elements

Quadrilateral finite elements are slightly more advanced than the triangular elements discussed in the previous chapter. The shape functions over these four-noded elements are bilinear which results in their derivatives being linear over the element. These shape functions are defined in an element coordinate frame instead of the global coordinate frame as was the case for the triangular elements. One of the advantages of the quadrilateral elements is the linear stress distribution over the element in contrast to the constant stress distribution in triangular elements. Note that in general the geometry of a membrane structure cannot be represented by quadrilateral elements exactly, which means this element is isoparametric.

The two-dimensional standard quadrilateral element is presented in Section 8-1. This standard element has a disadvantage of behaving too stiff as a result of membrane locking, which is resolved by the formulation of the hybrid element in Section 8-2. The extension of the quadrilateral finite element to three dimensions is finally presented in Section 8-3.

8-1 2D Elements

The shape functions for a two-dimensional quadrilateral, Q2, element are presented in this section. As with the triangular elements, the global coordinates $\boldsymbol{\xi}$ are in a Cartesian reference frame. To derive the shape functions in this coordinate system an extra set of coordinates $\boldsymbol{\eta}$ is required which is in a non-Cartesian element reference frame in general.

These two coordinate systems have components as shown in Equation (8-1):

$$\boldsymbol{\xi} = [x, y]^T \qquad \boldsymbol{\eta} = [r, s]^T \tag{8-1}$$

Figure 8-1 shows a general Q2 element both in global and element coordinate system.

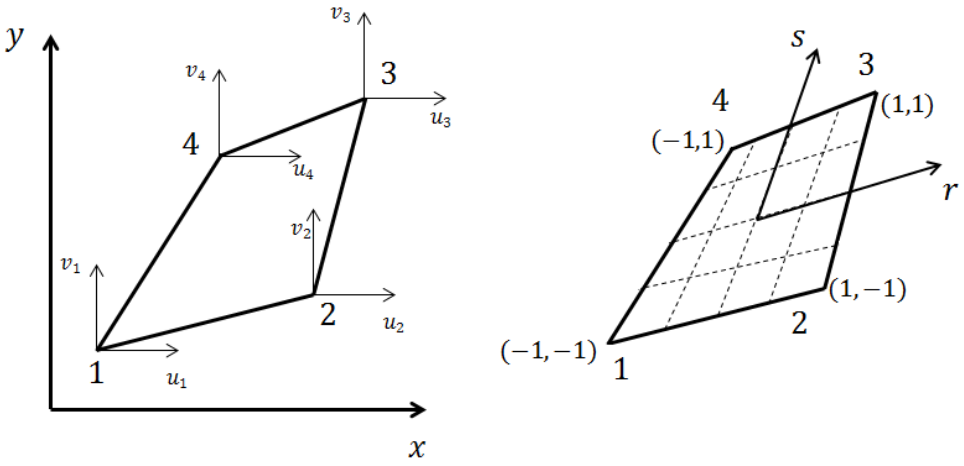

(a) Global coordinate system **(b)** Element coordinates system

Figure 8-1: 2D quadrilateral finite element in different coordinates systems in $\mathbb{R}^3$.

The relation between the differentials $d\boldsymbol{\xi}$ and $d\boldsymbol{\eta}$ is given by the Jacobian $\boldsymbol{J}$ as shown in Equation (8-2):

$$d\boldsymbol{\xi} = \begin{bmatrix} \frac{\partial x}{\partial r} & \frac{\partial x}{\partial s} \\ \frac{\partial y}{\partial r} & \frac{\partial y}{\partial s} \end{bmatrix} d\boldsymbol{\eta} = \boldsymbol{J} d\boldsymbol{\eta} \tag{8-2}$$

The shape functions N_i are presented in the element coordinate system as:

$$\begin{aligned} N_1(\boldsymbol{\eta}) &= \frac{1}{4}(1-r)(1-s) \\ N_2(\boldsymbol{\eta}) &= \frac{1}{4}(1+r)(1-s) \\ N_3(\boldsymbol{\eta}) &= \frac{1}{4}(1+r)(1+s) \\ N_4(\boldsymbol{\eta}) &= \frac{1}{4}(1-r)(1+s) \end{aligned} \tag{8-3}$$

Combining these yields the shape function matrix $\boldsymbol{N}(\boldsymbol{\eta})$:

$$\boldsymbol{N}(\boldsymbol{\eta}) = \begin{bmatrix} N_1 & 0 & N_2 & 0 & N_3 & 0 & N_4 & 0 \\ 0 & N_1 & 0 & N_2 & 0 & N_3 & 0 & N_4 \end{bmatrix} \tag{8-4}$$

To compute the $\boldsymbol{B}$ matrix in Equation (5-29) the derivative of this shape function matrix with respect to the global coordinates ξ_i is required. Applying the chain rule, this derivative can be written to be:

$$\boldsymbol{N}_{,i} = \frac{\partial \boldsymbol{N}}{\partial \xi_i} = \frac{\partial \eta_j}{\partial \xi_i} \frac{\partial \boldsymbol{N}}{\partial \eta_j} = \sum_{j=1}^{2} \left(J^{-1}\right)_{ji} \frac{\partial \boldsymbol{N}}{\partial \eta_j} \tag{8-5}$$

This expression is applied to find the derivative of the shape function with respect to x and y:

$$\frac{\partial \boldsymbol{N}}{\partial x} = \left(J^{-1}\right)_{11} \frac{\partial \boldsymbol{N}}{\partial r} + \left(J^{-1}\right)_{21} \frac{\partial \boldsymbol{N}}{\partial s} = \frac{1}{\det \boldsymbol{J}} \left(J_{22} \frac{\partial \boldsymbol{N}}{\partial r} - J_{21} \frac{\partial \boldsymbol{N}}{\partial s} \right) \tag{8-6a}$$

$$\frac{\partial \boldsymbol{N}}{\partial y} = \left(J^{-1}\right)_{12} \frac{\partial \boldsymbol{N}}{\partial r} + \left(J^{-1}\right)_{22} \frac{\partial \boldsymbol{N}}{\partial s} = \frac{1}{\det \boldsymbol{J}} \left(-J_{12} \frac{\partial \boldsymbol{N}}{\partial r} + J_{11} \frac{\partial \boldsymbol{N}}{\partial s} \right) \tag{8-6b}$$

From these derivatives the $\boldsymbol{B}$ matrix is computed as shown in Section 5-5-1, provided that the components of the Jacobian $\boldsymbol{J}$ are known. To compute these components, the definition of the shape functions is repeated in Equation (8-7):

$$\boldsymbol{r}(\boldsymbol{\xi}) = \boldsymbol{N}\boldsymbol{\rho}_0 \qquad \Rightarrow \qquad \xi_i = N_{ij}\rho_{0,j} \tag{8-7}$$

with $\boldsymbol{\rho}_0$ being the initial location of the nodes in global coordinates:

$$\boldsymbol{\rho}_0 = \begin{bmatrix} x_{0,1} & y_{0,1} & x_{0,2} & y_{0,2} & x_{0,3} & y_{0,3} & x_{0,4} & y_{0,4} \end{bmatrix}^T \tag{8-8}$$

The components of the Jacobian are then computed as:

$$J_{ik} = \frac{\partial \xi_i}{\partial \eta_j} = \frac{\partial N_{ij}}{\partial \eta_k}\xi_{0,j} \tag{8-9}$$

Applying this equation to the J_{11} component gives:

$$J_{11} = \frac{\partial x}{\partial r} = \frac{\partial N_{11}}{\partial r}x_{0,1} + \frac{\partial N_{12}}{\partial r}y_{0,1} + ... + \frac{\partial N_{18}}{\partial r}x_{0,4} \tag{8-10}$$

The $\boldsymbol{B}$ matrix for Q2 elements is not constant over each element but it depends linearly on the element coordinates r, s. Consequently, as specified by the Gauss-integration rules, four integration points at $r, s = \pm 1/\sqrt{3}$ are required for the numerical integration, which all have a weight $w_i = 1$. The determinant of the Jacobian accounts for the change in coordinates from $\boldsymbol{\eta}$ to $\boldsymbol{\xi}$:

$$dxdy = \det\boldsymbol{J} drds$$

The element stiffness matrix and residual force vector are therefore written as shown in Equation (8-11):

$$\boldsymbol{K}_e = t\sum_{i=1}^{4}\left(\frac{\partial \boldsymbol{B}_i^T}{\partial \boldsymbol{v}}\hat{\boldsymbol{S}}_i + \boldsymbol{B}_i^T\boldsymbol{C^*}_i\boldsymbol{B}_i\right)\det\boldsymbol{J}_i \tag{8-11a}$$

$$\boldsymbol{R}_e = \boldsymbol{R}_v - t\sum_{i=1}^{4}\boldsymbol{B}_i^T\boldsymbol{C^*}_i\boldsymbol{R}_{w_i}\det\boldsymbol{J}_i \tag{8-11b}$$

8-2 Hybrid Element

The quadrilateral element as presented in Section 8-1 has a significant disadvantage of behaving too stiff under in plane deformations. This is caused by the four Gauss points used for numerical integration which can model five stress and strain modes: two in-plane stretch, one in-plane shear and two in-plane bending modes.

The bilinear shape functions are only able to represent the first three of these modes, which means that the displacement field does not contain the two bending modes. For a better understanding, consider the quadrilateral element in its element coordinates as shown in Figure 8-2.

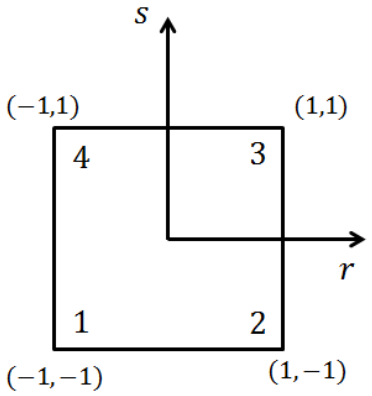

Figure 8-2: Quadrilateral element in its element coordinate system.

The shape functions as presented in Equation (8-3) are linear on the edges of this element, whereas the stress and strain bending modes would curve the edges. This means that the system has to provide energy to keep the edges straight, resulting in too high stiffness of the elements.

This effect was reduced by the design of a hybrid element. In this element the bending modes of stress and strain are projected on the other three modes, which removes the bending modes and therefore makes the stress and strain modes compatible with the shape functions. A general formulation of hybrid elements is given by Pian [22], whereas Sansour [31] performs an assessment of several of these elements. For the design of the hybrid element the Hu-Washizu principle as presented in Section 5-6 was applied.

8-2-1 Consistent Hybrid Element

The Hu-Washizu principle includes an assumed stress and strain field as shown in Section 5-6. The assumed strain field $\breve{\boldsymbol{\varepsilon}}$ is the projection of all five strain modes onto the stretch and shear modes, which is shown in Equation (8-12):

$$\breve{\boldsymbol{\varepsilon}} = \boldsymbol{T}\left(\bar{\boldsymbol{\varepsilon}} + \begin{bmatrix} k_r s \\ k_s r \\ 0 \end{bmatrix}\right) = \boldsymbol{T}\boldsymbol{S}^T\boldsymbol{\varepsilon}^* \tag{8-12}$$

in which the terms within the round brackets are the fives strain modes in element coordinates r, s which are transformed by $\boldsymbol{T}$ to the global coordinates. This transformation was presented in Section 3-2. The variables k_r and k_s in Equation 8-12 indicate the magnitude of bending strains and $\bar{\boldsymbol{\varepsilon}}$ contains the other three modes. The expressions for $\boldsymbol{S}$ and $\boldsymbol{\varepsilon}^*$ are shown in Equation (8-13):

$$\boldsymbol{S} = \begin{bmatrix} 1 & 0 & 0 \\ 0 & 1 & 0 \\ 0 & 0 & 1 \\ s & 0 & 0 \\ 0 & r & 0 \end{bmatrix} \qquad \boldsymbol{\varepsilon}^* = \begin{pmatrix} \bar{\varepsilon}_r \\ \bar{\varepsilon}_s \\ \bar{\gamma}_{rs} \\ k_r \\ k_s \end{pmatrix} \tag{8-13}$$

Similarly the assumed stress is given as:

$$\breve{\boldsymbol{\sigma}} = \boldsymbol{T}_\sigma \boldsymbol{S}^T \boldsymbol{\sigma}^* = \boldsymbol{T}^{-T} \boldsymbol{S}^T \boldsymbol{\sigma}^* \tag{8-14}$$

with:

$$\boldsymbol{\sigma}^* = \begin{pmatrix} \bar{\sigma}_r & \bar{\sigma}_s & \bar{\tau}_{rs} & m_r & m_s \end{pmatrix}^T \tag{8-15}$$

In this equation m_r and m_s denote the bending stress modes, equivalently to k_r and k_s in Equation (8-12). Note that the transformation matrix for stresses $\boldsymbol{T}_\sigma = \boldsymbol{T}^{-T}$ as has been presented in Section 3-2. Next, the Hu-Washizu principle is applied to the assumed stresses and strains by substitution into Equation (5-54). First Equation (5-54a) is applied below:

$$\begin{aligned} 0 &= \int_\Omega \boldsymbol{T}^{-T} \boldsymbol{S}^T \delta\boldsymbol{\sigma}^* \cdot \left(\boldsymbol{\varepsilon} - \boldsymbol{T}\boldsymbol{S}^T \boldsymbol{\varepsilon}^* \right) d\Omega \\ &= \int_\Omega \delta\boldsymbol{\sigma}^{*T} \left[\boldsymbol{S}\boldsymbol{T}^{-1}\boldsymbol{\varepsilon} - \boldsymbol{S}\boldsymbol{S}^T \boldsymbol{\varepsilon}^* \right] d\Omega \end{aligned} \tag{8-16}$$

Solving this equation for $\boldsymbol{\varepsilon}^*$ ans substituting the result into Equation (8-12) gives:

$$\breve{\boldsymbol{\varepsilon}} = \boldsymbol{T}\boldsymbol{S}^T \boldsymbol{M}_e^{-1} \int_\Omega \boldsymbol{S}\boldsymbol{T}^{-1} \boldsymbol{\varepsilon} d\Omega \tag{8-17}$$

in which:

$$\boldsymbol{M}_e = \int_\Omega \boldsymbol{S}\boldsymbol{S}^T d\Omega \qquad \Rightarrow \qquad \boldsymbol{M}_e = \boldsymbol{M}_e^T \tag{8-18}$$

Equation (8-17) contains an integral of the strains over the element, which means that the assumed strain depends on the strains in all integration points. For this reason it is convenient to construct a 12×1 strain vector $\breve{\boldsymbol{\varepsilon}}_e$ containing the strains at each integration point. The assumed strain then becomes as shown in Equation (8-19):

$$\breve{\boldsymbol{\varepsilon}}_e = \boldsymbol{T}_e \boldsymbol{S}_e^T \boldsymbol{M}_e^{-1} \boldsymbol{S}_e \boldsymbol{T}_e^{-1} \boldsymbol{W}_e \boldsymbol{\varepsilon}_e \tag{8-19}$$

in which the subscript e represents the matrix for the full element (i.e. containing all four integration points). The expressions for the matrices with this subscript are given in Equation (8-20) together with the matrix sizes:

$$\breve{\boldsymbol{\varepsilon}}_e = \begin{bmatrix} \breve{\boldsymbol{\varepsilon}}_1^T & \breve{\boldsymbol{\varepsilon}}_2^T & \breve{\boldsymbol{\varepsilon}}_3^T & \breve{\boldsymbol{\varepsilon}}_4^T \end{bmatrix}^T \qquad (12 \times 1) \tag{8-20a}$$

$$\boldsymbol{\varepsilon}_e = \begin{bmatrix} \boldsymbol{\varepsilon}_1^T & \boldsymbol{\varepsilon}_2^T & \boldsymbol{\varepsilon}_3^T & \boldsymbol{\varepsilon}_4^T \end{bmatrix}^T \qquad (12 \times 1) \tag{8-20b}$$

$$\boldsymbol{T}_e = \text{diag} \begin{bmatrix} \boldsymbol{T}_1 & \boldsymbol{T}_2 & \boldsymbol{T}_3 & \boldsymbol{T}_4 \end{bmatrix} \qquad (12 \times 12) \tag{8-20c}$$

$$\boldsymbol{S}_e = \begin{bmatrix} \boldsymbol{S}_1 & \boldsymbol{S}_2 & \boldsymbol{S}_3 & \boldsymbol{S}_4 \end{bmatrix} \qquad (5 \times 12) \tag{8-20d}$$

$$\boldsymbol{W}_e = \text{diag} \begin{bmatrix} \boldsymbol{W}_1 & \boldsymbol{W}_2 & \boldsymbol{W}_3 & \boldsymbol{W}_4 \end{bmatrix} \qquad (12 \times 12) \tag{8-20e}$$

in which:

$$\boldsymbol{W}_i = t \cdot \det \boldsymbol{J}_i \begin{bmatrix} 1 & 0 & 0 \\ 0 & 1 & 0 \\ 0 & 0 & 1 \end{bmatrix} \tag{8-21}$$

As can be seen from Equation (8-19) the integral over the element is performed by numerical integration using the determinants of the Jacobian as the weight factor. Equation (8-19) is written using new variables $\boldsymbol{H}_e$ and $\boldsymbol{P}_e$:

$$\breve{\boldsymbol{\varepsilon}}_e = \boldsymbol{H}_e \boldsymbol{W}_e \boldsymbol{\varepsilon}_e = \boldsymbol{P}_e \boldsymbol{\varepsilon}_e \qquad \Rightarrow \qquad \boldsymbol{P}_e^T = \boldsymbol{W}_e^T \boldsymbol{H}_e^T = \boldsymbol{W}_e \boldsymbol{H}_e^T \tag{8-22}$$

in which:

$$\boldsymbol{H}_e = \boldsymbol{T}_e \boldsymbol{S}_e^T \boldsymbol{M}_e^{-1} \boldsymbol{S}_e \boldsymbol{T}_e^{-1} \tag{8-23}$$

The expression for $\boldsymbol{P}_e$ as a function of the entries of the Jacobian $\boldsymbol{J}$ has been presented in Appendix B. Next Equation (5-54b), which represents the variation of the Hu-Washizu principle with respect to assumed strains, is applied using the assumed stress and strain:

$$\begin{aligned} 0 &= \int_\Omega \boldsymbol{T}\boldsymbol{S}^T \delta\boldsymbol{\varepsilon}^* \cdot \left(\boldsymbol{\sigma} - \boldsymbol{T}^{-T} \boldsymbol{S}^T \boldsymbol{\sigma}^* \right) d\Omega \\ &= \int_\Omega \delta\boldsymbol{\varepsilon}^{*T} \left[\boldsymbol{S}\boldsymbol{T}^T \boldsymbol{\sigma} - \boldsymbol{S}\boldsymbol{S}^T \boldsymbol{\sigma}^* \right] d\Omega \end{aligned} \tag{8-24}$$

In a similar way as for the strains, the expression for $\breve{\boldsymbol{\sigma}}_e$ is derived to be:

$$\begin{aligned} \breve{\boldsymbol{\sigma}}_e &= \boldsymbol{T}_e^{-T} \boldsymbol{S}_e^T \boldsymbol{M}_e^{-1} \boldsymbol{S}_e \boldsymbol{T}_e^T \boldsymbol{W}_e \boldsymbol{\sigma}_e \\ &= \boldsymbol{H}_e^T \boldsymbol{W}_e \boldsymbol{\sigma}_e \end{aligned} \tag{8-25}$$

Finally the variation of the Hu-Washizu principle with respect to the displacement, given in Equation (5-54c), is applied:

$$\begin{aligned} \boldsymbol{f} &= \int_\Omega \left(\frac{\partial \boldsymbol{\varepsilon}}{\partial \boldsymbol{u}} \right)^T \breve{\boldsymbol{\sigma}} d\Omega \\ &= \boldsymbol{B}_e^T \boldsymbol{W}_e \breve{\boldsymbol{\sigma}}_e \end{aligned} \tag{8-26}$$

Linearizing the right hand side of this equation with respect to the nodal displacement vector $\boldsymbol{v}$ yields the stiffness matrix as shown in Equation (8-27):

$$\boldsymbol{K}_e = \underbrace{\frac{\partial \boldsymbol{B}_e^T}{\partial \boldsymbol{v}} \boldsymbol{W}_e \breve{\boldsymbol{\sigma}}_e}_{\boldsymbol{K}_{e,I}} + \underbrace{\boldsymbol{B}_e^T \boldsymbol{W}_e \frac{\partial \breve{\boldsymbol{\sigma}}_e}{\partial \boldsymbol{v}}}_{\boldsymbol{K}_{e,II}} \tag{8-27}$$

The first part of this stiffness matrix is rewritten using Equation (8-25) to give:

$$\boldsymbol{K}_{e,I} = \frac{\partial \boldsymbol{B}_e^T}{\partial \boldsymbol{v}} \boldsymbol{W}_e \boldsymbol{H}_e^T \boldsymbol{W}_e \boldsymbol{\sigma}_e \tag{8-28}$$

By applying the chain rule the expression for $\boldsymbol{K}_{e,II}$ becomes as shown in Equation (8-29):

$$\begin{aligned} \boldsymbol{K}_{e,II} &= \boldsymbol{B}_e^T \boldsymbol{W}_e \frac{\partial \breve{\boldsymbol{\sigma}}_e}{\partial \boldsymbol{\sigma}_e} \frac{\partial \boldsymbol{\sigma}_e}{\partial \breve{\boldsymbol{\varepsilon}}_e} \frac{\partial \breve{\boldsymbol{\varepsilon}}_e}{\partial \boldsymbol{\varepsilon}_e} \frac{\partial \boldsymbol{\varepsilon}_e}{\partial \boldsymbol{v}} \\ &= \boldsymbol{B}_e^T \boldsymbol{W}_e \boldsymbol{H}_e^T \boldsymbol{W}_e \boldsymbol{C}_e^* \boldsymbol{H}_e \boldsymbol{W}_e \boldsymbol{B}_e \\ &= \boldsymbol{B}_e^T \boldsymbol{P}_e^T \boldsymbol{W}_e \boldsymbol{C}_e^* \boldsymbol{P}_e \boldsymbol{B}_e \\ &= \boldsymbol{B}_e^{*T} \boldsymbol{W}_e \boldsymbol{C}_e^* \boldsymbol{B}_e^* \end{aligned} \tag{8-29}$$

in which $\boldsymbol{C}_e^*$ is a block diagonal matrix containing the effective material stiffness matrices at the four integration points $\boldsymbol{C}_i^*$ and:

$$\boldsymbol{B}_e^* = \boldsymbol{P}_e \boldsymbol{B}_e = \frac{\partial \breve{\boldsymbol{\varepsilon}}_e}{\partial \boldsymbol{v}} \tag{8-30}$$

With this stiffness matrix and assumed stresses and strains the hybrid element has been obtained by consistently following the Hu-Washizu principle.

8-2-2 Stress Positiveness

The stress tensor $\boldsymbol{S}$ needs to be positive to have a stable solution to the optimization problem of minimizing the total potential energy in the membrane, as explained in Chapter 5. This constraint was used in Section 5-3 to derive the relaxed strain energy function.

It needs be verified that the hybrid element presented in this section preserves this positiveness of the stress tensor. If this is not the case a solution to the energy minimization problem is not guaranteed which decreases the robustness of the method. In this section an example is looked for in which a negative stress tensor appears in the hybrid element. Finding this example would prove that the formulation of the hybrid element does not always preserve positiveness of the stress tensor.

The stress tensor is positive if its determinant is positive, i.e. if its components satisfy Equation (8-31):

$$|\boldsymbol{\sigma}_i| = \sigma_{x,i}\sigma_{y,i} - \tau_{xy,i}^2 > 0 \tag{8-31}$$

Suppose an element of which the Jacobian equals the identity matrix, i.e. $\boldsymbol{J} = \boldsymbol{I}$. In the hybrid element the stresses in integration point 1 then become:

$$\breve{\sigma}_{x,1} = \frac{1}{2}\left(\sigma_{x,1} + \sigma_{x,2}\right) \tag{8-32a}$$

$$\breve{\sigma}_{y,1} = \frac{1}{2}\left(\sigma_{y,1} + \sigma_{y,4}\right) \tag{8-32b}$$

$$\breve{\tau}_{xy,1} = \frac{1}{4}\left(\tau_{xy,1} + \tau_{xy,2} + \tau_{xy,3} + \tau_{xy,4}\right) \tag{8-32c}$$

which follows from the expression of $\boldsymbol{P}_e$ in Appendix B. The determinant of the assumed stress tensor integration point 1 of the hybrid element becomes as shown in Equation (8-33):

$$|\breve{\boldsymbol{\sigma}}_1| = \frac{1}{4}\left(\sigma_{x,1} + \sigma_{x,2}\right)\left(\sigma_{y,1} + \sigma_{y,4}\right) - \frac{1}{16}\left(\tau_{xy,1} + \tau_{xy,2} + \tau_{xy,3} + \tau_{xy,4}\right)^2 \tag{8-33}$$

Next, suppose $\boldsymbol{\sigma}_1 = \boldsymbol{\sigma}_2 = \boldsymbol{\sigma}_4 > 0$ and $\boldsymbol{\sigma}_3 = k\boldsymbol{\sigma}_1$ with $k > 0$ are the stresses in the original element. Substitution into Equation (8-33) gives for $|\breve{\boldsymbol{\sigma}}_1|$:

$$|\breve{\boldsymbol{\sigma}}_1| = \sigma_{x,1}\sigma_{y,1} - \frac{1}{16}\left(3 + k\right)^2 \tau_{xy,1}^2 \tag{8-34}$$

From this equation it can be shown that:

$$k > \frac{4}{\tau_{xy,1}}\sqrt{\sigma_{x,1}\sigma_{y,1}} - 3 \qquad \Rightarrow \qquad |\breve{\boldsymbol{\sigma}}_1| < 0 \tag{8-35}$$

which shows that an example can be found in which positiveness of the assumed stress tensor is not preserved, therefore the consistent hybrid element is not robust.

8-2-3 Modified Hybrid Element

The consistent hybrid element formulation does not guarantee to preserve positiveness of the assumed stress tensor. For this reason a modified hybrid element is applied which does preserve this positiveness, however, this method is not entirely consistent with the Hu-Washizu principle.

In the modified hybrid element the assumed strains are as in the consistent hybrid element, but the assumed stresses are equal to the original stresses in the membrane, therefore these stresses maintain their positiveness. This modified scheme is shown in Equation (8-36):

$$\breve{\boldsymbol{\varepsilon}}_e = \boldsymbol{P}_e \boldsymbol{\varepsilon}_e \tag{8-36a}$$

$$\breve{\boldsymbol{\sigma}}_e = \boldsymbol{\sigma}_e \tag{8-36b}$$

$$\boldsymbol{K}_e = \frac{\partial \boldsymbol{B}_e^T}{\partial \boldsymbol{v}} \boldsymbol{W}_e \breve{\boldsymbol{\sigma}}_e + \boldsymbol{B}_e^{*T} \boldsymbol{W}_e \boldsymbol{C}_e^* \boldsymbol{B}_e^* \tag{8-36c}$$

$$\boldsymbol{R}_e = \boldsymbol{R}_v - \boldsymbol{B}_e^{*T} \boldsymbol{W}_e \boldsymbol{C}_e^* \boldsymbol{R}_{w,e} \tag{8-36d}$$

with $\boldsymbol{B}_e^*$ as in Equation (8-30). Equation (8-36c) shows that the first term of the stiffness matrix $\boldsymbol{K}_{e,I}$ is affected by the modification, whereas $\boldsymbol{K}_{e,II}$ is the same as the consistent part shown in Equation (8-29).

The residual force vector $\boldsymbol{R}_e$ in Equation (8-36d) is according to the consistent hybrid element formulation and is equivalent to its expression in Equation (5-46).

8-3 3D Elements

The three-dimensional quadrilateral element, Q3, is presented in this section in the same way as the T3 triangular element in Section 7-2. The element is described in a 3D Cartesian frame with coordinates $\boldsymbol{\Xi} = [X, Y, Z]^T$. These coordinates are transformed into the already familiar coordinates $\boldsymbol{\xi} = [x, y]^T$ to compute the shape functions over the element. Figure 8-3 shows the Q3 element in $\mathbb{R}^3$.

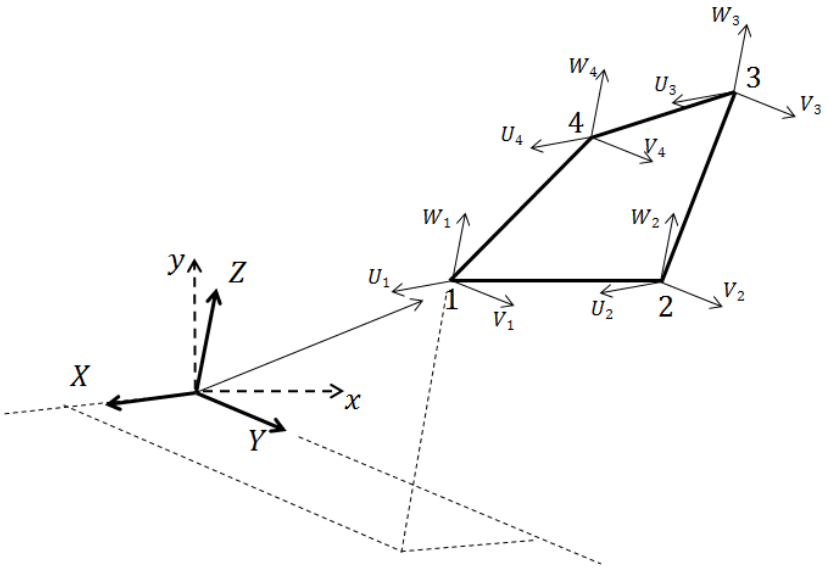

Figure 8-3: 3D quadrilateral finite element in $\mathbb{R}^3$.

The x, y-coordinate system has its origin in the origin of the (X, Y, Z) coordinate system. In general the element is curved and therefore the four nodes of the Q3 elements are not in one plane in the reference configuration. This curvature is neglected and the x, y-plane is chosen parallel to triangle formed by nodes 1, 2 and the center between nodes 3 and 4, referred to as point 5. The x-axis is chosen to be parallel to the vector from node 1 to node 2. The unit basis vectors $\boldsymbol{e}_x$ and $\boldsymbol{e}_y$ follow from this to be:

$$\boldsymbol{e}_x = \frac{\boldsymbol{r}_{12}}{\|\boldsymbol{r}_{12}\|} \tag{8-37}$$

$$\boldsymbol{e}_y = \frac{\boldsymbol{r}_{15} - (\boldsymbol{r}_{15} \cdot \boldsymbol{e}_x)\, \boldsymbol{e}_x}{\|\boldsymbol{r}_{15} - (\boldsymbol{r}_{15} \cdot \boldsymbol{e}_x)\, \boldsymbol{e}_x\|} \tag{8-38}$$

$$\tag{8-39}$$

with $\boldsymbol{r}_{ij}$ as given in Equation (7-9) and the subscript '5' represents the point in between nodes 3 and 4:

$$\boldsymbol{r}_5 = \frac{1}{2}\left(\boldsymbol{r}_3 + \boldsymbol{r}_4\right) \tag{8-40}$$

As with the triangular elements, the coordinates $\boldsymbol{\xi}$ of any material point inside the element is obtained by projection of the $\boldsymbol{\Xi}$ coordinates as shown in Equation (8-41):

$$\boldsymbol{\xi} = \boldsymbol{\Lambda}\boldsymbol{\Xi}; \qquad \boldsymbol{\Lambda} = \begin{bmatrix} \boldsymbol{e}_x^T \\ \boldsymbol{e}_y^T \end{bmatrix} \tag{8-41}$$

The $\boldsymbol{\xi}$ coordinates of the nodes are used to apply the first section of this chapter to compute the shape functions and their derivatives over the element as a function of $\boldsymbol{\eta} = [r, s]^T$. The position and displacement of any material point inside the element are obtained from the nodal vectors as shown in Equation (8-42):

$$\boldsymbol{r}_0 = \boldsymbol{N}\boldsymbol{\rho}_0 \qquad \boldsymbol{u} = \boldsymbol{N}\boldsymbol{v} \tag{8-42}$$

with:

$$\boldsymbol{\rho}_0 = \left[\begin{array}{cccccc} X_{0,1}, & Y_{0,1}, & Z_{0,1}, & \ldots, & X_{0,4}, & Y_{0,4}, & Z_{0,4} \end{array} \right]^T$$

$$\boldsymbol{v} = \left[\begin{array}{cccccc} U_1, & V_1, & W_1, & \ldots, & U_4, & V_4, & W_4 \end{array} \right]^T$$

$$\boldsymbol{N}(\boldsymbol{\eta}) = \left[\begin{array}{cccccccccccc} N_1 & 0 & 0 & N_2 & 0 & 0 & N_3 & 0 & 0 & N_4 & 0 & 0 \\ 0 & N_1 & 0 & 0 & N_2 & 0 & 0 & N_3 & 0 & 0 & N_4 & 0 \\ 0 & 0 & N_1 & 0 & 0 & N_2 & 0 & 0 & N_3 & 0 & 0 & N_4 \end{array} \right]$$

Chapter 9

Isogeometric Analysis

Isogeometric analysis is distinguished from isoparametric analysis mainly by its exact representation of the membrane geometry. It relies on a direct application of the computer aided design (CAD) representation of a geometric model, which is often available as the geometrical design is performed in specialized CAD software. The CAD representation of a geometry is based on non-rational basis functions and several control points. In an isogeometric analysis these basis functions and control points are directly used for the finite element analysis of the structure.

The non-rational basis functions were derived from the rational B-spline basis functions as presented in Section 9-1. Subsequently the non-rational NURBS basis functions and their capacity to represent different geometries are considered in Sections 9-2 and 9-3 respectively. The applications of these NURBS basis functions to finite element analysis is presented in Section 9-4. Note that this chapter is not intended to provide a complete discussion on isogeometric analysis, see for more depth [6, 20, 23].

9-1 B-Spline Basis Functions

B-spline basis functions are polynomial functions with a user specified polynomial order, which means that these are rational functions. In this section these basis functions are defined and characterized by a set of parameters. For this purpose, first a knot vector $\boldsymbol{\xi} = [\xi_1, \xi_2, ..., \xi_n]$, which is a ordered list of numbers, is defined. B-spline basis functions are defined over the range of this knot vector. The p-th order basis functions are computed recursively and denoted by $N_{i,p}(\xi)$ in which i is the counter for the shape function. In Equation (9-1) the 0-th order B-spline is defined.

$$N_{i,0}(\xi) = \begin{cases} 1 & \text{if } \xi_i \leq \xi \leq \xi_{i+1} \\ 0 & \text{otherwise} \end{cases} \tag{9-1}$$

Higher order basis function are then obtained by recursion:

$$N_{i,p}(\xi) = \frac{\xi - \xi_i}{\xi_{i+p} - \xi_i} N_{i,p-1}(\xi) + \frac{\xi_{i+p+1} - \xi}{\xi_{i+p+1} - \xi_{i+1}} N_{i+1,p-1}(\xi) \tag{9-2}$$

These shape functions have many properties which are listed in [6, 20, 23], one of which states that the sum of the shape functions equals to 1 over the whole domain. This is one of the reasons these basis function can be applied as shape functions in a finite element analysis. The first derivative of the basis functions $N_{i,p}(\xi)$, which is required in a finite element model, is computed as:

$$\frac{d}{d\xi}N_{i,p}\left(\xi\right) = \frac{p}{\xi_{i+p} - \xi_i}N_{i,p-1}\left(\xi\right) - \frac{p}{\xi_{i+p+1} - \xi_{i+1}}N_{i+1,p-1}\left(\xi\right) \tag{9-3}$$

Many properties of the shape functions are hidden in the knot vector $\boldsymbol{\xi}$ which therefore needs to be chosen carefully. To obtain p-th order basis functions on the domain $\xi = [0, 1]$, the knot vector is constructed as:

$$\boldsymbol{\xi} = [\underbrace{0, 0, ..., 0}_{p+1 \text{ times}}, \xi_{p+2}, \xi_{p+3}, ..., \xi_{n-p+1}, \underbrace{1, 1, ..., 1}_{p+1 \text{ times}}] \tag{9-4}$$

The derivatives of the spline at the knots ξ_i are continuous up to the $(p-1)$-th derivative. Note that the multiplicity of the first and the last knot is needed to obtain a non-zero shape function at these locations. For convenience, define the unrepeated knot vector $\boldsymbol{\xi}^* = [\xi_1^*, \xi_2^*, ..., \xi_n^*]$ as the collection of unique knots of the original knot vector. The original knot vector of order p is obtained from $\boldsymbol{\xi}^*$ as:

$$\boldsymbol{\xi} = [\underbrace{\xi_1^*, \xi_1^*, ..., \xi_1^*}_{p+1 \text{ times}}, \xi_2^*, \xi_3^*, ..., \xi_{n-1}^*, \underbrace{\xi_n^*, \xi_n^*, ..., \xi_n^*}_{p+1 \text{ times}}] \tag{9-5}$$

As stated above, the resulting basis function is continuous up to its $(p-1)$-th derivative. Let k be the derivative up to which the spline is continuous, i.e. $k = p-1$ in the example above. The value of k is referred to as the element connectivity as a knot marks the border of an element. Modifying the value of k is achieved by increasing the multiplicity of the interior knots, which are all knots except for the first and the last one. Decreasing the element connectivity by one is obtained by also increasing the multiplicity of these knots by one. Note that the value of k cannot exceed $p - 1$.

The parameters $\boldsymbol{\xi}^*$, p and k uniquely determine the original knot vector $\boldsymbol{\xi}$ and consequently the basis functions by Equations (9-1) and (9-2). As an example consider the unrepeated knot vector $\boldsymbol{\xi}^* = [0, \frac{1}{3}, \frac{2}{3}, 1]$, then for different values of p and k the knot vector $\boldsymbol{\xi}$ becomes as shown in Table 9-1.

p	k	**Knot vector $\boldsymbol{\xi}$**
1	0	$[0, 0, \frac{1}{3}, \frac{2}{3}, 1, 1]$
2	0	$[0, 0, 0, \frac{1}{3}, \frac{1}{3}, \frac{2}{3}, \frac{2}{3}, 1, 1, 1]$
2	1	$[0, 0, 0, \frac{1}{3}, \frac{2}{3}, 1, 1, 1]$
3	0	$[0, 0, 0, 0, \frac{1}{3}, \frac{1}{3}, \frac{1}{3}, \frac{2}{3}, \frac{2}{3}, \frac{2}{3}, 1, 1, 1, 1]$
3	2	$[0, 0, 0, 0, \frac{1}{3}, \frac{2}{3}, 1, 1, 1, 1]$

Table 9-1: Overview of knots vectors $\boldsymbol{\xi}$ for $\boldsymbol{\xi}^* = [0, \frac{1}{3}, \frac{2}{3}, 1]$ and different values of p and k.

Note that in general the element connectivity k can be chosen for each knot separately, which may be useful in other cases outside the scope of this thesis. The basis functions corresponding to the different polynomial orders p and element connectivities k presented in Table 9-1 are shown in Figure 9-1.

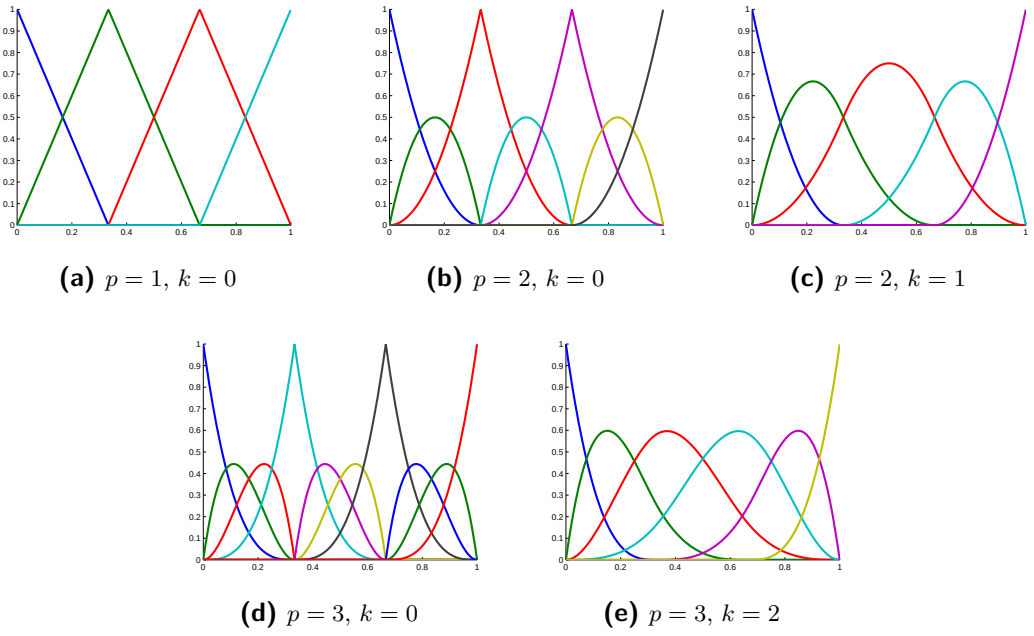

(a) $p = 1,\ k = 0$ **(b)** $p = 2,\ k = 0$ **(c)** $p = 2,\ k = 1$

(d) $p = 3,\ k = 0$ **(e)** $p = 3,\ k = 2$

Figure 9-1: B-spline shape functions for $\boldsymbol{\xi}^* = [0, \frac{1}{3}, \frac{2}{3}, 1]$.

The basis functions in Figure 9-1a are the same as the piecewise linear shape functions used in isoparametric elements. Note that for all basis functions with $k = 0$, at each knot all basis functions are equal to 0, except for one. The connection between the presented B-splines basis function and the familiar finite elements can now be partly established. The unrepeated knot vector $\boldsymbol{\xi}^*$ is related to finite elements as each interval in this knot vector represents an element. In the example of Figure 9-1 this means that three finite elements are present. Let n_e the number of elements, then the number of shape functions n_s is computed as:

$$n_s = p + 1 + (n_e - 1)(p - k) \tag{9-6}$$

Note that the knots are not equivalent to the nodes in a finite element model. This equivalent of the node is discussed in Section 9-3 on spline geometries.

9-2 NURBS Basis Functions

The B-splines presented in Section 9-1 are polynomials and thus rational functions. Irrational curves, such as perfect circles, can therefore not be exactly represented by these splines. For this purpose the non-rational NURBS basis functions are introduced, which are presented in this section. Essentially the NURBS basis functions $R_{i,p}(\xi)$ are weighted versions of the

B-splines $N_{i,p}(\xi)$ as shown in Equation (9-7):

$$R_{i,p}(\xi) = \frac{N_{i,p}(\xi)\, w_i}{W(\xi)} = \frac{N_{i,p}(\xi)\, w_i}{\sum_{j=1}^{n_s} N_{j,p}(\xi)\, w_j} \tag{9-7}$$

This formulation guarantees that the sum of the basis functions remains equal to one over the whole domain as required. When choosing $w_i = c\ \forall i$, the B-spline basis functions are returned. The first derivative of the NURBS basis functions is computed as:

$$\frac{d}{d\xi} R_{i,p}(\xi) = w_i \frac{N'_{i,p}(\xi)\, W(\xi) - N_{i,p}(\xi)\, W'(\xi)}{W(\xi)^2} \tag{9-8}$$

9-3 NURBS Geometries

The NURBS basis functions can be applied to represent irrational curves, which is considered in this section. The representation of a curve $\boldsymbol{C}$ is shown in Equation (9-9):

$$\boldsymbol{C}(\xi) = \sum_{i=1}^{n_s} R_{i,p}(\xi)\, \boldsymbol{P}_i \tag{9-9}$$

in which $\boldsymbol{P}_i$ is a control point location, i.e. $\boldsymbol{P}_i = [x_i, y_i, z_i]^T$. The control points determine the actual location of the curve in physical space. Each of the control points contains a weight w_i in order to form the basis functions $R_{i,p}$ in Equation (9-7). Note that the number of control points needs to be equal to the number of shape functions as computed in Equation (9-6). As an example a quarter of the unit circle is represented by NURBS basis functions in the x, y-plane. For this circle the basis functions need to have at least $p = 2$. When only one element is applied, i.e. $\boldsymbol{\xi}^* = [\xi_1^*, \xi_2^*]$, three control points are required which are located at $(x, y) = (0, 0)$, $(1, 0)$ and $(1, 1)$. The weights of these control points are equal to 1, $1/\sqrt{2}$ and 1 respectively. The representation of the quarter circle is shown in Figure 9-2 as well as the B-spline curve with the same control points.

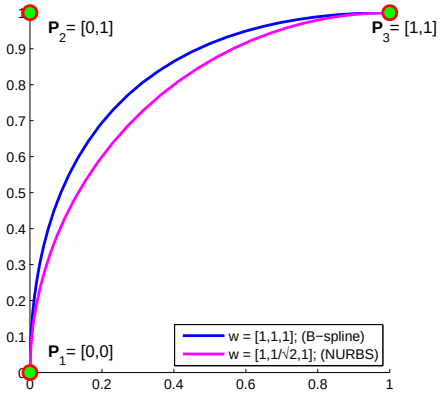

Figure 9-2: Representation of a quarter circle with NURBS.

Any curve which can be represented by p-th order basis functions can also be represented when the order is increased by 1, which is called p-refinement. The knot vector required for the refined curve is obtained by applying Section 9-1. Assuming the number of elements $n_e = 1$, the number of shape functions increases by one as a result of p-refinement which follows from Equation (9-6). This means that an extra control point $\boldsymbol{P}$ is required to represent the same curve. To compute the locations of the new control points, define:

$$\boldsymbol{P}_i^w = [w_i x_i, w_i y_i, w_i z_i, w_i]^T \tag{9-10}$$

The control point locations after p-refinement $\bar{\boldsymbol{P}}_i^w$ are then computed as:

$$\bar{\boldsymbol{P}}_i^w = (1 - \alpha_i)\, \boldsymbol{P}_i^w + \alpha_i \boldsymbol{P}_{i-1}^w \tag{9-11}$$

with:

$$\alpha_i = \frac{i-1}{p+1} \qquad i = 1, ..., p+2 \tag{9-12}$$

The computed $\bar{\boldsymbol{P}}_i^w$ is transformed into the real coordinates $\bar{\boldsymbol{P}}_i$ by Equation (9-10). Figure 9-3 shows the p-refinement of the quarter circle to third and fourth order basis functions.

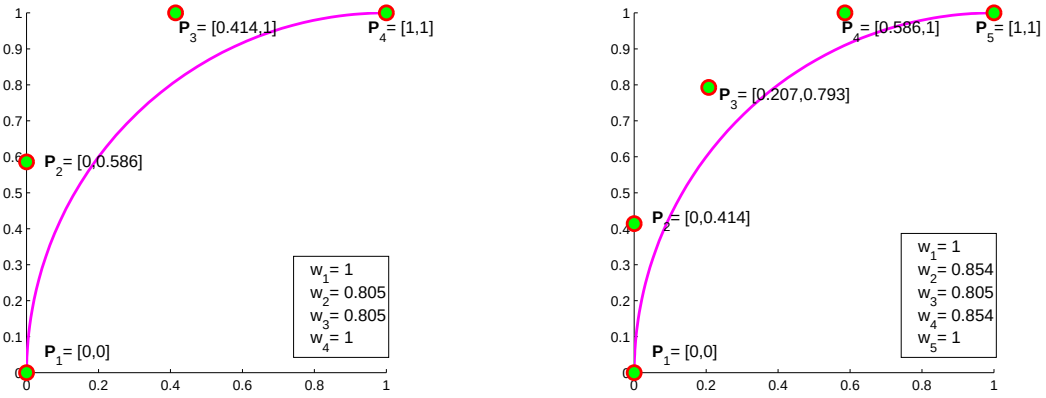

(a) $p = 3,\ k = 1$ **(b)** $p = 4,\ k = 1$

Figure 9-3: p-refinement on quarter-circle for $\boldsymbol{\xi}^* = [0, 1]$.

In addition to p-refinement also h-refinement can be applied to any representation of a curve. This is achieved by adding an extra knot to the knot vector $\boldsymbol{\xi}$. As a result the number of control points increases. Suppose the new knot has location $\bar{\xi}$ with $\xi_s < \bar{\xi} \leq \xi_{s+1}$, then the locations of the new control points are computed as:

$$\bar{\boldsymbol{P}}_i^w = (1 - \alpha_i)\, \boldsymbol{P}_i^w + \alpha_i \boldsymbol{P}_{i-1}^w \tag{9-13}$$

with:

$$\alpha_i = \begin{cases} 1 & \text{if } i \leq s - p \\ \dfrac{\bar{\xi} - \xi_i}{\xi_{i+p} - \xi_i} & \text{if } s - p + 1 \leq i \leq s \\ 0 & \text{if } s + 1 \leq i \end{cases} \tag{9-14}$$

Two examples of h-refinement applied to the quarter circle are shown in Figure 9-4. In Figure 9-4a a knot is inserted right in between the two existing knots and in Figure 9-4a the additional knot is biased towards one side.

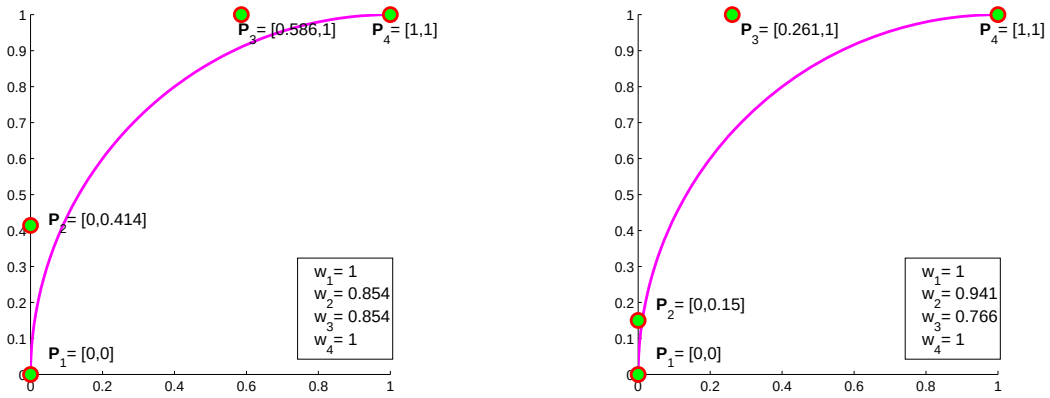

(a) $\boldsymbol{\xi}^* = [0, 0.5, 1]$ **(b)** $\boldsymbol{\xi}^* = [0, 0.2, 1]$

Figure 9-4: h-refinement on quarter-circle for $p = 2$, $k = 1$.

These p- and h- refinements are sufficient to create all curves required in this thesis. In order to represent the quarter circle by e.g. 10 elements with $p = 5$ and $k = 2$, the applied procedure is as follows: first a p-refinement is applied to the single element, second order representation of the quarter circle in order to obtain the single element, fifth order representation. Subsequently the unrepeated knot vector $\boldsymbol{\xi}^*$ is chosen, which contains 10+1 entries. This vector, combined with the values for p and k results in the knot vector $\boldsymbol{\xi}$ by Section 9-1. The knots in this vector which are not in the knot vector of the single element, fifth order representation are inserted one by one using the h-refinement procedure.

Note that the control points presented in this section are the equivalent of the nodes in isoparameteric finite elements. An important note is that these nodes are not necessarily located on the curve as is the case with the quarter circle.

9-4 Finite Element Analysis

The NURBS basis functions can be applied as shape functions in a finite element analysis as is discussed in this section. The basic principle of representing the initial configuration and displacement field is the same as for isoparametric elements:

$$\boldsymbol{r}_0(\boldsymbol{\xi}) = \boldsymbol{N}(\boldsymbol{\xi})\,\boldsymbol{\rho}_0 \tag{9-15}$$

$$\boldsymbol{u}(\boldsymbol{\xi}) = \boldsymbol{N}(\boldsymbol{\xi})\,\boldsymbol{v} \tag{9-16}$$

in which $\boldsymbol{\rho}_0$ contains the locations of the control points which are the equivalent of nodes. This means that the representation of the membrane in Equation (9-15) is exact and only the displacement field is an approximation. Note that for finite element analysis on a curve the entries of the shape function matrix $\boldsymbol{N}$ are the NURBS basis functions directly. For the

analysis of surface like the membrane the shape function matrix is built up slightly different, because two knot vectors, say $\boldsymbol{\xi}$ and $\boldsymbol{\eta}$, are required to represent the surface. For a simple rectangle the first knot vector would e.g. represent its width and the second the height of the rectangle. As both knot vectors result in a set of basis functions they need to be combined, i.e. multiplied, to fill the shape function matrix. The derivative of this matrix in ξ and η direction is then obtained by the product rule. For more detailed discussion on the extension from curves to surface and the consequences for finite element analysis, one should consult the literature [6, 20, 23].

As mentioned in Section 9-1 the intervals of the unrepeated knot vector $\boldsymbol{\xi}^*$ are equivalent to the elements in a finite element analysis. As shown Figure 9-1 the NURBS basis functions are only non-zero on a limited number of elements, which means that Equations (9-15) and (9-16) can be considered at the element level as was the case for the isoparametric finite elements. The number of non-zero basis functions over an element represents the number of control points per element. Consider the basis functions shown in Figure 9-1e for which the relation between the elements and the corresponding control points is shown in Table 9-2.

Element	**Range**	**Control points**
1	$\xi = [0, \frac{1}{3}]$	1,2,3,4
2	$\xi = [\frac{1}{3}, \frac{2}{3}]$	2,3,4,5
3	$\xi = [\frac{2}{3}, 1]$	3,4,5,6

Table 9-2: Overview of connection between elements and nodes for $\boldsymbol{\xi}^* = [0, \frac{1}{3}, \frac{2}{3}, 1]$, $p = 3$, $k = 2$.

From Table 9-2 it can be seen that each element consists of four nodes, some of which are shared with other elements. The second element in the table shares all of its nodes with one of the two neighboring elements. Suppose that to represent a surface the second knot vector $\boldsymbol{\eta}$ is chosen the same as $\boldsymbol{\xi}$. In the example of Table 9-2 this would mean that each two-dimensional element consists of $4 \times 4 = 16$ nodes. The nodal position and displacement vectors and the shape function matrix for a three-dimensional analysis then look like:

$$\boldsymbol{\rho}_0 = \begin{bmatrix} X_{0,1}, & Y_{0,1}, & Z_{0,1}, & \ldots, & X_{0,16}, & Y_{0,16}, & Z_{0,16} \end{bmatrix}^T$$

$$\boldsymbol{v} = \begin{bmatrix} U_1, & V_1, & W_1, & \ldots, & U_{16}, & V_{16}, & W_{16} \end{bmatrix}^T$$

$$\boldsymbol{N} = \begin{bmatrix} N_1 & 0 & 0 & N_2 & 0 & 0 & \cdots & N_{16} & 0 & 0 \\ 0 & N_1 & 0 & 0 & N_2 & 0 & & 0 & N_{16} & 0 \\ 0 & 0 & N_1 & 0 & 0 & N_2 & & 0 & 0 & N_{16} \end{bmatrix}$$

in which the entries N_i are composed of the NURBS basis functions for knot vectors $\boldsymbol{\xi}$ and $\boldsymbol{\eta}$.

To construct the stiffness matrix $\boldsymbol{K}_e$ and residual force $\boldsymbol{R}_e$ of an element, Equations (5-45) and (5-46) are applied. In the case of NURBS basis functions two Jacobians are required in the numerical integration. The first Jacobian represents the change from the Gauss-integration domain $[-1, 1]$ to the knot vector domain $\boldsymbol{\xi}$, whereas the second Jacobian describes the transformation from knot vector domain to the physical space. Note that for the quadrilateral

element in Chapter 8 only one Jacobian was applied from the Gauss-integration domain to the physical space, also note that for higher order NURBS basis functions more integration points are required on the Gauss-integration domain. For a two-dimensional knot space, i.e. two knot vectors, the number of integration points per element is $(p+1) \times (p+1)$.

To evaluate the performance of the NURBS basis functions a one dimensional ordinary differential equation (ODE) is solved using isogeometric analysis. The ODE with boundary conditions is given in Equation (9-19):

$$u_{xx} + \sin \frac{2\pi x}{L} = 0; \qquad u(0) = 0; \quad u(L) = 1 \tag{9-17}$$

The exact solution to this ODE is:

$$u(x) = \left(\frac{L}{2\pi}\right)^2 \sin \frac{2\pi x}{L} + \frac{x}{L} \tag{9-18}$$

The numerical and exact values for $u(x)$ for 32 elements with $p = 3$ and $k = 2$ are shown in Figure 9-5.

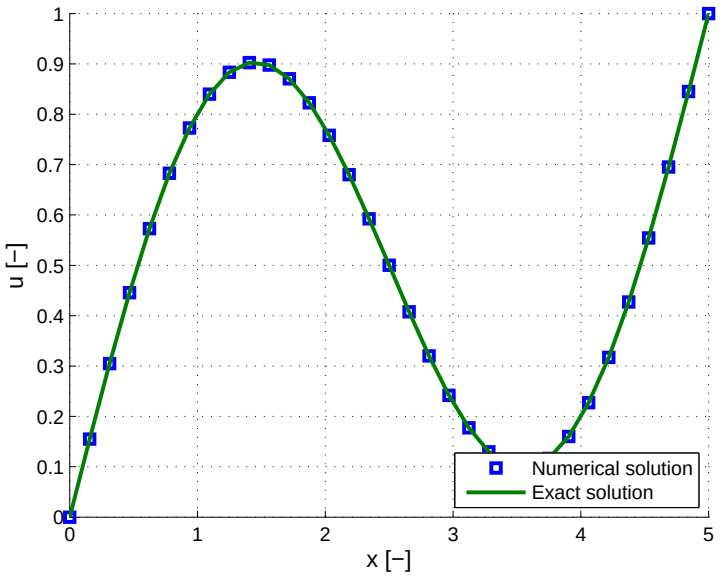

Figure 9-5: Isogeometric analysis results for ODE for $\boldsymbol{\xi}^* = [0, \frac{1}{32}, \frac{2}{32}, ..., 1]$, $p = 3$, $k = 2$.

To assess the performance the NURBS basis functions for different values of p and k a convergence study is performed. The numerical error ε is computed as:

$$\varepsilon = \frac{\int_0^L |u - u_{exact}| \, dx}{\int_0^L u_{exact} dx} \tag{9-19}$$

The convergence behavior for different basis functions is displayed in Figure 9-6. As the element size $h \propto 1/n_e$, a slope of $-s$ in the convergence plots corresponds to a rate of

convergence of $\mathcal{O}(h^s)$. Note that the case $p = 1$, $k = 0$ represents the use of standard isoparametric 1D elements.

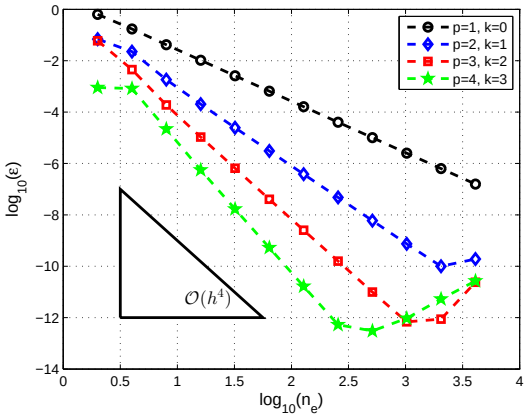

(a) $k = p - 1$

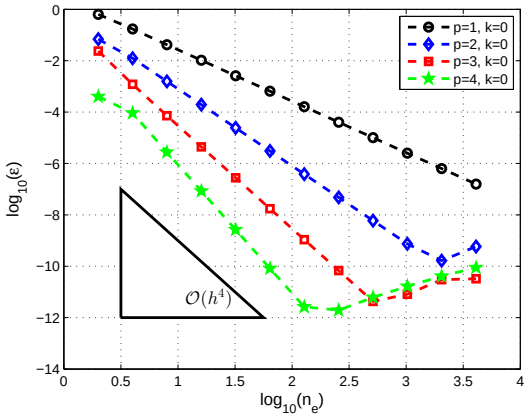

(b) $k = 0$

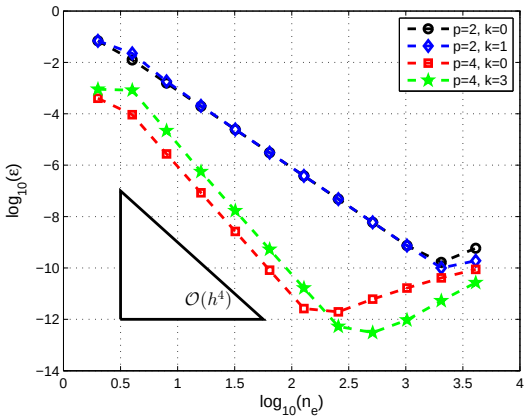

(c) Comparison between different k-values

Figure 9-6: Convergence analysis for 1D isogeometric finite elements.

The results for basis functions with the maximum element connectivity of $k = p - 1$ are shown in Figure 9-6a, whereas the results in Figure 9-6b are generated using zeroth order connectivity. The effect of this value of k on the error convergence is shown in Figure (9-6c). All convergence plots show an increase in rate of convergence for increasing values of p, which is as expected. The order of convergence is close to p itself and the connectivity between the elements does not alter this rate of convergence significantly.

Chapter 10

Numerical Results

Several numerical examples of the proposed finite elements are presented in this chapter. A rectangular membrane strip under shear loading was used to assess the performance of different types of finite elements in Section 10-1. The verification of the proposed method was performed using an analytical solution together with a convergence analysis of the numerical results. Two annular membranes loaded in lateral deflection and twisting were considered to test the method in Sections 10-2 and 10-3. Severe slacking of the membrane was modeled using a rectangular plate with a hole under shear loading in Section 10-4. The validation of the finite elements was performed with a pressurized membrane beam loaded in bending in Section 10-5. The load-displacement curve of the proposed method was compared with experimental results.

It should be noted that all load cases were displacement controlled because of multiple reasons. First the analytical solution used for verification was displacement controlled and many challenging load cases were expressed more easily in terms of displacements rather than forces. Another reason was that in case of softening behavior of the structure, as with the pressurized beam under bending, a displacement controlled method was numerically more stable.

The material law considered in all examples was the incompressible neo-Hookean law unless stated otherwise. In the latter case the linear elastic Saint-Venant material law was applied. Unless stated otherwise, the modulus of elasticity was assumed to be $E = 2850\text{MPa}$ and the membrane thickness $t = 0.01\text{mm}$, which both represent the material properties used for validation of the elements.

10-1 Sheared Membrane Strip

A rectangular membrane strip under shear and tension loading is considered in this section. This example is one of the few relatively complex cases for which an analytical solution exists, therefore it was used to extensively check the performance of the finite elements presented in previous chapters. The analytical Mansfield solution [14] was applied to perform a convergence analysis for different mesh types to verify the numerical results.

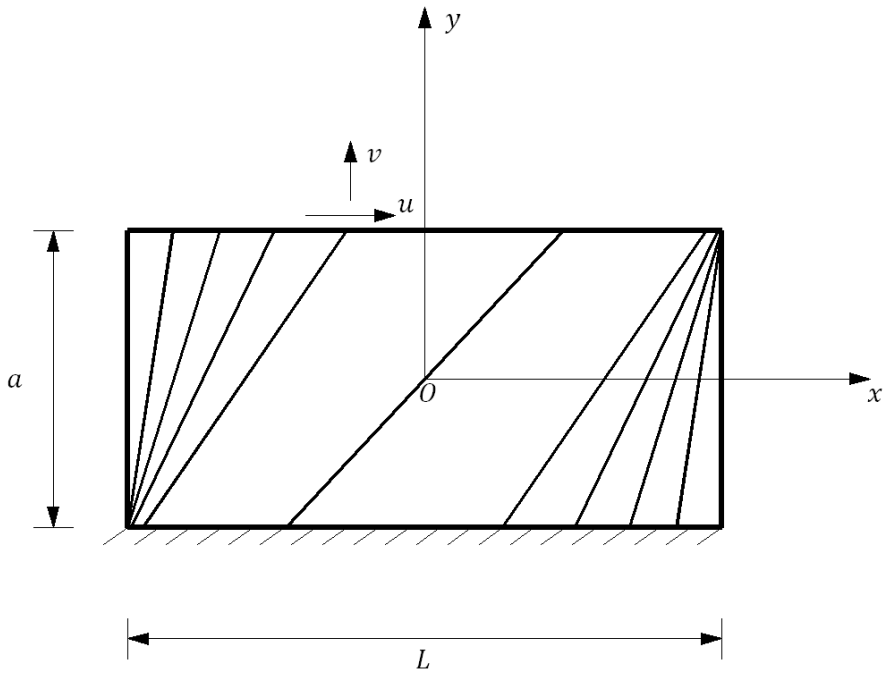

Figure 10-1: Sketch of rectangular membrane strip under displacement loading.

A sketch of the load case of the membrane strip is shown in Figure 10-1. It shows that the bottom edge of the plate is clamped whereas the top edge is displaced in x and y direction by u and v respectively. The straight lines in the strip represent the straight tension rays as obtained from the Mansfield solution. The derivation of this analytical solution is presented in Appendix C using a slightly different approach than Mansfield applied.

10-1-1 Isoparametric Analysis

The isoparametric analysis is considered in detail in this section because the isoparametric finite elements are used widely in practice and have shown good performance in computational modeling. To perform a thorough verification of the proposed method several different mesh types are considered. These consist of either triangular or quadrilateral elements in different configurations. The different mesh types used to represent the rectangular membrane strip are shown in Figure 10-2. Figures 10-2a and 10-2c show the best-conditioned meshes for the triangular and quadrilateral elements respectively. For the triangular elements these are equilateral triangles and for the quadrilateral elements the best-conditioned mesh consists of squares only.

For the meshes in Figures 10-2b and 10-2d the nodes initially are positioned the same as in Figures 10-2a and 10-2c respectively, but are then biased towards the corners of the plate. This bias is applied because the stresses in the membrane for the current load case are singular in two of the corners of the membrane strip. From the analytical solution it is found that this singularity is of the form $1/\sqrt{r}$ with r the distance from the corner. Integration of such a singularity is achieved by the change of variables $s = r^2$, which effectively means biasing the nodes towards the corner. This change of variables indicates that this bias should be quadratic, therefore it is expected that the second order mesh bias which is applied in Figures

10-2b and 10-2d will yield better results in this specific example.

Figures 10-2e and 10-2f show a skewed and irregular quadrilateral mesh respectively. Both meshes are conditioned worse than the square or rectangular elements and thus are expected to yield less accurate results. The reason for considering these meshes was to evaluate the performance of ill-conditioned meshes. It should be noted that the mesh in Figure 10-2f was generated using a random number generator.

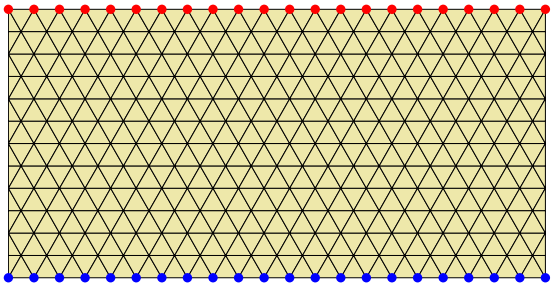

(a) Tria elements

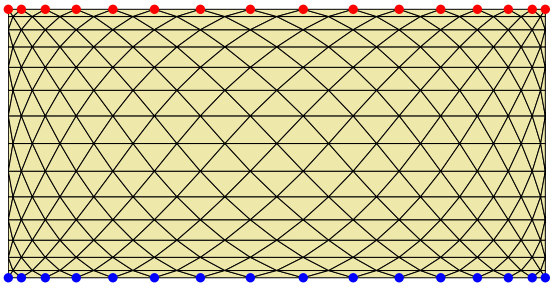

(b) Tria elements, 2nd order biased

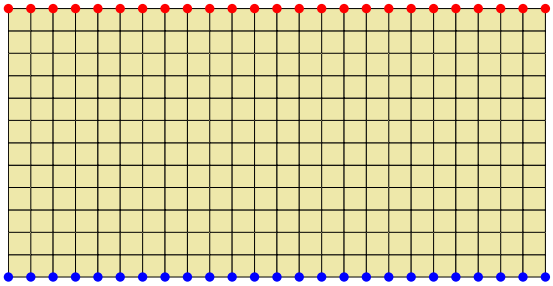

(c) Quad elements

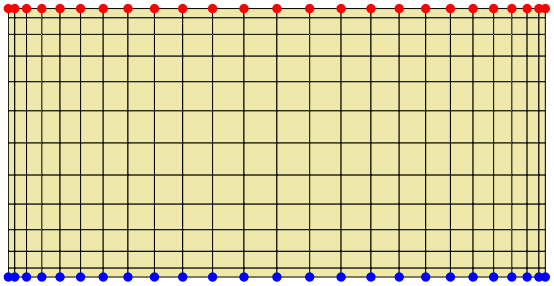

(d) Quad elements, 2nd order biased

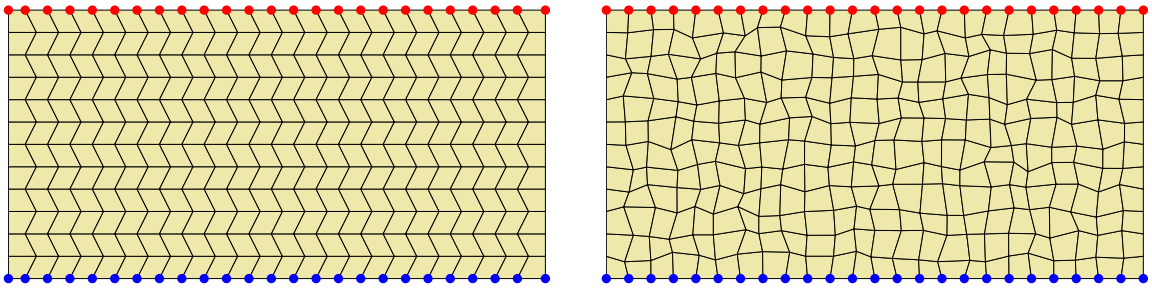

(e) Quad elements, skewed mesh **(f)** Quad elements, irregular mesh

Figure 10-2: Example meshes of rectangular membrane strip.

The deformed configuration of the membrane strip under large pure shear deformation is shown Figure 10-3. The vertical edges of the membrane are curved in the deformed configuration which is due to the Poisson's effect of the material. For neo-Hookean materials the equivalent Poisson's ratio is $\nu = 0.5$ at zero stress as shown in Section 5-7.

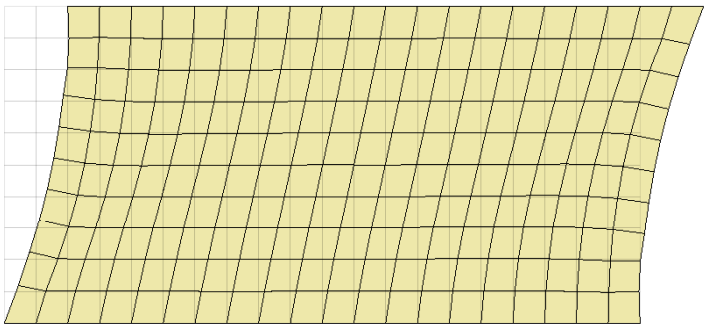

Figure 10-3: Membrane deformation under shear deformation with $a = 50\text{mm}$, $L = 100\text{mm}$, $u = 15\text{mm}$, $v = 0\text{mm}$.

The first principal stresses in the membrane strip for two different load cases are shown in Figure 10-4. Figures 10-4a and 10-4b display the results for pure shear deformation and in Figures 10-4c and 10-4d a tensile deformation is added.

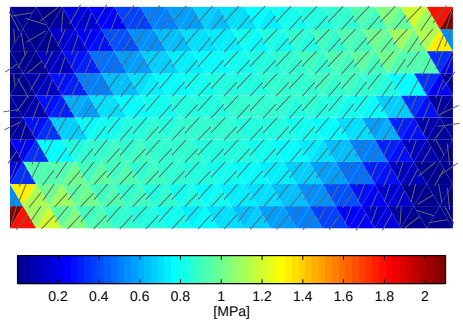

(a) Tria elements, $u = 0.03$mm, $v = 0$mm.

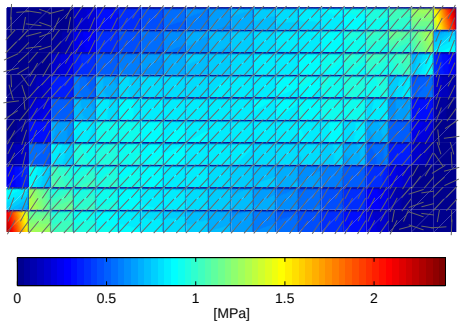

(b) Quad elements, $u = 0.03$mm, $v = 0$mm.

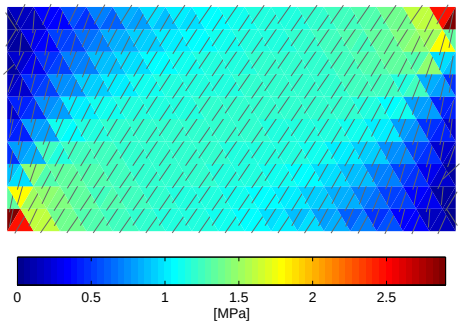

(c) Tria elements, $u = 0.03$mm, $v = 0.01$mm.

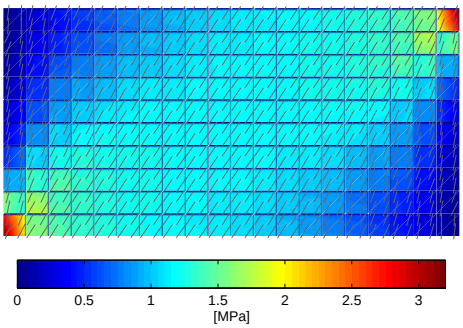

(d) Quad elements, $u = 0.03$mm, $v = 0.01$mm.

Figure 10-4: Contour plot of first principal stresses σ_1 for two different load cases with $a = 50$mm, $L = 100$mm.

Several observations can be made from these results. First the results show that the stresses are constant in triangular elements and vary linearly in the quadrilateral elements. This is caused by the shape functions used in the derivation of the elements, see Chapters 7 and 8, also the stresses are not continuous at the border between elements, which is inherent to the isoparametric finite elements since they are only forced to be $\mathbb{C}^0$ on the element boundaries.

All stresses in the membrane are positive, as can be seen in Figure 10-4, which means that the main constraint as derived in Chapter 5 is satisfied. The dark lines in the figure represent the direction of the first principal stresses. As predicted by the analytical solution these tension rays form straight lines. In the regions where σ_1 is close to zero the membrane is close to slacking. Figure 10-4 shows that in these regions the direction of the stresses are not computed very accurately as they should form straight tension rays but appear to be more randomly oriented. An explanation can be found in the fact that these regions are very close

to the boundary of the feasible region for the stresses ($\boldsymbol{S} > 0$). Near this boundary the barrier function, see Section 5-3, governed by penalty parameter μ is significant and interferes with the solution. Another contribution to this 'randomness' lies in the fact that in the regions which are almost slacked the effective membrane stiffness is close to zero in all directions, which means that the stress-strain relation is close to singular. The finite numerical accuracy of the computer may cause round-off errors in this case.

Comparing the two different load cases shown in Figure 10-4 it is observed that for the second load case, including tensile displacement, the stress directions are modeled more accurate near the corners which are close to slacking. This is explained by the fact that the tensile deformation causes the stresses to increase and thus move away from the boundary of the feasible region of the stresses.

The analytical solution from Mansfield states that the second principal stress is exactly zero over the whole membrane strip. In the numerical model this is not the case as the penalty parameter μ is always strictly positive. From Figure 10-5 it can be seen that σ_2 is close to zero in the whole membrane for both loading conditions.

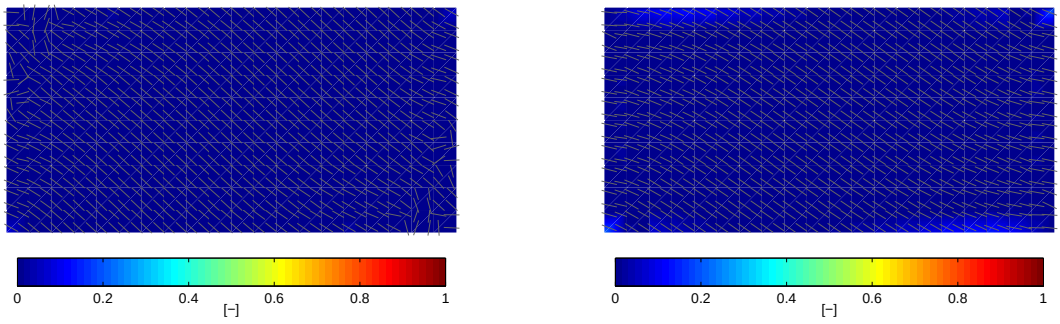

(a) $u = 0.03\text{mm}$, $v = 0\text{mm}$.

(b) $u = 0.03\text{mm}$, $v = 0.01\text{mm}$.

Figure 10-5: Contour plot of normalized second principal stresses $\sigma_2 / \max\{1, \sigma_1\}$ for two different load cases with $a = 50\text{mm}$, $L = 100\text{mm}$.

Note that Figure 10-5 shows σ_2 normalized with respect to $\max\{1, \sigma_1\}$, which is done to be able to distinguish the different states of the membrane: taut, wrinkled or slack. The reason for not normalizing σ_2 with respect to σ_1 directly is to prevent a misleading plot in slacked regions. In these regions both σ_1 and σ_2 are very small, i.e. in the order of magnitude of the penalty parameter μ, which means that their ratio can be anywhere between 0 and 1. To force the contour values in Figure 10-5 to be close to zero in this case normalization with respect to $\max\{1, \sigma_1\}$ is applied. Note that the '1' does not affect the rest of the figure as it is much smaller than the value for σ_1 in taut or wrinkled regions.

Now the state of the membrane can be identified by combining Figures 10-4 and 10-5 as shown in Table 10-1.

State	Exact Characteristics	Approximated Characteristics
Taut	$\sigma_1 > 0$ & $\sigma_2 > 0$	$\sigma_1 > 0.01 \max \sigma_1$ & $\sigma_2 / \max\{1, \sigma_1\} > 0.01$
Wrinkled	$\sigma_1 > 0$ & $\sigma_2 = 0$	$\sigma_1 > 0.01 \max \sigma_1$ & $\sigma_2 / \max\{1, \sigma_1\} < 0.01$
Slack	$\sigma_1 = 0$ & $\sigma_2 = 0$	$\sigma_1 < 0.01 \max \sigma_1$ & $\sigma_2 / \max\{1, \sigma_1\} < 0.01$

Table 10-1: Characteristics of membrane states

From these characteristics it can be seen that almost the complete membrane strip in Figure 10-4 is wrinkled, as predicted by the analytical solution. The approximated characteristics in Table 10-1 are introduced for post-processing purposes. The value of 0.01 was chosen to be some orders larger than the penalty parameter μ, which was done to make the post-processing results better readable. The states of the membrane under the two loading conditions are shown in Figure 10-6 in which the approximated characteristics of Table 10-1 are applied. Note that many existing numerical methods require the membrane states as part of the calculations whereas in the current method these states are purely obtained by post-processing.

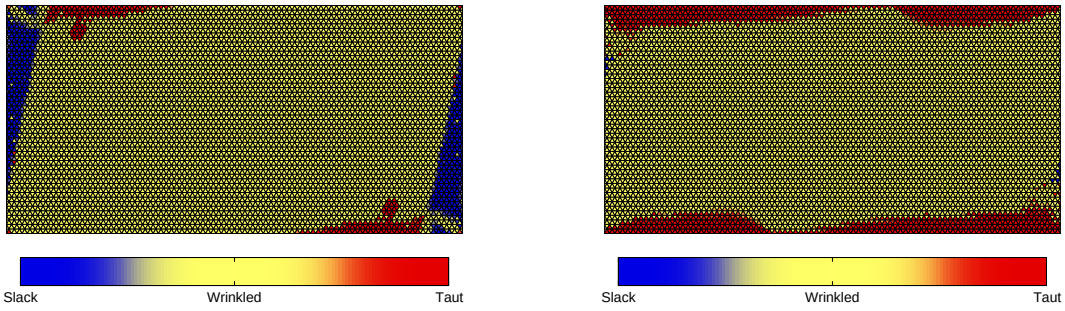

(a) $u = 0.03$mm, $v = 0$mm. **(b)** $u = 0.03$mm, $v = 0.01$mm.

Figure 10-6: States of the membrane under different load cases with $a = 50$mm, $L = 100$mm.

From Figure 10-6 it can be seen that in contrast to the analytical solution, some parts of the membrane strip are either slack or taut. The taut region is a result from the fact that the applied displacements are finite instead of infinitesimal which results in the Poisson's effect. The slack regions are caused by the same as well as by the choice of the 0.01 value in Table 10-1. This value, however, has only a little effect, which means that the approximated membrane state can be safely considered to be the real membrane state.

For the pure shear load case in Figure 10-6a the membrane is slacking near two corners, whereas this slack has disappeared for the load case including tensile displacement in Figure 10-6b. As can be seen from Figure 10-6a, the lower right and upper left corners are approached by a taut region from the horizontal direction and a slack region from the vertical direction. This results in a wrinkled region at these corners. Both figures 10-6a and 10-6b are symmetric across the diagonal because of the symmetry in loading, structure and mesh.

By observation it was shown that the presented results agree with the analytical model, however a more thorough convergence study was required to assess the performance of the numerical model. This was done using the analytical results presented by Mansfield and is presented in Appendix C. The Mansfield solution assumes a linear elastic/ Saint-Venant material, therefore this material law was also used for this convergence analysis. The Poisson's ratio did not appear in the analytical solution because infinitesimal displacements were assumed. In the numerical model this Poisson's ratio was chosen to be $\nu = 0.5$ since this resembles the neo-Hookean material law. For the convergence analysis the error in total strain energy in the membrane is considered:

$$\varepsilon = \frac{\frac{1}{2}\int_{\Omega}(\Delta\boldsymbol{\sigma})^T\boldsymbol{C}^{-1}(\Delta\boldsymbol{\sigma})d\Omega}{\phi_{MF}} \tag{10-1}$$

in which ϕ_{MF} is the total strain energy computed from the Mansfield solution, $\boldsymbol{C}$ is the material stiffness matrix and $\Delta\boldsymbol{\sigma}$ is the difference between the numerical and analytical stresses:

$$\Delta\boldsymbol{\sigma} = \boldsymbol{\sigma}_{num} - \boldsymbol{\sigma}_{MF} \tag{10-2}$$

The integratal in Equation (10-1) is performed by numerical integration using the integration points of the elements. Figure 10-7 consists of several mesh convergence plots for the rectangular membrane, each of which checks different element properties. Note that unless stated otherwise, as in Figure 10-7c, the quad elements are the hybrid elements as presented in Section 8-2-3.

The main observation from Figure 10-7 is that all plots show a convergence behavior. The order of convergence is related to the decrease in error with a decrease in element size h which is proportional to the square root of the number of elements: $h \propto 1/\sqrt{n_e}$. Consequently, a first order convergence $\mathcal{O}(h)$ corresponds to a slope of -0.5 in the convergence plots. This slope is drawn in the figures and can be used to show that the order of convergence for all plots is $\mathcal{O}(h)$. For general FEM methods this order is $\mathcal{O}(h^2)$ if the mesh is perfect, i.e. all squares have same size, and $\mathcal{O}(h)$ otherwise. This means that the order of convergence in Figure 10-7 conforms well with the standard FEM methods.

Note that the errors in Figure 10-7 level off at a value of approximately 10^{-2} whereas the tolerance of the penalty parameter μ is 10^{-6}. This discrepancy is caused amongst others by the fact that in the numerical method the displacements are finite whereas the analytical solution assumes infinitesimal displacements. Another explanation is that the numerical method has difficulties in integration stresses at the corners which are singular in the pure shear load case and close to singular when tensile displacement loading is added. Further, the regions which are close to slacking have very small stiffness in all directions which may cause numerical difficulties in these regions. The final contribution to the cut-off level of the errors are the tensors $\hat{\boldsymbol{S}}$ and $\hat{\boldsymbol{E}}$ which are close to rank-one. Inverting these tensors may yield inaccuracies as pure rank-one tensors are not invertible. Despite these difficulties the results in Figure 10-7 are satisfying because convergence is proven.

From Figure 10-7a it can be seen that for the load case with pure shear deformation the proposed method contains a larger error than for the second load case including tension. This was expected due to the difficulties in the regions close to slacking as explained. The quad elements also showed a smaller error than the tria elements and a smoother convergence curve. The peaks in the convergence curve of triangular elements were caused by non-symmetry in the mesh, which caused a slight increase in the error because the structure and loading were

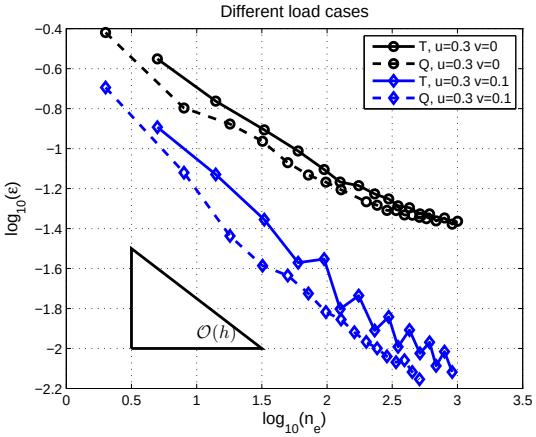

(a) Different load cases.

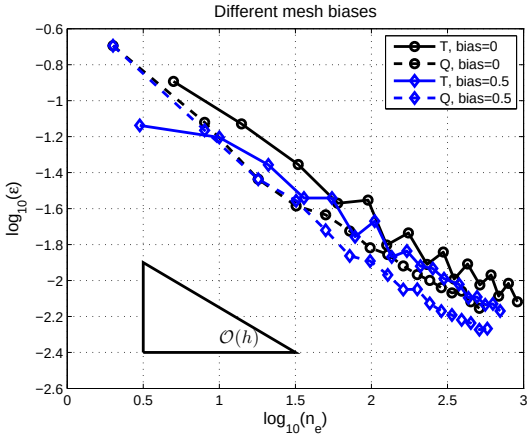

(b) Different mesh biases.

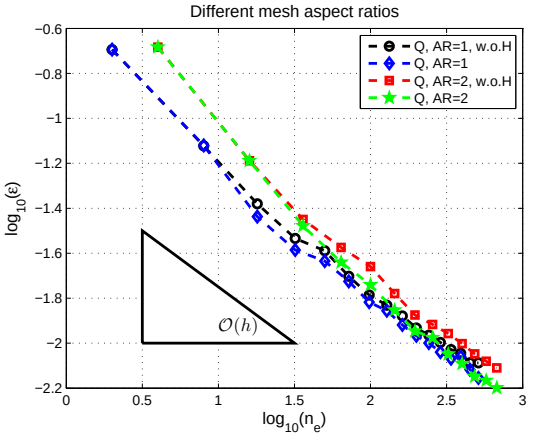

(c) Different quad mesh aspect ratios with or without the hybrid element (w.o.H).

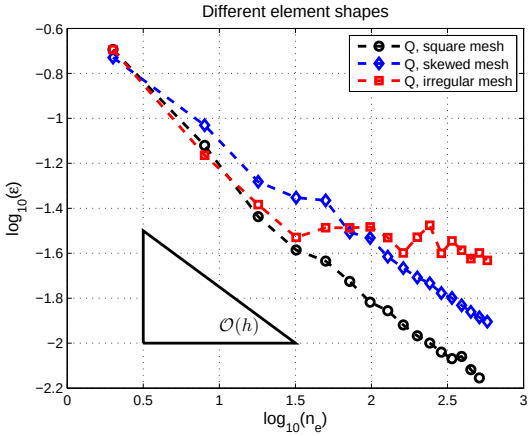

(d) Different element shapes.

Figure 10-7: Mesh convergence for rectangular membrane strip with $a = 50$mm, $L = 100$mm.

symmetric. Applying mesh bias was expected to reduce the total error as explained, which was confirmed, see Figure 10-7b for both type of elements.

The convergence for square (AR=1) and rectangular (AR=2) quad elements and the results for the original quad element, i.e. not the hybrid element are shown in Figure 10-7c. The differences among the curves in this figure were small but behave as expected: the square elements were better than rectangular elements and the hybrid element outperformed the standard quad element.

Finally the convergence for different shapes of the quad elements is shown in Figure 10-7d. As expected the square mesh performs best and the error for the irregular mesh has a higher cut-off level than the other meshes. This is explained by the fact that the irregular mesh contained the worse-conditioned elements which decreased the accuracy of the results.

10-1-2 Isogeometric Analysis

The isoparametric elements performed well in modeling the tension field as they show convergence towards the analytical solution, however these elements also suffered from some deficiencies. This included an inability to model the stress directions accurately in regions close to slacking. In this section it is investigated whether isogeometric analysis leads to better results in general, especially in these difficult regions. The basic principles of isogeometric analysis with finite elements were presented in Chapter 9.

The isogeometric analysis may lead to better results as the derivative of the NURBS basis functions can be forced to be continuous over the membrane. As the stresses are related to this derivative they are consequently forced to be continuous, which may lead to a more accurate modeling of the stress directions in the slacked regions. These directions appeared to experience some randomness in the isoparametric elements as shown in Figure 10-4 which is likely to be prevented by a continuous stress field.

The representation of a rectangular membrane using NURBS basis functions is trivial. The weight of all control points is the same, meaning that the basis function are B-splines effectively. The minimum order of shape functions is $p = 1$, which represents the linear shape functions applied in isoparametric analysis. In fact, choosing $p = 1$ and $k = 0$ is fully equivalent to using rectangular quadrilateral elements. The first principal stresses in the membrane for the same load cases as in Figure 10-4 are shown in Figure 10-8. The basis functions are of second order and the element connectivity is $k = 1$.

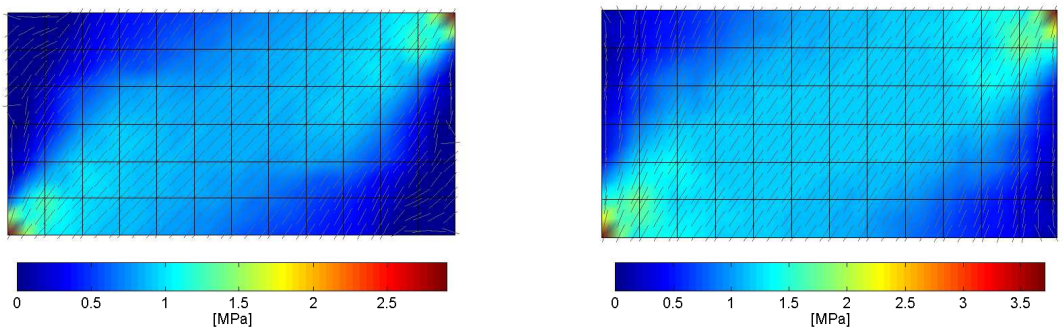

(a) $u = 0.03$mm, $v = 0$mm. **(b)** $u = 0.03$mm, $v = 0.01$mm.

Figure 10-8: Contour plot of first principal stresses σ_1 from isogeometric analysis with $p = 2$ and $k = 1$.

The stresses shown in Figure 10-8 are continuous over the whole membrane. The stress directions in the slacked regions of the membrane were less random than for the isoparametric elements as follows from Figure 10-8a, however the orientation of these stresses was not very accurate when compared to the analytical solution. This may partly be caused by the finite displacement in the numerical model in contrast to the infinitesimal displacements in the analytical model but may also be due to the loss of accuracy of the proposed method in slacked regions. Forcing the stress field to be continuous therefore leads to a less random, but not

necessarily better modeling of the stress directions. Note that increasing k to higher values does not resolve this issue.

To further assess the performance of the NURBS basis functions for the membrane application a convergence study is applied for different values of p and k. The results of this study are presented in Figure 10-9.

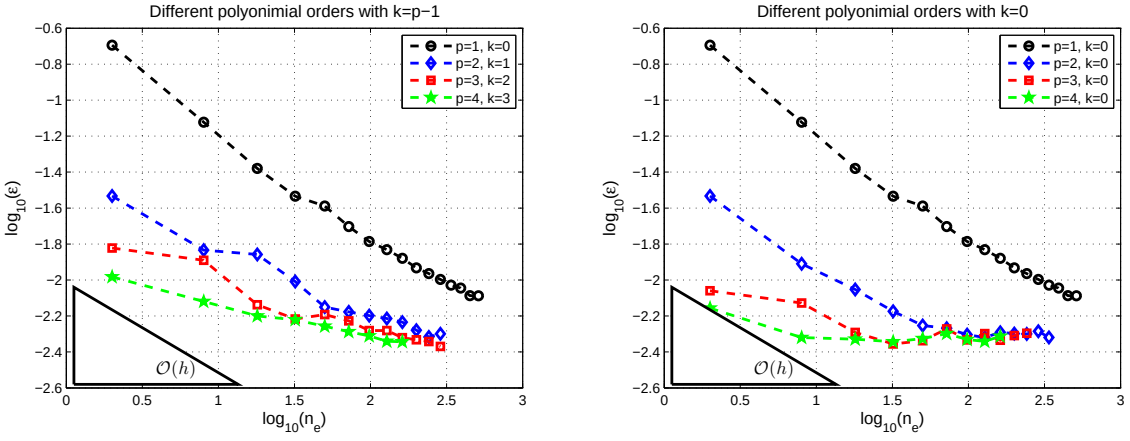

(a) Element connectivity $k = p - 1$ **(b)** Element connectivity $k = 0$

Figure 10-9: Mesh convergence of isogeometric analysis for rectangular membrane strip with $a = 50\text{mm}$, $L = 100\text{mm}$.

The results showed that higher order shape functions yielded lower errors in the results, which was expected as these shape function are able to model more complex geometries and more integration points are used per element. The order of convergence was not affected by the choice of p, which could have been expected based on Chapter 9. For the curves where $p = 3$ or $p = 4$ this can be explained by the cut-off level of the error which was already reached for a very low number of elements, especially in Figure 10-9b. The curves for $p = 2$ require another explanation as their rate of convergence was not limited by the level-off error. Most likely the limited differentiability of the relaxed strain energy function contributes to the $\mathcal{O}(h)$ convergence rate. Indeed, the definition of the relaxation does not guarantee a continuity of the second derivative of this relaxation, which may restrict the rate of convergence of the error. Another explanation may be a lack of accuracy in the representation of the governing equations, which would be caused by e.g. neglecting terms in the derivations which leads to $\mathcal{O}(h)$ convergence of the problem representation. As only second order errors were neglected in deriving the governing equations the latter explanation is unlikely.

10-2 Annular Ring

Haseganu et al. [10] propose a numerical method for membrane wrinkling based on a dynamic relaxation method, which is tested on several load case examples. Three of these examples were also modeled using the proposed element in this section and the two following sections. Haseganu et al. present only the deformed configurations as results, which were used as a visual verification for the results presented in this section. The first example was an annular

membrane ring which was clamped at the outer radius and the displacement was applied at the inner radius.

10-2-1 Isoparametric Analysis

The initial configuration of the annular ring, meshed with triangular and quadrilateral elements, is depicted in Figure 10-10. These meshes are optimized to get the best-conditioned elements, i.e. the tria elements are as close to equilateral triangles as possible and the quad elements approach the square shape. The outer radius of the annular ring is twice the inner radius.

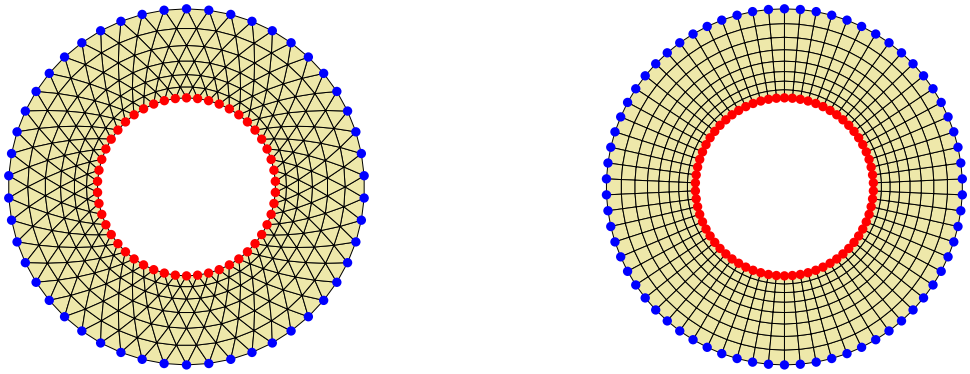

(a) Tria elements **(b)** Quad elements

Figure 10-10: Mesh of annular membrane ring with $R_{out} = 100$mm and $R_{in} = 50$mm.

The applied displacement exerted on the inner circle consists of three parts. First the inner circle is pulled inside by reducing the inner radius by a factor of 2. Then an in-plane twist of 90° is applied after which the inner circle is pulled out normal to the reference configuration by $R_{out} = 100$mm. Note that these three displacements were applied simultaneously in the implementation. The deformed configuration is shown in Figure 10-11 and its colors represent the first and second principal stresses, shown in Figures 10-11a and 10-11b respectively. Note that these stress values were obtained directly from the stress tensor $\boldsymbol{S}$ and therefore they represent the stresses in the reference configuration. This means that the actual stresses are slightly different and Figure 10-11 was only used to make qualitative conclusions about the stresses.

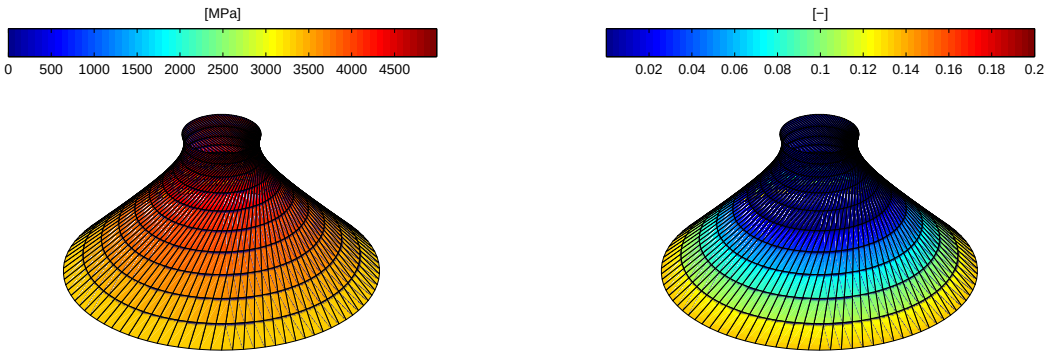

(a) σ_1 [MPa] **(b)** $\sigma_2 / \max\{1, \sigma_1\}$ [-]

Figure 10-11: Deformed configuration of annular ring with first and second principal stresses under axisymmetric loading.

Note that the second principal stresses σ_2, shown in Figure 10-11b, were normalized with respect to $\max\{1, \sigma_1\}$ for the same reason as presented in Section 10-1. The values of σ_1 in Figure 10-11 are relatively high, which is not considered relevant as this example is not meant to represent a realistic load case but it rather serves as a performance study of the proposed method. From the characteristics in Table 10-1 the membrane states are displayed in Figure 10-12.

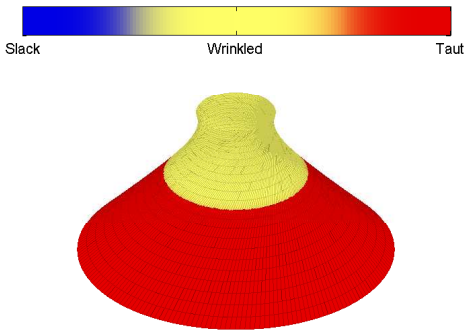

Figure 10-12: States of the annular membrane ring under axisymmetric loading.

From Figure 10-12 it can be observed that the annular membrane is taut near the outer edge of the annular ring and becomes wrinkled approximately halfway towards the inner circle. The membrane does not slack anywhere in the deformed annular ring. All stresses in the membrane are axisymmetric which is caused by the axisymmetry of the structure and the loading.

The deformed configuration of the annular membrane where, in addition to the loading as

before, the inner circle is also translated parallel to the initial configuration by $R_{in} = 50\text{mm}$ is shown in Figure 10-13.

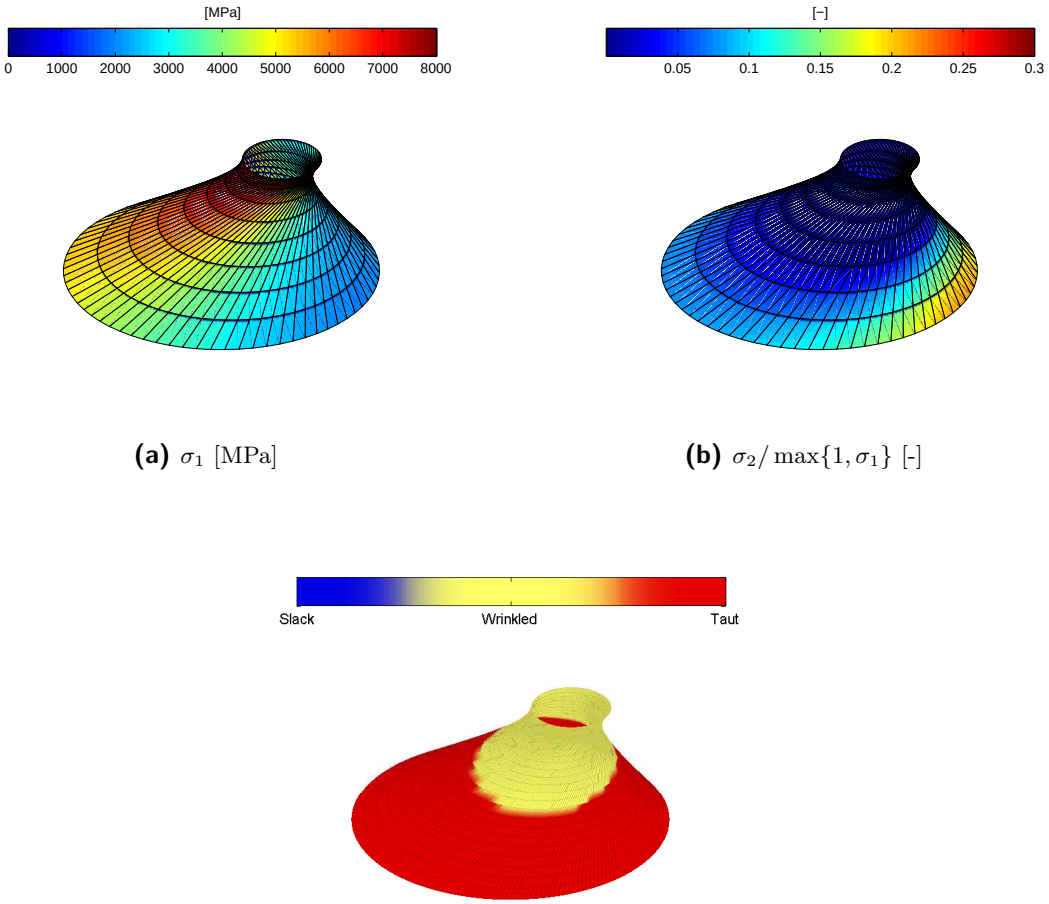

(a) σ_1 [MPa]

(b) $\sigma_2/\max\{1, \sigma_1\}$ [-]

(c) Membrane states

Figure 10-13: Deformed configuration of annular ring with first and second principal stresses under non-symmetric loading.

From Figure 10-13 it can be seen that the wrinkled region of the membrane is larger than for the symmetric load case and no slack occurs in the membrane. The results presented in this section prove the performance of the proposed method with isoparametric finite elements in $\mathbb{R}^3$.

10-2-2 Isogeometric Analysis

To apply the isogeometric analysis to the annular membrane ring, its geometry needs to be represented by the NURBS basis functions. The representation of a quarter circle was considered in Section 9-3. In the current analysis one knot vector represents this circular arc

whereas the other knot vector represents the radial direction of the annular ring from $r = R_{in}$ to $r = R_{out}$.

The geometry of the full circle can be obtained by combining four quarter rings, however, this requires careful considerations at the interfaces. Instead, the axisymmetry of the annular ring and its loading were used in this section, therefore only a quarter ring was needed with corresponding boundary conditions at the symmetry planes. The input mesh for the quarter annular ring is shown in Figure 10-14.

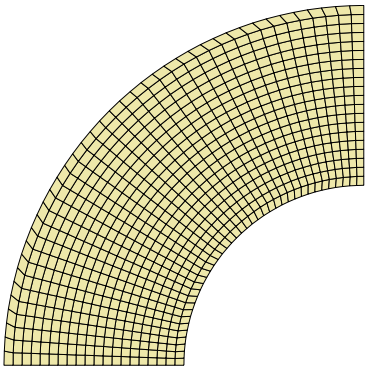

Figure 10-14: Input mesh for isogeometric analysis on quarter annular ring.

The boundary conditions on the two symmetry planes were implemented as multi-point constraints relating the degrees of freedom at the first symmetry plane to those at the second symmetry plane. Note that in Figure 10-14 these symmetry planes are the horizontal and vertical edges of the quarter circle. The applied loading to the quarter circle was the symmetric loading case which was also considered for isoparametric analysis. The first principal stresses are shown in Figure 10-15 for shape functions with polynomial order $p = 2$ and element connectivity $k = 1$.

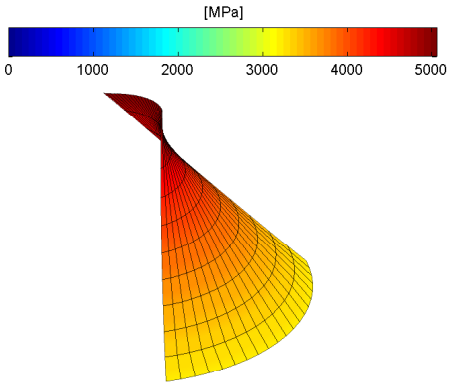

Figure 10-15: Deformed configuration of quarter annular ring with first principal stresses from isogeometric analysis with $p = 2$ and $k = 1$.

From Figure 10-15 it can be seen that the membrane deformation and stress distribution are equivalent to the results obtained from isoparameteric analysis in Figure 10-11. The performance of the NURBS shape functions is therefore confirmed even though a thorough analysis has not been performed in this example as this was presented for the more challenging membrane strip in Section 10-1.

10-3 Annular Square

The annular square membrane which is presented in this section is similar to the annular ring. The difference in membrane geometry is that the circular shapes are replaced by squares. Note that from this section onwards only isoparametric elements are implemented as they simplify the meshing procedure in the programming software MATLAB. The reference configuration of the square membrane, meshed with elements optimized for good conditioning, is shown in Figure 10-16.

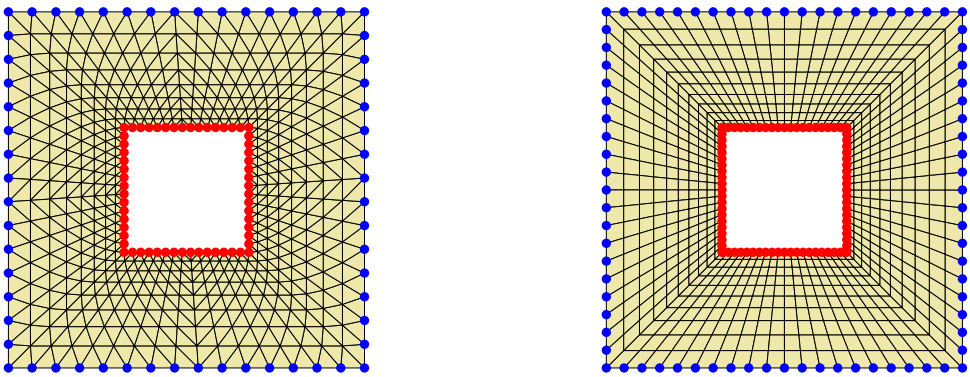

(a) Tria elements **(b)** Quad elements

Figure 10-16: Mesh of annular membrane square with $W_{out} = 50$mm and $W_{in} = 17.5$mm.

The applied displacement to the inner square consists of two parts. First an in-plane twist of 90° was applied after which this square was pulled out normal to the reference configuration by $W/2 = 25$mm. Again, these displacement were applied simultaneously to generate the results. The deformed configuration of the membrane colored with the first and second principal stresses as well as the membrane states according to Table 10-1 is shown in Figure 10-17.

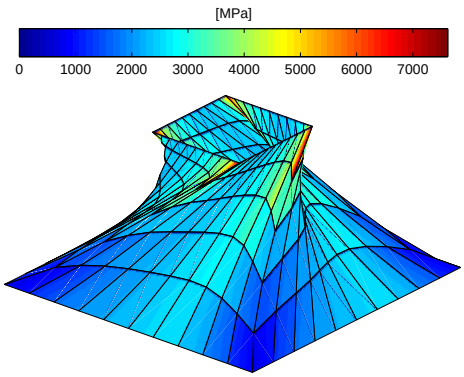

(a) σ_1 [MPa]

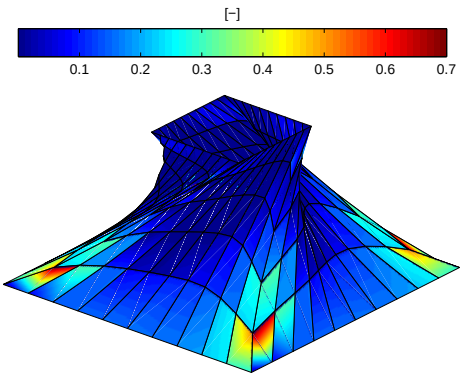

(b) $\sigma_2 / \max\{1, \sigma_1\}$ [-]

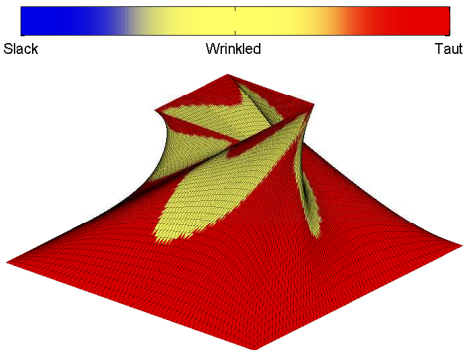

(c) Membrane states

Figure 10-17: Deformed configuration of annular ring with first and second principal stresses.

From Figure 10-17 it can be seen that the extreme values of σ_1 occured near the corners of the inner square. In fact, the stresses were singular at these corners which was found by refinement of the mesh. Looking at Figure 10-17c it was observed that the membrane wrinkles near the inner square and is taut at the outer edges. Slack does not occur in the deformed configuration.

10-4 Sheared Membrane with Hole

The third example from Haseganu et al. [10] which was considered in this section consists of a square membrane with a hole. A severe shear displacement was applied to the membrane to show the effects of extreme slackness on the proposed method. The initial configuration including the mesh which again was optimized to be well-conditioned is shown in Figure 10-18.

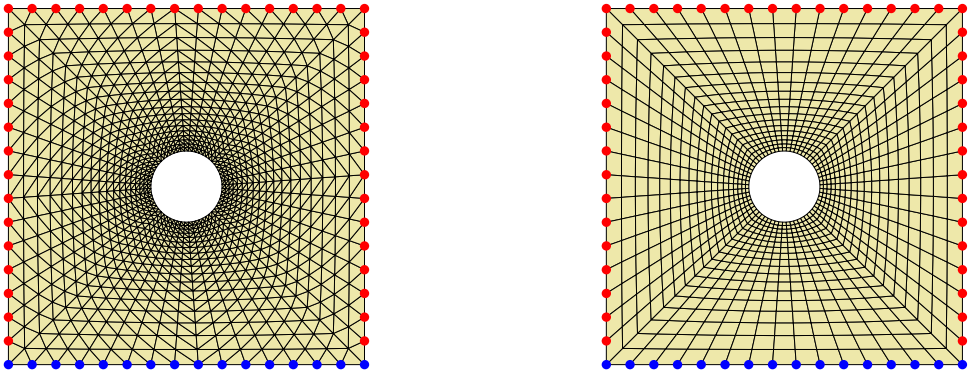

(a) Tria elements **(b)** Quad elements

Figure 10-18: Mesh of square membrane with a hole with $W = 100$mm and $R_{in} = 10$mm.

The applied displacement was a shear deformation on the edges of the membrane with a shear angle of $\gamma = 1/\sqrt{3}$rad$\approx 65^o$. The deformed configuration and stresses are given in Figure 10-19.

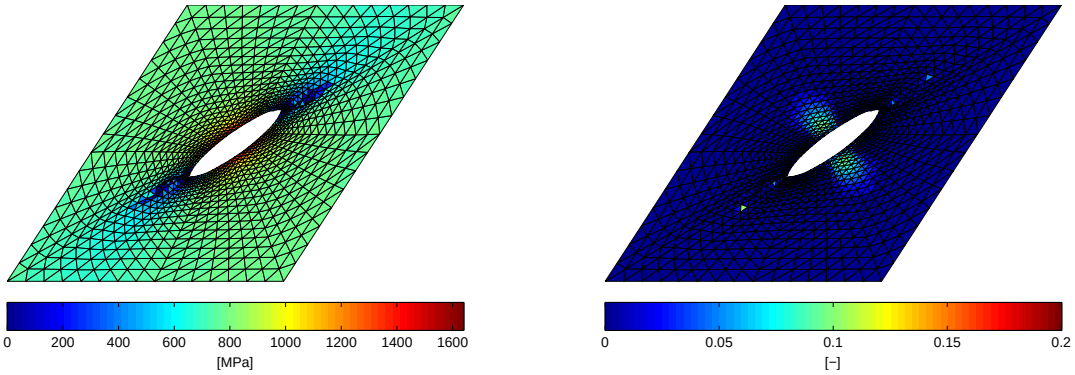

(a) σ_1 [MPa] **(b)** $\sigma_2/\max\{1, \sigma_1\}$ [-]

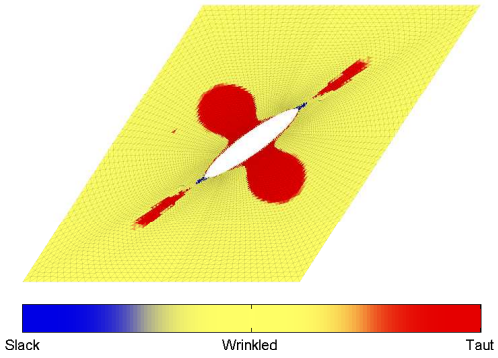

(c) Membrane states

Figure 10-19: Deformed configuration of square membrane with hole with first and second principal stresses under shear deformation with $\gamma = 1/\sqrt{3}$.

From Figure 10-19 it can be seen that all three different membrane states are present in the deformed configuration. The major part of the membrane was wrinkled but near the sharp edges of the deformed hole a slack region occurs and at the long sides of the ellipse the membrane was taut. The detailed deformation of the slack region was obtained from a mesh refinement in this region. Zooming in to this region yielded the σ_1 contours as presented in Figure 10-20. Note that the mesh for this figure was generated using ABAQUS.

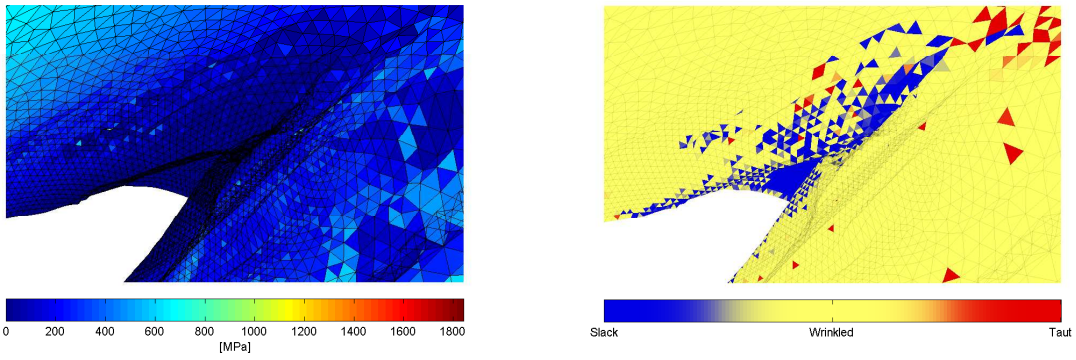

(a) σ_1 [MPa] **(b)** Membrane states

Figure 10-20: First principal stresses and membrane states near the deformed hole.

A severe mesh distortion in the slack region is shown in Figure 10-20, which only occurs for large shear deformation as was the case. This mesh distortion also caused small distortions in the stress field, which resulted in the irregularity in membrane states seen in Figure 10-20b. The distortion is likely to be caused by a combination of different factors. Firstly the effective stiffness of the membrane in the slack region is very small and results in low resistance against displacements. The second factor is the severity of out of plane displacement that would occur

in reality, which is now modeled as an in-plane contraction. When this contraction needs to be much larger than the element size, elements may start to overlap since they cannot accommodate for this large contraction. The combination of these factors may result in the observed mesh distortion, this however was not verified using experiments or other models and thus the explanation is speculative.

This mesh distortion clearly is a limitation of the method, however it does not break down the results in the rest of the membrane as can be seen from Figure 10-19. It should be noted that the results was less stable when using the 3D elements, because the distortion is then able to go in three directions. The out of plane direction was the 'easiest' way to go for the mesh because of the low out of plane stiffness in slacked regions. This may lead to unstable convergence as these out out of plane distortions can become very large and result in numerical instabilities. In the 2D elements the membrane cannot go in this out of plane direction and is therefore more stable. For this reason it is advised to use the 2D elements, if possible, when severe slack regions are expected.

10-5 Pressurized Beam under Bending

Membranes are often applied in inflatable or pressurized structures as they are lightweight and flexible. A simplified model of such a structure is a pressurized membrane beam clamped at one side which is considered in this section and used to validate the proposed method with experimental results. The beam was subjected to a tip displacement which caused it to bend. Pressurizing the beam resulted in tensile stresses over the whole beam whilst the bending load had a compressive effect at one side of the beam. When the compression exceeded the tension induced by the pressure, wrinkling initiated in the compressed side of the membrane beam. This led to a lower resistance of the inflatable beam against the bending load, called softening.

The membrane model in this section attempted to capture the softening by computing the load-deflection curve, which was compared with experimental results to validate the proposed method.

10-5-1 Volume Dependent Pressure Loading

The modeling of volume dependent pressure loading is more complex than modeling dead loads as e.g. gravity. These dead loads are independent of the deformation of the structure, whereas pressure loading depends on the deformation both in magnitude and direction. The magnitude of the pressure loading depends on the volume inside the beam and its direction is normal to the deformed structure. The governing equations for pressure loading are presented in Rumpel [30] and considered here.

The external virtual work done by pressure loading $\delta\Pi_{press}$ is given as:

$$\delta\Pi_{press} = \int_{x^1}\int_{x^2} p\boldsymbol{n}^* \cdot \delta\boldsymbol{u} dx^1 dx^2 \tag{10-3}$$

in which p is the pressure, $\boldsymbol{n}^*$ is the normal vector to the membrane defined as $\boldsymbol{n}^* = \boldsymbol{b}_1 \times \boldsymbol{b}_2$ according to the convention in Section 4-1 and x^1 and x^2 are the coordinates in the current

configuration using this same convention. The variational principle including this pressure contribution then becomes:

$$\delta\Pi_{struct} + \delta\Pi_{press} = 0 \tag{10-4}$$

with $\delta\Pi_{struct}$ the variation of potential energy of the membrane structure as in Equation (5-21). The pressure p is determined by the Poisson's law as function of the enclosed volume V:

$$p_0 V_0^{\kappa} = pV^{\kappa} \tag{10-5}$$

with p_0 and V_0 being the pressure and enclosed volume in the reference configuration and κ is the isentropy constant which takes the value $\kappa = 1.4$ in air. The enclosed volume V is computed as:

$$V = \frac{1}{3}\int_{x^1}\int_{x^2} \boldsymbol{r}\cdot\boldsymbol{n}^* dx^1 dx^2 \tag{10-6}$$

with $\boldsymbol{r}$ is the position vector in the current configuration. Linearization of the Poisson's law yields:

$$\Delta p + \frac{\kappa p}{V}\Delta V = 0 \tag{10-7}$$

Rumpel [30] shows that the implementation of Equations (10-4) and (10-7) into the known finite element expressions results in the governing Equation (10-8) for the nodal displacements update $\Delta\boldsymbol{v}$. Note that this equation holds for closed volume structures only:

$$\left(\boldsymbol{K}_{struct} - \boldsymbol{K}_{press} + \gamma\boldsymbol{d}\otimes\boldsymbol{d}\right)\Delta\boldsymbol{v} = \boldsymbol{R}_{struct} + \boldsymbol{f}_{press} \tag{10-8}$$

$\boldsymbol{K}_{struct}$ and $\boldsymbol{R}_{struct}$ are the stiffness matrix and residual force vector of the structure alone, which are obtained by summation over all elements of the corresponding expressions in Equation (5-45) and (5-46) respectively. The pressure dependent parameters in Equation (10-8) are given as:

$$\boldsymbol{K}_{press} = \frac{p}{2}\sum_{elem}\int_{x^1}\int_{x^2}\begin{pmatrix}\boldsymbol{N}\\ \boldsymbol{N}_{,1}\\ \boldsymbol{N}_{,2}\end{pmatrix}^T\begin{bmatrix}\boldsymbol{0} & \boldsymbol{W}^{(1)} & \boldsymbol{W}^{(2)}\\ \boldsymbol{W}^{(1)^T} & \boldsymbol{0} & \boldsymbol{0}\\ \boldsymbol{W}^{(2)^T} & \boldsymbol{0} & \boldsymbol{0}\end{bmatrix}\begin{pmatrix}\boldsymbol{N}\\ \boldsymbol{N}_{,1}\\ \boldsymbol{N}_{,2}\end{pmatrix} dx^1 dx^2 \tag{10-9}$$

$$\gamma = \kappa\frac{p}{v} \tag{10-10}$$

$$\boldsymbol{d} = \sum_{elem}\int_{x^1}\int_{x^2}\boldsymbol{N}^T\boldsymbol{n}^* dx^1 dx^2 \tag{10-11}$$

$$\boldsymbol{f}_{press} = p\sum_{elem}\int_{x^1}\int_{x^2}\boldsymbol{N}^T\boldsymbol{n}^* dx^1 dx^2 \tag{10-12}$$

in which $\boldsymbol{N}$, $\boldsymbol{N}_{,1}$ and $\boldsymbol{N}_{,2}$ are the shape function matrix and its derivative as presented in Section 5-5-1 in general and in Chapters 7, 8 and 9 for the triangular, quadrilateral and isogeometric elements respectively, also:

$$\boldsymbol{W}^{(1)} = \boldsymbol{n}^*\otimes\boldsymbol{b}^1 - \boldsymbol{b}^1\otimes\boldsymbol{n}^* \tag{10-13a}$$

$$\boldsymbol{W}^{(2)} = \boldsymbol{n}^*\otimes\boldsymbol{b}^2 - \boldsymbol{b}^2\otimes\boldsymbol{n}^* \tag{10-13b}$$

in which $\boldsymbol{b}^1$ and $\boldsymbol{b}^2$ are the contravariant basis vectors in the current configuration which are obtained from the covariant basis vectors as:

$$\boldsymbol{b}^1 = \frac{1}{\boldsymbol{n}^* \cdot \boldsymbol{n}^*} (\boldsymbol{b}_2 \times \boldsymbol{n}^*) \tag{10-14a}$$

$$\boldsymbol{b}^2 = \frac{1}{\boldsymbol{n}^* \cdot \boldsymbol{n}^*} (\boldsymbol{n}^* \times \boldsymbol{b}_1) \tag{10-14b}$$

In Equation (10-8) only $\boldsymbol{K}_{struct}$ and $\boldsymbol{K}_{press}$ are sparse matrices, whereas the tensor product $\boldsymbol{d} \otimes \boldsymbol{d}$ is not. Therefore it is not efficient to solve this equation by inverting the whole expression which multiplies $\Delta \boldsymbol{v}$, but instead the Shermain-Morrison procedure [42] is applied. For this, let:

$$\boldsymbol{K}^* = \boldsymbol{K}_{struct} - \boldsymbol{K}_{press} \tag{10-15a}$$

$$\boldsymbol{f}^* = \boldsymbol{R}_{struct} + \boldsymbol{f}_{press} \tag{10-15b}$$

in which $\boldsymbol{K}^*$ is a sparse matrix, which can be inverted relatively easily. Define $\Delta \boldsymbol{v}_I$ and $\Delta \boldsymbol{v}_{II}$ as:

$$\Delta \boldsymbol{v}_I = \boldsymbol{K}^{*-1} \boldsymbol{f}^* \tag{10-16a}$$

$$\Delta \boldsymbol{v}_{II} = \boldsymbol{K}^{*-1} \boldsymbol{d} \tag{10-16b}$$

According to the Sherman-Morrison procedure the solution for $\Delta \boldsymbol{v}$ then becomes as:

$$\Delta \boldsymbol{v} = \Delta \boldsymbol{v}_I - \frac{\gamma \Delta \boldsymbol{v}_{II} \cdot \boldsymbol{f}^*}{1 + b\boldsymbol{d} \cdot \Delta \boldsymbol{v}_{II}} \Delta \boldsymbol{v}_{II} \tag{10-17}$$

10-5-2 Beam Model Description

The pressurized beam to be modeled is cylindrically shaped and clamped at the root. The end cap at the tip of the beam is modeled as a rigid part. A sketch of the beam is shown in Figure 10-21.

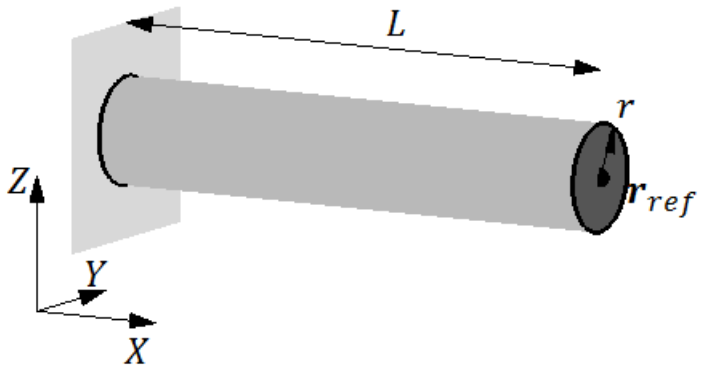

Figure 10-21: Sketch of beam model

The length of the beam is $L = 1000$mm and its radius $r = 50$mm. The position vector $\boldsymbol{r}_{ref}$ represents the reference point of the end cap and is located at its center. The six degrees

of freedom (DOF) of the rigid cap are applied in this reference point directly. These DOF consist of three translations and three rotations and are collected in the vector $\boldsymbol{v}_D$ as shown in Equation (10-18):

$$\boldsymbol{v}_D = \begin{pmatrix} v_{r,X} & v_{r,Y} & v_{r,Z} & \theta & \phi & \psi \end{pmatrix}^T = \begin{pmatrix} \boldsymbol{v}_r \\ \boldsymbol{\theta}_r \end{pmatrix} \tag{10-18}$$

The rotation angles θ, ϕ and ψ are applied in this order and represent rotation around the Z, Y and X axes respectively. For each node within the rigid end cap, the displacement vector is fully determined by these six rigid body DOF. The displacement vector $\boldsymbol{v}_k$ for node k within this end cap is given as:

$$\boldsymbol{v}_k = \boldsymbol{T}\tilde{\boldsymbol{r}}_k + \boldsymbol{v}_r \tag{10-19}$$

in which $\boldsymbol{T}$ is the rotation matrix, $\tilde{\boldsymbol{r}}_k$ is the position of node k relative to $\boldsymbol{r}_{ref}$ in the reference configuration and $\boldsymbol{v}_r$ is the translation of the reference point. The rotation matrix $\boldsymbol{T}$ is composed of the rotation matrices of the three rotation angles as shown in Equation (10-20b):

$$\tilde{\boldsymbol{r}}_k = \boldsymbol{r}_{0,k} - \boldsymbol{r}_{ref} \tag{10-20a}$$

$$\boldsymbol{T} = \boldsymbol{T}_\psi \boldsymbol{T}_\phi \boldsymbol{T}_\theta - \boldsymbol{I} = \begin{bmatrix} 1 & 0 & 0 \\ 0 & c_\psi & -s_\psi \\ 0 & s_\psi & c_\psi \end{bmatrix} \begin{bmatrix} c_\phi & 0 & s_\phi \\ 0 & 1 & 0 \\ -s_\phi & 0 & c_\phi \end{bmatrix} \begin{bmatrix} c_\theta & -s_\theta & 0 \\ s_\theta & c_\theta & 0 \\ 1 & 0 & 0 \end{bmatrix} - \boldsymbol{I} \tag{10-20b}$$

in which $s_\phi = \sin\phi$ and $c_\phi = \cos\phi$. Equation (10-19) needs to be implemented into the numerical model as a constraint on the displacement of all nodes within the rigid end cap. This constraint reduces the number of DOF within this end cap from the displacement unknowns at all nodes to only the six rigid DOF.

Suppose that all nodes in the finite element model are divided into three sets. The first set contains all nodes inside the clamped region at the wall, set two contains the free nodes and the final set contains the nodes inside the rigid end cap. Let n_3 be the number of nodes in this last set and $\boldsymbol{v}_3$ the nodal displacement vector related to these nodes, which is a part of the complete nodal displacement vector. In this case $\boldsymbol{v}_3$ is completely determined by the six rigid DOF as shown in Equation (10-21), which also shows the size of all entries:

$$\underbrace{\boldsymbol{v}_3}_{[3n_3\times 1]} = \underbrace{\begin{bmatrix} \boldsymbol{T} & & \boldsymbol{0} \\ & \boldsymbol{T} & \\ & \ddots & \\ \boldsymbol{0} & & \boldsymbol{T} \end{bmatrix}}_{=\tilde{\boldsymbol{T}}\ [3n_3\times 3n_3]} \underbrace{\begin{pmatrix} \tilde{\boldsymbol{r}}_1 \\ \tilde{\boldsymbol{r}}_2 \\ \vdots \\ \tilde{\boldsymbol{r}}_{n_3} \end{pmatrix}}_{=\tilde{\boldsymbol{R}}\ [3n_3\times 1]} + \underbrace{\begin{bmatrix} \boldsymbol{I} \\ \boldsymbol{I} \\ \vdots \\ \boldsymbol{I} \end{bmatrix}}_{=\tilde{\boldsymbol{I}}\ [3n_3\times 3]} \underbrace{\boldsymbol{v}_r}_{[3\times 1]} = \tilde{\boldsymbol{T}}\tilde{\boldsymbol{R}} + \tilde{\boldsymbol{I}}\boldsymbol{v}_r \tag{10-21}$$

Note that with this equation the number of DOF within the rigid end cap is reduced from $3n_3$ unknown displacement at n_3 nodes to the 6 rigid DOF. Linearizing Equation (10-21) with respect to these rigid DOF results in the relation between $\Delta\boldsymbol{v}_3$ and $\Delta\boldsymbol{v}_D$:

$$\Delta\boldsymbol{v}_3 = \begin{bmatrix} \tilde{\boldsymbol{I}} & \frac{\partial\tilde{\boldsymbol{T}}}{\partial\theta}\tilde{\boldsymbol{R}} & \frac{\partial\tilde{\boldsymbol{T}}}{\partial\phi}\tilde{\boldsymbol{R}} & \frac{\partial\tilde{\boldsymbol{T}}}{\partial\psi}\tilde{\boldsymbol{R}} \end{bmatrix} \begin{pmatrix} \Delta\boldsymbol{v}_r \\ \Delta\boldsymbol{\theta}_r \end{pmatrix} = \boldsymbol{M}\Delta\boldsymbol{v}_D \tag{10-22}$$

in which $\boldsymbol{M}$ is a $3n_3 \times 6$ matrix. With this expression the discretized equations are to be modified. For this purpose, suppose that the discretized system of equations developed in

previous chapters and including the pressure loading is written as $\boldsymbol{K}\Delta\boldsymbol{v} = \boldsymbol{f}$. With the division of the nodes into the three different sets as stated above, this can be written as:

$$\begin{bmatrix} \boldsymbol{K}_{11} & \boldsymbol{K}_{12} & \boldsymbol{K}_{13} \\ \boldsymbol{K}_{12}^T & \boldsymbol{K}_{22} & \boldsymbol{K}_{23} \\ \boldsymbol{K}_{13}^T & \boldsymbol{K}_{23}^T & \boldsymbol{K}_{33} \end{bmatrix} \begin{pmatrix} \Delta\boldsymbol{v}_1 \\ \Delta\boldsymbol{v}_2 \\ \Delta\boldsymbol{v}_3 \end{pmatrix} = \begin{pmatrix} \boldsymbol{f}_1 \\ \boldsymbol{f}_2 \\ \boldsymbol{f}_3 \end{pmatrix} \tag{10-23}$$

in which $\Delta\boldsymbol{v}_1 = \boldsymbol{0}$ because it represents the clamped set of nodes, which means that the total number of unknowns is $3n_2 + 3n_3$ with n_2 and n_3 the number of nodes in sets two and three respectively. By applying Equation (10-22) this set of equations can be rewritten to become:

$$\begin{bmatrix} \boldsymbol{K}_{11} & \boldsymbol{K}_{12} & \boldsymbol{K}_{13}\boldsymbol{M} \\ \boldsymbol{K}_{12}^T & \boldsymbol{K}_{22} & \boldsymbol{K}_{23}\boldsymbol{M} \\ (\boldsymbol{K}_{13}\boldsymbol{M})^T & (\boldsymbol{K}_{23}\boldsymbol{M})^T & \boldsymbol{M}^T\boldsymbol{K}_{33}\boldsymbol{M} \end{bmatrix} \begin{pmatrix} \Delta\boldsymbol{v}_1 \\ \Delta\boldsymbol{v}_2 \\ \Delta\boldsymbol{v}_D \end{pmatrix} = \begin{pmatrix} \boldsymbol{f}_1 \\ \boldsymbol{f}_2 \\ \boldsymbol{M}^T\boldsymbol{f}_3 \end{pmatrix} \tag{10-24}$$

in which the total number of unknowns is equal to $3n_2 + 6$. Solving this equation for $\Delta\boldsymbol{v}_D$ yields the updated $\boldsymbol{v}_D$ which is then substituted into Equation (10-21) to obtain $\boldsymbol{v}_3$. Note that the beam bending is displacement controlled by prescribing one or more entries in $\boldsymbol{v}_D$.

10-5-3 Numerical Results

The numerical results for the pressurized beam under tip loading were compared with experimental data performed by Veldman [36], therefore it was important to have the same dimensions and material properties as those applied during Veldman's experiments. The applied material used is PolyPhenyleneSulphide (PPS) which has a stiffness modulus $E = 2850$MPa and a Poisson's ratio between $\nu = 0.347$ and $\nu = 0.351$. Modeling this material as a linear elastic Saint-Venant material or a neo-Hookean material makes a difference of less than 0.1% in the linear load-deflection regime and less than 1% in the non-linear, softening regime. This means that for validation purposes both material models are equivalent and because the neo-Hookean material is slightly more stable numerically, this was the material model applied in this section.

First the cylindrical beam was only pressurized to check the performance of the pressure contribution presented in Subsection 10-5-1. The input mesh and deformed configuration under pure pressure loading is shown in Figure 10-22.



(a) Reference configuration.

(b) Deformed configuration under pure prssure loading of $p = 2.5$MPa.

Figure 10-22: Mesh of membrane beam with $L = 1000$mm, $r = 50$mm and $t = 0.06$mm.

In Figure 10-22 the red dots represent the nodes inside the rigid end cap of the beam. The deformed configuration as a result of 'blowing up' the beam using a high internal pressure and clamping the rigid end cap is shown in Figure 10-22b.

The first and second principal stresses for the same beam with a lower internal pressure are presented in Figure 10-23.

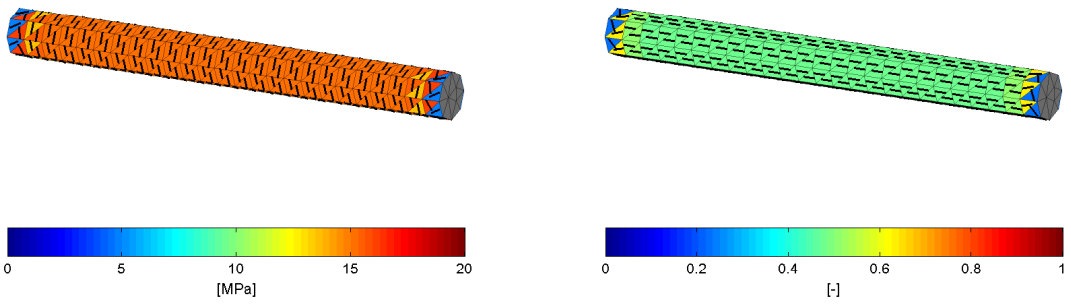

(a) σ_1 [MPa]

(b) $\sigma_2 / \max\{1, \sigma_1\}$ [-]

Figure 10-23: First and second principal stresses of cylindrical beam under pure pressure loading with $p = 0.02$MPa.

From Figure 10-23 it can be seen that both the first and second principal stresses are greater than zero, meaning that the whole membrane beam is taut as expected. The hoop stress in longitudinal direction is predicted by the analytical expression for infinitesimal pressures:

$$\frac{pr}{t} = \frac{0.02 \cdot 50}{0.06} = 16.7\text{MPa}$$

The stresses in Figure 10-23a differed approximately 4% from this analytical value of 16.7MPa caused by the finite internal pressure which results in a volume increase and thus a pressure drop inside the beam. From Figure 10-23b it can be seen that the second principal stresses σ_2 in the membrane are half the value of σ_1 which is in accordance with the analtyical prediction, meaning that the performance of the pressure contribution is confirmed.

Next a bending displacement was applied to the beam by applying a displacement in the vertical direction on the rigid end cap, whilst keeping its other DOF unconstrained as is done in the Veldman's experiments [36]. The stresses in the membrane caused by an internal pressure of 0.02MPa and a tip deflection of 100mm are shown in Figure 10-24.

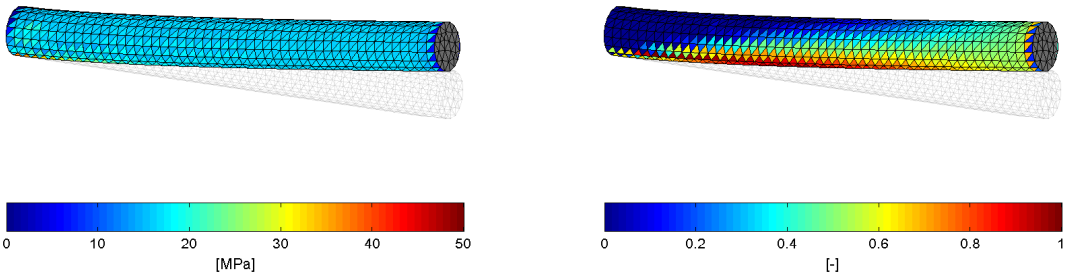

(a) σ_1 [MPa] **(b)** $\sigma_2 / \max\{1, \sigma_1\}$ [-]

Figure 10-24: First and second principal stresses of cylindrical beam with $p = 0.02$MPa and a tip deflection of 100mm.

From Figure 10-24 it can be seen that the first principal stresses were positive along the whole membrane beam and the second principal stresses were equal to zero at the top side of the beam. This means that the beam was wrinkled at this compressed side of the beam and taut elsewhere. When applying multiple load steps in the simulation the pulling force at the tip of the beam is obtained as a function of the tip displacement. This load-deflection curve was generated for different internal pressures and is shown in Figure 10-25.

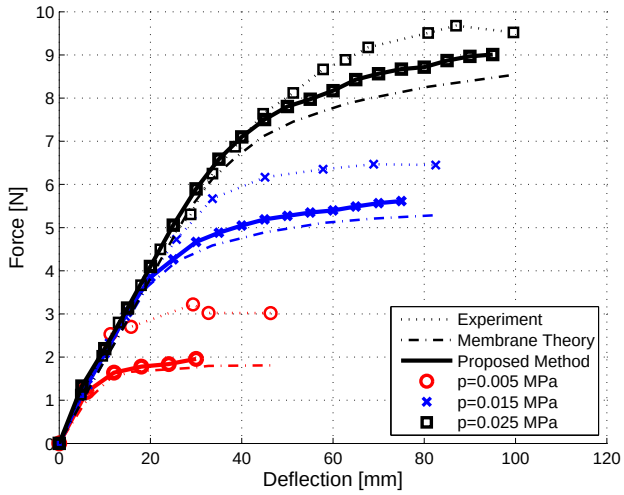

Figure 10-25: Load deflection curves for cylindrical pressurized membrane beam under bending used for validation of numerical results with experimental data. The beam has $L = 1000$mm, $r = 50$mm and $t = 0.06$mm.

From Figure 10-25 it can be observed that the membrane beam displays softening behavior as expected, meaning that for larger tip deflections it became easier to deflect the tip one unit of length more. The softening was caused by the wrinkling of the compressed side of the beam, which is why the curves in Figure 10-25 were initially linear before wrinkling occured. The load at which softening occured increased for increasing internal pressures, which was explained by the larger tensile stresses preventing wrinkles from developing. It should be noted that for all internal pressures the linear regimes have the same slope in Figure 10-25, which indicates that the air inside the beam did not influence the beams 'bending stiffness'.

The load-displacement curves obtained from experiments and membrane theory which are obtained from Veldman [36] and its references are also shown in Figure 10-25. It can be seen that the numerical results agreed very well with experiments and theory in the linear part of the curves. After wrinkling initiated it matched the experimental data better than the theory did, but still underestimated the required pulling force. This was caused by the main assumption of tension field theory, which is that the membrane has zero bending stiffness. In reality the membranes has some bending stiffness and post-buckling stiffness, which means it is able to resists compressive load slightly. A consequence of the zero-bending stiffness assumption is therefore that softening occurs too early and in the softening regime the structural stiffness of the beam is lower in the numerical results than in the experiments.

Next to the cylindrical beam, Veldman [36] has alos done experiments on a tapered pressurized beam which he modeled using standard finite elements. In Veldman's experiments, the membrane material is PPS as for the cylindrical beam, the root radius is $r_{root} = 56.8$mm, the taper ratio $r_{tip}/r_{root} = 0.5$ and the skin thickness is increased to $t = 0.0703$mm. An internal pressure of $p = 0.02$MPa is applied after which the tip is deflected by 100mm. The resulting principal stresses as computed using the proposed element are shown in Figure 10-26.

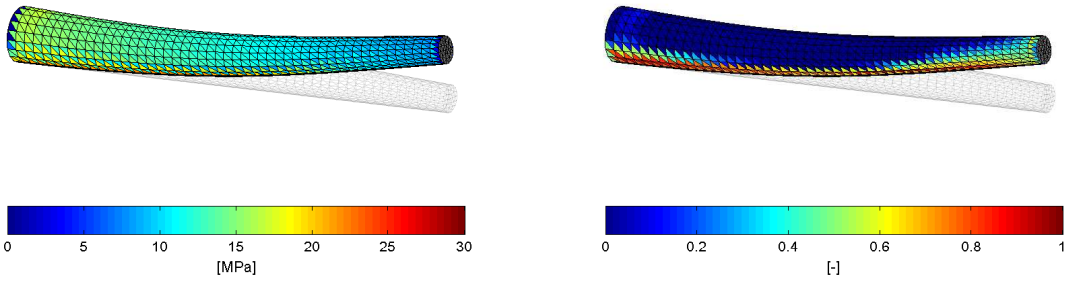

(a) σ_1 [MPa] **(b)** $\sigma_2/\max\{1,\sigma_1\}$ [-]

Figure 10-26: First and second principal stresses of tapered beam with $p = 0.02$MPa and a tip deflection of 100mm.

From Figure 10-26 it can be seen that the wrinkled region for this tapered cylinder was larger than for the cylindrical beam in Figure 10-24. This is explained by the smaller radii of the tapered beam which result in lower tensile stresses during pressure loading, meaning that wrinkling occurs at a lower applied loading. The proposed method is compared with a standard shell element method [36] in Figure 10-27.

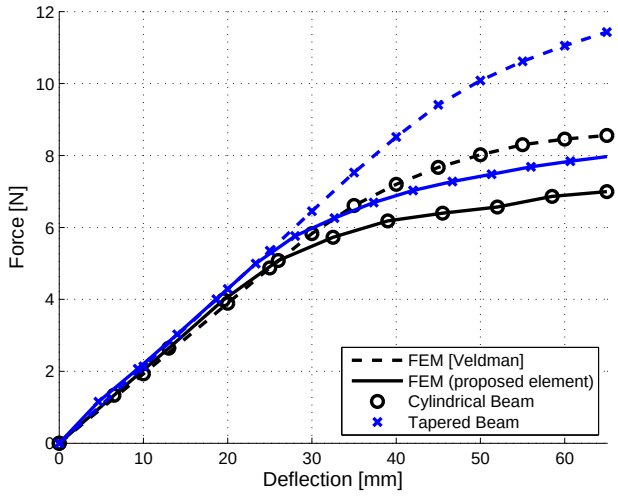

Figure 10-27: Load deflection curves for pressurized membrane beam under bending with $p = 0.02$MPa. The cylindrical beam has $L = 1000$mm, $r = 50$mm and $t = 0.06$mm and the tapered beam has $L = 1000$mm, $r_{root} = 56.8$mm and $t = 0.0703$mm.

The results in Figure 10-27 show similar behavior to that shown in Figure 10-25, i.e. the linear part of the load-deflection curve is modeled correctly whereas the non-linear part is too flexible. It is observed that the mismatch for the tapered beam is larger than for the

cylindrical beam. This mismatch is caused by a too early initiation of softening and a lower slope during softening. The former indicates that in reality the membrane had a larger resistance against compression and the latter shows that in reality the membrane had a large post-buckling stiffness.

Combining the results shown in Figures 10-25 and 10-27 it can be stated that the proposed element models the linear part of the load-deflection curve very accurately and loses some of this accuracy in the softening regime.

Chapter 11

Conclusions and Recommendations

11-1 Conclusions

In many engineering applications load carrying membranes are used to provide strength and structural stiffness. Despite many advantages such as high flexibility and a low mass to surface ratio, these membrane are only capable of carrying tensile loads. Any compressive loads immediately lead to wrinkling of the membrane which affects its load carrying capabilities. The tension field theory method provides the governing equations to model these load carrying capabilities with the presence of wrinkles. In this method the wrinkles are modeled as an continuous in-plane contraction of the membrane, which allows the mesh in e.g. a finite element model to be larger than the individual wrinkles. The exact geometry of the wrinkles is lost by this method, but the reduction in computational cost is significant.

The tension field theory method is implemented into the existing theory of finite deformations using a relaxed strain energy function by Pipkin [25, 24]. This relaxation results in a quasi-convex strain energy as function of the deformation gradient which is required to have a stable minimization of total potential energy in the membrane. In this thesis it is investigated whether a variational formulation of the relaxed strain energy function can be used to obtain a robust and efficient method to model the stress distribution in membranes with the presence of wrinkles.

The relaxation of the strain energy function leads to its required quasi-convexity with respect to the deformation gradient based on general convexity properties. Quasi-convexity is a type of convexity which is weaker than convexity but stronger than rank-one convexity. The sufficient conditions for the required quasi-convexity were shown in Chapter 3 to be a convex and non-decreasing strain energy function as a function of the strain tensor, whereas the necessary condition was a non-decreasing strain energy function. By assuming the strain energy function to be convex with respect to the strain tensor, the lower, convex and non-decreasing envelope of the strain energy function exactly led to the required quasi-convexity. This envelope was referred to as the relaxed strain energy function. The expression to obtain this relaxation from the strain energy function was presented in Section 3-4 and it was proven

to be the lower, convex and non-decreasing envelope of the strain energy function. The convexity assumption on the strain energy allowed all material laws for which the stress-strain relation is one-to-one to be applied, which ensured the robustness of the method.

The definition of the relaxed strain energy function was a constrained optimization problem in itself. The constraint specified that the second Piola-Kirchhoff stress tensor needs to be semi-positive definite, which is also specified by Pipkin [25]. Solving a constrained optimization problem is inherently more difficult than an unconstrained problem, which encouraged us to replace the constraint by adding a barrier function. This function approached zero when the constraint was satisfied and infinity elsewhere. The barrier function contains a penalty parameter which goes zero in the limit and represents the extent to which the solution is influenced by the barrier function.

Minimization of the total potential energy in the membrane was performed unsing the variational principle and the relaxed strain energy function and is discussed in Chapter 5. This resulted in three governing equations which uniquely described the membrane deformation and the wrinkling strains and stresses. The three different states of membrane, taut, wrinkled and slack, were implicitly captured in these equations. Consequently, no $if-else$ statements were required to distinguish between the membrane states, which increased the implementation efficiency of the equations. As the governing equations were non-linear and could not be solved analytically they were linearized and the membrane structure was discretized into finite elements. The resulting system of equations contained wrinkling stress and strain updates for every integration point in the finite element model, and a stiffness matrix and residual force vector to determine the displacements of the membrane. The latter makes the method suitable for implementation in a commercial FEM software package. The convexity properties of the relaxed strain energy function guaranteed that solving the linearized governing equations in an iterative procedure leads to the global minimum of the total potential energy function, which ensures the efficiency of the method.

The numerical implementation of the governing equations was based on the interior point method which yielded an efficient algorithm for the updates for wrinkling strains and stresses as presented in Chapter 6. The penalty parameter of the barrier function was also efficiently driven to zero by this method using a predictor-corrector update. To start up the numerical algorithm the wrinkling stresses and strains were initialized in the feasible region based on the stresses computed as if the membrane was a regular shell.

Verification of the proposed method was performed using a rectangular membrane strip under shear and tension loading, see Section 10-1. The resulting stress distribution was relatively complex as it contained singular stresses in two corners and slacking of the membrane in the other corners. An analytical solution of this stress distribution is presented in Mansfield [14] and used to assess the convergence of the proposed method. Convergence of the numerical results to the Mansfield solution with a rate of $\mathcal{O}(h)$ was proven, and is shown in Figure 10-7 considering the energy norm of the error. This error had a cut-off level at approximately 0.5%, which was relatively high given the tolerance on the penalty parameter of 10^{-6}. This cut-off level was attributed to the invertibility of the wrinkling strain tensor which was almost rank-one. As rank-one tensors are not invertible, the small disturbance to the wrinkling strain tensor caused by the barrier function had a noticeable effect on the inverse of this tensor. Additionaly, the stress directions in the slack regions were challenging to model accurately, which contributed to the observed cut-off level of the energy norm. The application of isogeometric analysis ensured continuity of the stress distribution, but also

yielded inaccuracies in the stress directions of the slack regions. Despite these issues the proposed method was verified to accurately model the stress distribution in a membrane with the presence of wrinkles for low computational costs.

The performance of the method in three dimensions was established by modeling in plane twisting and out of plane displacement of two annular membrane structures, see Sections 10-2 and 10-3. A qualitative verification was performed on the deformation of the membrane. Severe slacking of the membrane was considered by extensive shearing of a rectangular plate with a hole as discussed Section 10-4. In the slack regions applied shear distorted the mesh slightly due to the low effective membrane stiffness and severity of the slack. This distortion did not affect the wrinkled and taut regions of the model, which displayed the robustness of the method.

Validation of the method was achieved by consideration of an inflatable beam under bending load, see Section 10-5. Wrinkling occurred at one side of the beam when the compression due to bending exceeded the tension due to internal pressure. As a result the resistance of the beam against the bending load softened which was captured in a load-displacement curve. This softening was shown to depend on the internal pressure as a high pressure delayed the onset of wrinkles in the membrane. A comparison between experimental data and numerical results showed a perfect agreement of the load-displacement curve before softening occurred. In reality the beam softened at higher loads than predicted, which was explained by the assumption of zero bending stiffness of the membrane. In the presence of wrinkles the experiments showed a slightly more stiff behavior than the numerical results due to the non-zero post-buckling stiffness of the actual beam. These discrepancies with experimental data were shown to be inherent to the governing equations of the tension field theory method. The proposed method was considered to be validated, because of the good qualitative and reasonable quantitative agreements between numerical and experimental results.

Summarizing, the convexity properties of the relaxed strain energy function inherently led to an efficient solution method for the minimization of total potential energy. Efficiency was also achieved by the implicit containment of the membrane states in the governing equations. The possibility to apply any material law with a stress-strain relation which is one-to-one, led to a robust method. Additionally the robustness was increased by the governing equations which were in the form a global stiffness matrix and force vector. This allowed implementation in a commercial FEM software and a coupling with other type of elements. Combining these observations with the numerical results, it was shown that a variational formulation of the relaxed strain energy function can be used to obtain a robust and efficient method to model the stress distribution in membranes in the presence of wrinkles.

11-2 Recommendations

Several recommendations to improve the work presented in this thesis and to extend it to other areas are considered in this section. First, the proposed method is least accurate near slack regions in the membrane. Both the stress directions and the membrane deformation in these slack regions are shown to be susceptible to inaccuracies. In highly slacked regions the low effective stiffness may also result in instabilities of the numerical algorithm. Further research is proposed to consider these slack regions in more detail and to address the presented issues whilst still maintaining the mathematical properties of the governing equations.

Secondly, in the current algorithm the stress initialization in the membrane is performed in the same way at the beginning of each step. This stress initialization is based on the stresses computed as if the membrane were a regular shell, however, the initialization may be more efficient when utilizing the membrane stresses at the end of the previous step, as these already indicate e.g. the stress direction. Several attempts were made during the current work to do this, but a stable alternative was not found. Further research may lead to improvements in this process of initializing the membrane stresses.

Thirdly, the results in this thesis have all been obtained using purely displacement controlled loading, except for the pressurized beam. In reality membranes are often reinforced at the edges and the force is applied to these reinforcements, a purely force controlled analysis of the membrane is recommended. Additional challenges of applying force control are e.g. the determination of a realistic force distribution over the edges of the membrane taking into account possible slack regions at these edges.

The presented work can be used as a starting point for future research. As mentioned before, the proposed method is suitable for implementation in a commercial FEM software due to the form of its governing equations. Further research is recommended to enable this implementation and to perform the actual implementation. Activities required for this purpose would include e.g. a detailed patch test of the elements.

Additionally, a research area in which the presented work may be applied is for post-buckling analysis of regular shells. The tension field theory method applied in this thesis can be interpreted as a post-buckling analysis of membranes with zero bending stiffness. Additional research is recommended to investigate the extent to which the tension field theory method can be applied to regular shells after they have buckled. This may include a need to make modifications to the governing equations to allow slight compressive stresses in the post-buckling regime of the shell.

Appendix A

Alternative Convexity Analysis

The conditions for a quasi-convex strain energy with respect to the deformation gradient were presented in Section 3-3. An alternative approach to obtain these conditions is presented in this appendix. This approach is slightly weaker than that given in Section 3-3 as it requires the strain energy function to be continuous in its second derivative.

The approach followed in this appendix is based on the Hessian of the strain energy function, which is presented in Section A-1 for the general case. Conditions for quasi-convexity of the strain energy with respect to the deformation gradient are discussed in Section A-2.

A-1 Hessian Tensor of Strain Energy Function

The condition for a function $f(\boldsymbol{X})$ to be convex is given in Equation (3-27). By letting $\boldsymbol{X}_2 - \boldsymbol{X}_1$ approach zero this condition becomes $\mathsf{H} \geq \boldsymbol{0}$, with H being the Hessian of $f(\boldsymbol{X})$ defined as:

$$\mathsf{H}(\boldsymbol{X}) = \frac{\partial^2 f(\boldsymbol{X})}{\partial \boldsymbol{X} \partial \boldsymbol{X}} \tag{A-1}$$

The Hessian of the strain energy function is derived in this section to formulate the conditions for convexity. The strain energy function is denoted by $\psi(\boldsymbol{F}) = \phi(\boldsymbol{E}(\boldsymbol{F})) = \phi(\boldsymbol{E})$ in which $\boldsymbol{F}$ is the deformation gradient, usually represented by its mixed components F^i_α. The Green-Lagrange strain tensor $\boldsymbol{E}$ is defined as:

$$\boldsymbol{E} = \frac{1}{2}\left(\boldsymbol{F}^T\boldsymbol{F} - \boldsymbol{I}\right) \tag{A-2}$$

which in index notation becomes:

$$2E_{\alpha\beta} = g_{ij}F^i_\alpha F^j_\beta - \delta_{\alpha\beta} \tag{A-3}$$

Note that Greek indices are used to denote the reference configuration of the membrane, whereas Latin indices indicate the current configuration. From its definition it follows that

$\boldsymbol{E}$ is a symmetric tensor, meaning $E_{\alpha\beta} = E_{\beta\alpha}$. The first and second Piola-Kirchhoff stress tensors, $\boldsymbol{P}$ and $\boldsymbol{S}$ respectively, are defined as the derivatives of the strain energy function:

$$\boldsymbol{P} = \frac{\partial \psi(\boldsymbol{F})}{\partial \boldsymbol{F}}; \qquad \boldsymbol{S} = \frac{\partial \phi(\boldsymbol{E})}{\partial \boldsymbol{E}} \tag{A-4}$$

Note that $\boldsymbol{P}$ represents the force per unit reference area of the membrane whereas $\boldsymbol{S}$ does not have a direct physical meaning. The stress tensor $\boldsymbol{S}$ is a symmetric matrix which follows from the symmetry of the Green-Lagrange strain tensor $\boldsymbol{E}$.

The relation between the first and second Piola-Kirchhoff stress tensors is derived in Equation (A-5):

$$\begin{aligned} P_i^\alpha &= \frac{\partial \psi}{\partial F_\alpha^i} \\ &= \frac{\partial \phi}{\partial E_{\beta\gamma}} \frac{\partial E_{\beta\gamma}}{\partial F_\alpha^i} \\ &= S^{\beta\gamma} \frac{1}{2} \frac{\partial F_{j\beta} F_\gamma^j - \delta_{\beta\gamma}}{\partial F_\alpha^i} \\ &= \frac{1}{2} S^{\beta\gamma} \left(\frac{\partial F_{j\beta}}{\partial F_\alpha^i} F_\gamma^j + \frac{\partial F_\gamma^j}{\partial F_\alpha^i} F_{j\beta} \right) \\ &= \frac{1}{2} S^{\beta\gamma} \left(\delta_{ij} \delta_\beta^\alpha F_\gamma^j + \delta_i^j \delta_\gamma^\alpha F_{j\beta} \right) \\ &= \frac{1}{2} \left(S^{\alpha\gamma} F_{i\gamma} + S^{\alpha\beta} F_{i\beta} \right) \\ &= F_{i\gamma} S^{\alpha\gamma} = F_{i\gamma} S^{\gamma\alpha} = \boldsymbol{F}\boldsymbol{S} \end{aligned} \tag{A-5}$$

With this relation the Hessian of the strain energy function is derived from its definition:

$$\mathsf{H} = \frac{\partial^2 \psi}{\partial \boldsymbol{F} \partial \boldsymbol{F}} = \frac{\partial \boldsymbol{P}}{\partial \boldsymbol{F}} \tag{A-6}$$

The Hessian H is a fourth order tensor since both $\boldsymbol{P}$ and $\boldsymbol{F}$ are tensors of second order. Substitution of Equation (A-5) into the definition of the Hessian yields:

$$\begin{aligned} H_{ij}^{\alpha\beta} = \frac{\partial P_i^\alpha}{\partial F_\beta^j} &= \frac{\partial F_{i\gamma} S^{\alpha\gamma}}{\partial F_\beta^j} \\ &= \underbrace{\frac{\partial F_{i\gamma}}{\partial F_\beta^j} S^{\alpha\gamma}}_{I} + \underbrace{F_{i\gamma} \frac{\partial S^{\alpha\gamma}}{\partial F_\beta^j}}_{II} \end{aligned} \tag{A-7}$$

The first part of this expression is rewritten as:

$$I: \qquad \frac{\partial F_{i\gamma}}{\partial F_\beta^j} S^{\alpha\gamma} = \delta_{ij} \delta_\gamma^\beta S^{\alpha\gamma} = S^{\alpha\beta} \delta_{ij} \tag{A-8}$$

and the second part of Equation (A-7) is:

$$
\begin{aligned}
II: \qquad F_{i\gamma}\frac{\partial S^{\alpha\gamma}}{\partial F^j_\beta} &= F_{i\gamma}\frac{\partial S^{\alpha\gamma}}{\partial E_{\delta\theta}}\frac{\partial E_{\delta\theta}}{\partial F^j_\beta} \\
&= F_{i\gamma}C^{\alpha\gamma\delta\theta}\frac{1}{2}\left(F_{j\theta}\delta^\beta_\delta + F_{j\delta}\delta^\beta_\theta\right) \\
&= \frac{1}{2}F_{i\gamma}\left(C^{\alpha\gamma\beta\theta}F_{j\theta} + C^{\alpha\gamma\delta\beta}F_{j\delta}\right) \\
&= \frac{1}{2}F_{i\gamma}\left(C^{\alpha\gamma\beta\theta}F_{j\theta} + C^{\alpha\gamma\beta\delta}F_{j\delta}\right) \qquad \text{(Symmetry)} \\
&= C^{\alpha\gamma\beta\delta}F_{i\gamma}F_{j\delta} \qquad \text{(A-9)}
\end{aligned}
$$

C is the fourth order stiffness tensor which, because of its definition, is symmetric within its first and last two indices: $C^{\alpha\gamma\beta\delta} = C^{\gamma\alpha\beta\delta} = C^{\alpha\gamma\delta\beta}$. Substitution of the results into Equation (A-7) gives the Hessian H of the strain energy function to be:

$$H^{\alpha\beta}_{ij} = S^{\alpha\beta}\delta_{ij} + C^{\alpha\gamma\beta\delta}F_{i\gamma}F_{j\delta} \qquad \text{(A-10)}$$

A-2 Convexity Conditions

The minimization of the strain energy function is stable when it is at least quasi-convex in the deformation gradient [25]. The sufficient and necessary conditions for this quasi-convexity are presented in this section.

A-2-1 Convexity

The strain energy is convex if the Hessian H is a positive semi-definite (spd) tensor, which means that for any A^i_α and A^j_β it must hold that:

$$H^{\alpha\beta}_{ij}A^i_\alpha A^j_\beta \geq 0 \qquad \text{(A-11)}$$

Using Equation (A-7) this can be rewritten to be:

$$
\begin{aligned}
S^{\alpha\beta}\delta_{ij}A^i_\alpha A^j_\beta + C^{\alpha\gamma\beta\delta}F_{i\gamma}F_{j\delta}A^i_\alpha A^j_\beta &\geq 0 \\
S^{\alpha\beta}A^i_\alpha A_{i\beta} + C^{\alpha\gamma\beta\delta}B_{\gamma\alpha}B_{\delta\beta} &\geq 0 \qquad \text{(A-12)}
\end{aligned}
$$

in which $\boldsymbol{B} = \boldsymbol{F}^T\boldsymbol{A}$, which is the pull-back of $\boldsymbol{A}$ from the current to the reference configuration. Note that $S^{\alpha\beta}A^i_\alpha A_{j\beta} = \mathrm{tr}\boldsymbol{A}\boldsymbol{S}\boldsymbol{A}^T$.

As $\boldsymbol{A}$, and consequently $\boldsymbol{B}$, are arbitrary, the sufficient conditions for $\psi(\boldsymbol{F})$ to be convex are:

1. $\boldsymbol{S} \geq \boldsymbol{0}$, meaning that the stresses are non-compressive.
2. $\mathsf{C} \geq \boldsymbol{0}$, meaning that the stiffness tensor is spd.

A-2-2 Rank-One Convexity

A weaker form of convexity is rank-one convexity, for which A^i_α in Equation (A-11) is rank-one:

$$A^i_\alpha = u^i e_\alpha \tag{A-13}$$

Substituting this expression into Equation (A-12) yields the Legendre-Hadamard condition:

$$\begin{aligned} S^{\alpha\beta} e_\alpha e_\beta u^i u_i + C^{\alpha\gamma\beta\delta} e_\alpha v_\gamma e_\beta v_\delta \geq 0 \\ S^{\alpha\beta} e_\alpha e_\beta + C^{\alpha\gamma\beta\delta} e_\alpha v_\gamma e_\beta v_\delta \geq 0 \end{aligned} \tag{A-14}$$

in which $\boldsymbol{v} = \boldsymbol{F}^T \boldsymbol{u}$ is the pull-back of the vector $\boldsymbol{u}$ from the current into the reference configuration. As mentioned in Section 3-3 and shown in Chapter 4 the deformation gradient $\boldsymbol{F}$ is represented by a 3×2 matrix. As a result the vector $\boldsymbol{v} = \boldsymbol{F}^T \boldsymbol{u}$ equals zero when the vector $\boldsymbol{u}$ is chosen normal to the current configuration of the membrane. For this choice of $\boldsymbol{u}$ Equation (A-14) becomes:

$$S^{\alpha\beta} e_\alpha e_\beta \geq 0 \tag{A-15}$$

which is the necessary condition for the strain energy function in membranes to be rank-one convex. It states that $\boldsymbol{S} \geq \boldsymbol{0}$, meaning the stresses are non-compressive.

A-2-3 Quasi-Convexity

A stable solution of the equations of equilibrium exists when the strain energy is quasi-convex with respect to the deformation gradient [25], which is a weaker form than convexity, but at least as strong as rank-one convexity [33]. This means that for stable solutions to exist the strain energy function needs to be at least rank-one convex and it is sufficient to be convex. Combining this with the results from previous sections it is concluded that for membranes:

- sufficient conditions for quasi-convexity are $\boldsymbol{S} \geq \boldsymbol{0}$ and $\mathsf{C} \geq \boldsymbol{0}$. The former condition is equivalent to a non-decreasing $\phi(\boldsymbol{E})$ and the second condition is equivalent to a convex $\phi(\boldsymbol{E})$.
- necessary condition for quasi-convexity is $\boldsymbol{S} \geq \boldsymbol{0}$, which is equivalent to a non-decreasing strain energy function $\phi(\boldsymbol{E})$.

These sufficient and necessary conditions form an alternative proof of Proposition 3.3 which states that the relaxed strain energy function is the quasi-convexification of $\psi(\boldsymbol{F})$.

Appendix B

Finite Element Matrices

The components of several matrices for the triangular and quadrilateral elements are presented in this appendix. These matrices are obtained from their expressions presented in previous chapters.

B-1 2D Triangular Elements

$$\boldsymbol{B}_L = \begin{bmatrix} y_{23} & 0 & y_{31} & 0 & y_{12} & 0 \\ 0 & x_{32} & 0 & x_{13} & 0 & x_{21} \\ x_{32} & y_{23} & x_{13} & y_{31} & x_{21} & y_{12} \end{bmatrix} \tag{B-1}$$

with $x_{ij} = x_i - x_j$ and $y_{ij} = y_i - y_j$.

$$\boldsymbol{P}_1 = \frac{1}{4A^2} \begin{bmatrix} y_{23}^2 & 0 & y_{23}y_{31} & 0 & y_{12}y_{23} & 0 \\ & y_{23}^2 & 0 & y_{23}y_{31} & 0 & y_{12}y_{23} \\ & & y_{31}^2 & 0 & y_{12}y_{31} & 0 \\ & & & y_{31}^2 & 0 & y_{12}y_{31} \\ & symm & & & y_{12}^2 & 0 \\ & & & & & y_{12}^2 \end{bmatrix} \tag{B-2}$$

$$\boldsymbol{P}_2 = \frac{1}{4A^2} \begin{bmatrix} x_{32}^2 & 0 & x_{32}x_{13} & 0 & x_{21}x_{32} & 0 \\ & x_{32}^2 & 0 & x_{32}x_{13} & 0 & x_{21}x_{32} \\ & & x_{13}^2 & 0 & x_{21}x_{13} & 0 \\ & & & x_{13}^2 & 0 & x_{21}x_{13} \\ & symm & & & x_{21}^2 & 0 \\ & & & & & x_{21}^2 \end{bmatrix} \tag{B-3}$$

$$\boldsymbol{P}_{12} = \frac{1}{4A^2}\begin{bmatrix} (xy)_{32,23} & 0 & (xy)_{13,23} & 0 & (xy)_{21,23} & 0 & \\ & (xy)_{32,23} & 0 & (xy)_{13,23} & 0 & (xy)_{21,23} & \\ & & & (xy)_{13,31} & 0 & (xy)_{13,12} & 0 \\ & & & & (xy)_{13,31} & 0 & (xy)_{13,12} \\ & symm & & & & (xy)_{21,12} & 0 \\ & & & & & & (xy)_{21,12} \end{bmatrix} \tag{B-4}$$

with $(xy)_{ij,kl} = x_{ij}y_{kl} + x_{lk}y_{ji}$.

B-2 2D Quadrilateral Elements

$$\frac{\partial \boldsymbol{N}}{\partial r} = \frac{1}{4}\begin{bmatrix} s-1 & 0 & 1-s & 0 & s+1 & 0 & -s-1 & 0 \\ 0 & s-1 & 0 & 1-s & 0 & s+1 & 0 & -s-1 \end{bmatrix} \tag{B-5a}$$

$$\frac{\partial \boldsymbol{N}}{\partial s} = \frac{1}{4}\begin{bmatrix} r-1 & 0 & -r-1 & 0 & r+1 & 0 & 1-r & 0 \\ 0 & r-1 & 0 & -r-1 & 0 & r+1 & 0 & 1-r \end{bmatrix} \tag{B-5b}$$

For the hybrid element:

$$\boldsymbol{P}_e = \begin{bmatrix} \frac{J_1}{J_{12}} & 0 & 0 & \frac{J_2}{J_{12}} & 0 & 0 & 0 & 0 & 0 & 0 & 0 & 0 \\ 0 & \frac{J_1}{J_{14}} & 0 & 0 & 0 & 0 & 0 & 0 & 0 & 0 & \frac{J_4}{J_{14}} & 0 \\ 0 & 0 & \frac{J_1}{J_{1234}} & 0 & 0 & \frac{J_2}{J_{1234}} & 0 & 0 & \frac{J_3}{J_{1234}} & 0 & 0 & \frac{J_4}{J_{1234}} \\ \frac{J_1}{J_{12}} & 0 & 0 & \frac{J_2}{J_{12}} & 0 & 0 & 0 & 0 & 0 & 0 & 0 & 0 \\ 0 & 0 & 0 & 0 & \frac{J_2}{J_{23}} & 0 & 0 & \frac{J_3}{J_{23}} & 0 & 0 & 0 & 0 \\ 0 & 0 & \frac{J_1}{J_{1234}} & 0 & 0 & \frac{J_2}{J_{1234}} & 0 & 0 & \frac{J_3}{J_{1234}} & 0 & 0 & \frac{J_4}{J_{1234}} \\ 0 & 0 & 0 & 0 & 0 & 0 & \frac{J_3}{J_{34}} & 0 & 0 & \frac{J_4}{J_{34}} & 0 & 0 \\ 0 & 0 & 0 & 0 & \frac{J_2}{J_{23}} & 0 & 0 & \frac{J_3}{J_{23}} & 0 & 0 & 0 & 0 \\ 0 & 0 & \frac{J_1}{J_{1234}} & 0 & 0 & \frac{J_2}{J_{1234}} & 0 & 0 & \frac{J_3}{J_{1234}} & 0 & 0 & \frac{J_4}{J_{1234}} \\ 0 & 0 & 0 & 0 & 0 & 0 & \frac{J_3}{J_{34}} & 0 & 0 & \frac{J_4}{J_{34}} & 0 & 0 \\ 0 & \frac{J_1}{J_{14}} & 0 & 0 & 0 & 0 & 0 & 0 & 0 & 0 & \frac{J_4}{J_{14}} & 0 \\ 0 & 0 & \frac{J_1}{J_{1234}} & 0 & 0 & \frac{J_2}{J_{1234}} & 0 & 0 & \frac{J_3}{J_{1234}} & 0 & 0 & \frac{J_4}{J_{1234}} \end{bmatrix} \tag{B-6}$$

with $J_i = \det \boldsymbol{J}_i$, in which $i = 1..4$ is the index of the integration point, $J_{ij} = J_i + J_j$ and $J_{ijkl} = J_i + J_j + J_k + J_l$.

Appendix C

Mansfield Solution

The analytical solution of the tension field for a rectangular membrane under shear and tension loading is presented in this appendix. This solution includes the stresses, strains and strain energy in the membrane and it has been presented by Mansfield [14, 15] along with solutions for more general membrane shapes and loading in $\mathbb{R}^2$. The solution presented in this appendix is slightly different from the Mansfield solution because the symmetry of the tension field in the membrane is exploited. Note that the analytical solution assumes a linear elastic stress-strain relation.

Tension ray lines in a membrane under shear and tension displacements, u and v respectively, are shown in Figure C-1. The bottom edge of the membrane is clamped.

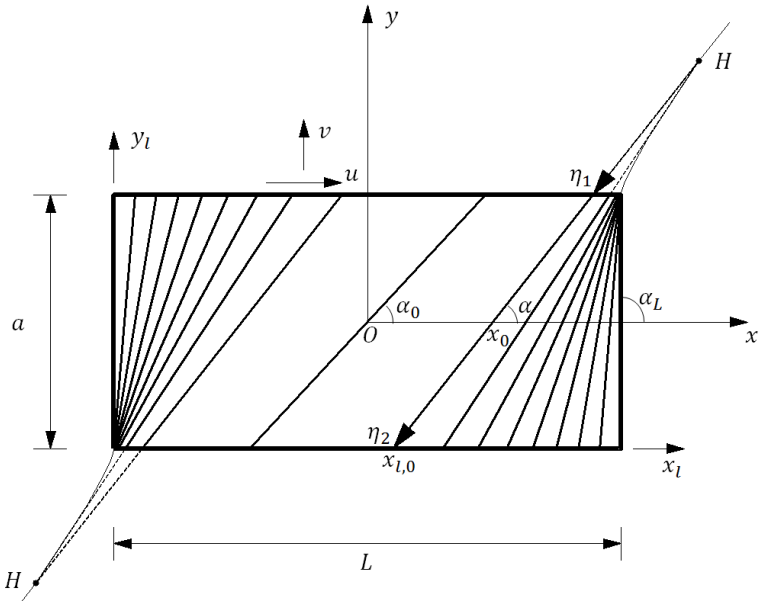

Figure C-1: Tension ray lines in membrane under shear loading.

Mansfield [15] shows that the tension rays in the membrane are straight and that two neighboring rays intersect in the locus point H. This point is not fixed but moves along the thin curved path depicted in Figure C-1. Note that the tension ray angle starts at $\alpha = \alpha_L$, which equals $\pi/2$ for a rectangular membrane, at the left edge, then decreases to α_0 in the center and increases to α_L again at the right edge of the membrane. This symmetry is used in the derivations of the equations in this appendix, which means that only the part of the membrane at the right of the tension ray with $\alpha = \alpha_0$ needs to be considered. This region is referred to as the right part of the membrane. In the derivations the x, y coordinate system is applied, whereas Mansfield uses the x_l, y_l coordinate system [14].

The parameters η_1 and η_2 in Figure C-1 represent the distance of the locus point H towards the edges of the membrane. Any point in the membrane can be identified by its x, y coordinates or by its $x_0(\alpha), \eta$ coordinates, in which $x_0(\alpha)$ is the x-coordinate of the intersection of a tension ray with the x-axis. The relation between x_0 and α is the first point of consideration. Define μ as:

$$\mu = \frac{\eta_1}{\eta_2} \tag{C-1}$$

and let α^* be the tension ray angle as a result from u and v in an infinite membrane. Using classical mechanics and assuming without loss of generality than $u > 0$, the expression for α^* is given as shown in Equation (C-2):

$$\tan 2\left(\alpha^* - \frac{\pi}{2}\right) = -\frac{u}{v} \qquad \Rightarrow \qquad \alpha^* = -\frac{1}{2}\tan^{-1}\left(\frac{u}{v}\right) + \frac{\pi}{2} \tag{C-2}$$

Assume that the displacement u, v is applied under an angle γ with the x-axis, meaning:

$$\tan\gamma = \frac{v}{u} \qquad \Rightarrow \qquad \gamma = \tan^{-1}\left(\frac{v}{u}\right) = 2\alpha^* - \frac{\pi}{2} \tag{C-3}$$

The applied displacement along a tension ray with angle α is denoted as Δ_α. Using the definitions of γ and α^* this displacement can be expressed as shown in Equation (C-4):

$$\begin{aligned}
\Delta_\alpha &= u\cos\alpha + v\sin\alpha \\
&= \hat{u}\left(\cos\gamma\cos\alpha + \sin\gamma\sin\alpha\right) \\
&= \hat{u}\cos\left(\alpha - \gamma\right) \\
&= \hat{u}\cos\left(\alpha - 2\alpha^* + \frac{\pi}{2}\right) \\
&= \hat{u}\sin\left(2\alpha^* - \alpha\right)
\end{aligned} \tag{C-4}$$

in which:

$$\hat{u}^2 = u^2 + v^2 \tag{C-5}$$

Next the function F is defined which, when integrated over the range of α, gives a measure for the strain energy in the membrane:

$$F = \frac{\Delta_\alpha^2}{-\ln\mu} = \frac{\hat{u}^2\sin^2\left(2\alpha^* - \alpha\right)}{-\ln\mu} \tag{C-6}$$

Note that this function only holds in the right part of the membrane, which is considered in these derivations. To find the relation between x_0 and α, first the relation between the two coordinate systems x, y and x_l, y_l is needed. From Figure C-1 it follows:

$$x_0 = x_{l,0} + \frac{a}{2}\left(1 + \cot\alpha\right) \tag{C-7}$$

Hence:

$$\frac{dx_0}{d\alpha} = x_0' = x_{l,0}' - \frac{a}{2}\text{cosec}^2\alpha \tag{C-8}$$

Mansfield [14] shows the relation between μ and $x_{l,0}'$ to be as shown in Equation (C-9):

$$\mu = 1 - \frac{a\text{cosec}^2\alpha}{x_{l,0}'} = 1 - \frac{a\text{cosec}^2\alpha}{x_0' + \frac{a}{2}\text{cosec}^2\alpha} \tag{C-9}$$

Solving for x_0' gives:

$$x_0' = \frac{a}{2}\text{cosec}^2\alpha\left(\frac{1+\mu}{1-\mu}\right) \tag{C-10}$$

After integrating this expression the relation between x_0 and α is obtained:

$$x_0 = \frac{a}{2}\int_{\alpha_0}^{\alpha}\text{cosec}^2\alpha\left(\frac{1+\mu}{1-\mu}\right)d\alpha \tag{C-11}$$

It should be noted that α_0 is not known beforehand, but can be determined by substituting that if $\alpha = \alpha_L$ then $x_0 = L/2$ (see Figure C-1). The parameter μ is also not known yet and in fact depends on α. Physically, the relation between μ and α represents the change in value of α along x. From Figure C-1 and Equation (C-1) it follows that if for a tension ray α, $\mu = 1$ it means that the locus point H is at infinite distance and hence the tension ray is parallel to its neighbors. For $\mu < 1$ the tension rays are non-parallel. The relation between μ and α is obtained by solving Equation (C-12) [14]:

$$\frac{dF}{dx_0'} = C \tag{C-12}$$

in which C is an unknown constant. Applying the chain rule and using Equations (C-9) and (C-10) this equation can be rewritten to be:

$$\begin{aligned}\frac{dF}{dx_0'} &= \frac{dF}{d\mu}\frac{d\mu}{dx_0'} \\ &= \frac{\Delta_\alpha^2}{\mu\left(\ln\mu\right)^2}\cdot\frac{\sin^2\alpha}{a}\left(1-\mu\right)^2 = C\end{aligned} \tag{C-13}$$

After rewriting and by using Equation (C-4) this becomes:

$$C\mu\left(\frac{\ln\mu}{1-\mu}\right)^2 = \frac{\Delta_\alpha^2}{a}\sin^2\alpha = \frac{\hat{u}^2}{a}\sin^2\left(2\alpha^* - \alpha\right)\sin^2\alpha \tag{C-14}$$

To compute C one should note from Figure C-1 that if $\alpha = \alpha_0$ then $\frac{d\alpha}{dx_0} = 0$ and hence $x_0' = \infty$ in the limit. According to Equation (C-9) this gives $\mu = 1$, which means that the tension rays are parallel at $\alpha = \alpha_0$. Using l'Hospital's rule one can show that for $\alpha = \alpha_0$ the left hand side of Equation (C-14) becomes equal to C and hence:

$$C = \frac{\hat{u}^2}{a}\sin^2\left(2\alpha^* - \alpha_0\right)\sin^2\alpha_0 \tag{C-15}$$

Substituting this result into Equation (C-14) gives the final relation between μ and α as shown in Equation (C-16):

$$\mu\left(\frac{\ln\mu}{1-\mu}\right)^2 = \frac{\sin^2\left(2\alpha^* - \alpha\right)\sin^2\alpha}{\sin^2\left(2\alpha^* - \alpha_0\right)\sin^2\alpha_0} \tag{C-16}$$

Solving this equation is done numerically by applying Newtons method to find the roots of the function $f(\mu)$:

$$f(\mu) = \mu \left(\frac{\ln \mu}{1-\mu} \right)^2 - \frac{\sin^2(2\alpha^* - \alpha) \sin^2 \alpha}{\sin^2(2\alpha^* - \alpha_0) \sin^2 \alpha_0} \tag{C-17a}$$

$$f'(\mu) = \left(\frac{\ln \mu}{1-\mu} \right)^2 \left[1 + \frac{2}{\mu+1} + \frac{2\mu}{1-\mu} \right] \tag{C-17b}$$

With this the relation between x_0 and α has been fully established. For a given α the value for μ is found by solving Equation (C-16) after which the value for x_0 is computed using Equation (C-11). The integration in this equation is evaluated efficiently using the Romberg integration method [5].

In the following, instead of obtaining x_0 from α, the other way around is required. This is achieved by applying the bisection method which computes a lower and upper bound for x_0 and squeezes them together. The value of α which is then between the two bounds also gives the value for μ by Equation (C-16).

The tension field theory assumes that the stresses in the membrane are parallel to the tension ray. For this reason the stress is denoted by σ_η and the corresponding strain is ε_η. This strain is computed as shown in Equation (C-18) [14]:

$$\varepsilon_\eta = \frac{\Delta_\alpha}{-\eta \ln \mu} = \frac{\hat{u} \sin(2\alpha^* - \alpha)}{-\eta \ln \mu} \tag{C-18}$$

To apply this equation for a given x, y location, first x_0 needs to be computed, which is done by assuming an initial value for x_0 and computing the corresponding α. Then the distance from the x, y coordinates to this tension ray is computed after which an iterative procedure is applied to find the x_0 for which this distance equals 0. From this x_0 the value for μ is computed using the procedure as explained above.

Next, the η coordinate is required in order to apply Equation (C-18). This parameter represents the location of the x, y coordinates on the tension ray which was just found. The value for η is computed from Figure C-1 as:

$$\begin{aligned} \eta &= -\frac{2y}{a} \left(\frac{\eta_2 - \eta_1}{2} \right) + \left(\frac{\eta_2 + \eta_1}{2} \right) \\ &= -\frac{2y}{a} \eta_2 \left(\frac{1-\mu}{2} \right) + \eta_2 \left(\frac{1+\mu}{2} \right) \end{aligned} \tag{C-19}$$

A result from Mansfield [14] combined with Equations (C-8) (C-10) gives the relation between η_2 and μ as:

$$\eta_2 = x'_{l,0} \sin \alpha = a \operatorname{cosec} \alpha \left(\frac{1}{1-\mu} \right) \tag{C-20}$$

Substituting this into Equation (C-19) yields:

$$\eta = \operatorname{cosec} \alpha \left[-y + \frac{a}{2} \left(\frac{1+\mu}{1-\mu} \right) \right] \tag{C-21}$$

With this result the strain is computed by substitution into Equation (C-18) to be:

$$\varepsilon_\eta = \frac{\hat{u} \sin(2\alpha^* - \alpha) \sin \alpha}{\left[y - \frac{a}{2} \left(\frac{1+\mu}{1-\mu} \right) \right] \ln \mu} \tag{C-22}$$

Using the linear-elastic stress strain relation assumed by Mansfield [14] the stress σ_η is computed as shown in Equation (C-23):

$$\sigma_\eta = E\varepsilon_\eta \tag{C-23}$$

in which E is the Young's modulus. Finally the strain energy ϕ is computed from the definition of the potential function F [14] as shown in Equation (C-24):

$$\phi = \frac{1}{2}Et \cdot 2\int_{\alpha_0}^{\alpha_L} F d\alpha = Et\hat{u}^2 \int_{\alpha_0}^{\alpha_L} \frac{\sin^2(2\alpha^* - \alpha)}{-\ln \mu} d\alpha \tag{C-24}$$

Note that the '2' appears because the strain in the right part of the membrane has to be multiplied by two to obtain the total strain energy in the membrane. Equation (C-24) is evaluated using the Romberg integration method.

Bibliography

[1] Akita, T., Nakashino, K., Natori, M. C., and Park, K. C. A simple computer implementation of membrane wrinkle behaviour via a projection technique. *International Journal for Numerical Methods in Engineering 71*, 10 (2007), 1231–1259.

[2] Ball, J. M. Strict convexity, strong ellipticity, and regularity in the calculus of variations. *Mathematical Proceedings of the Cambridge Philosophical Society 87*, 03 (1980), 501–513.

[3] Bonet, J., and Wood, R. *Nonlinear Continuum Mechanics for Finite Element Analysis*. Cambridge University Press, 2008.

[4] Boyd, S., and Vandenberghe, L. *Convex Optimization*. Cambridge University Press, New York, NY, USA, 2004.

[5] Burden, R., and Faires, J. *Numerical Analysis*. Brooks/Cole, 2010.

[6] Cottrell, J., Hughes, T., and Bazilevs, Y. *Isogeometric Analysis: Toward Integration of CAD and FEA*. Wiley, 2009.

[7] Epstein, M. On the wrinkling of anisotropic elastic membranes. *Journal of Elasticity 55*, 2 (1999), 99–109.

[8] Flores, F. G., and Oñate, E. Wrinkling and folding analysis of elastic membranes using an enhanced rotation-free thin shell triangular element. *Finite Elements in Analysis and Design 47*, 9 (2011).

[9] Fujisawa, K., Kojima, M., Nakata, K., and Yamashita, M. Sdpa (semidefinite programming algorithm) – user's manual. Tech. rep., Tokyo Institute of Technology, 1995.

[10] Haseganu, E., and Steigmann, D. Analysis of partly wrinkled membranes by the method of dynamic relaxation. *Computational Mechanics 14*, 6 (1994), 596–614.

[11] Jarasjarungkiat, A., Wüchner, R., and Bletzinger, K. . Efficient sub-grid scale modeling of membrane wrinkling by a projection method. *Computer Methods in Applied Mechanics and Engineering 198*, 9-12 (2009), 1097–1116.

[12] Kang, S., and Im, S. Finite element analysis of dynamic response of wrinkling membranes. *Computer Methods in Applied Mechanics and Engineering 173*, 1Ű2 (1999), 227 – 240.

[13] Lebedev, L., Cloud, M., and Eremeyev, V. *Tensor Analysis with Applications in Mechanics*. World Scientific Publishing Company, Incorporated, 2010.

[14] Mansfield, E. H. Load transfer via a wrinkled membrane. *Proceedings of the Royal Society of London. Series A, Mathematical and Physical Sciences 316*, 1525 (1970), pp. 269–289.

[15] Mansfield, E. H. Analysis of wrinkled membranes with anisotropic and nonlinear elastic properties. *Proc R Soc London Ser A 353*, 1975 (1977), 475–498.

[16] Marsden, J., and Hughes, T. *Mathematical Foundations of Elasticity*. Dover Civil and Mechanical Engineering Series. DOVER PUBN Incorporated, 1994.

[17] Mehrotra, S. On the implementation of a primal-dual interior point method. *SIAM Journal on Optimization 2*, 4 (1992), 575–601.

[18] Miyazaki, Y. Wrinkle/slack model and finite element dynamics of membrane. *International Journal for Numerical Methods in Engineering 66*, 7 (2006), 1179–1209.

[19] Mosler, J., and Cirak, F. A variational formulation for finite deformation wrinkling analysis of inelastic membranes. *Computer Methods in Applied Mechanics and Engineering 198*, 27-29 (2009), 2087–2098.

[20] Nguyen, V. P., Simpson, R. N., Bordas, S. P. A., and Rabczuk, T. An introduction to isogeometric analysis with matlab® implementation: Fem and xfem formulations. *CoRR abs/1205.2129* (2012).

[21] Pagitz, M., and Abdalla, M. Simulation of tension fields with in-plane rotational degrees of freedom. *Computational Mechanics 46*, 5 (2010), 747–757.

[22] Pian, T. H., and Chen, D. P. Alternative ways for formulation of hybrid stress element. *International Journal for Numerical Methods in Engineering 18*, 11 (1982), 1679–1684.

[23] Piegl, L., and Tiller, W. *The NURBS Book*. Monographs in visual communications. Springer-Verlag GmbH, 1997.

[24] Pipkin, A. C. Relaxed energy densities for small deformations of membranes. *IMA Journal of Applied Mathematics (Institute of Mathematics and Its Applications) 50*, 3 (1993), 225–237.

[25] Pipkin, A. C. Relaxed energy densities for large deformations of membranes. *IMA Journal of Applied Mathematics (Institute of Mathematics and Its Applications) 52*, 3 (1994), 297–308.

[26] Puntel, E., Deseri, L., and Fried, E. Wrinkling of a stretched thin sheet. *Journal of Elasticity 105*, 1-2 (2011), 137–170.

[27] Raible, T., Tegeler, K., Löhnert, S., and Wriggers, P. Development of a wrinkling algorithm for orthotropic membrane materials. *Computer Methods in Applied Mechanics and Engineering 194*, 21-24 SPEC. ISS. (2005), 2550–2568.

[28] Rockafellar, R. *Convex analysis*. Princeton mathematical series. PRINCETON University Press, 1997.

[29] Roddeman, D., Drukker, J., Oomens, C., and Janssen, J. The wrinkling of thin membranes: Part i - theory. *Journal of Applied Mechanics 54*, 4 (1987), 884–887.

[30] Rumpel, T., and Schweizerhof, K. Volume-dependent pressure loading and its influence on the stability of structures. *International Journal for Numerical Methods in Engineering 56*, 2 (2003), 211–238.

[31] Sansour, C., and Kollmann, F. G. Families of 4-node and 9-node finite elements for a finite deformation shell theory. an assessment of hybrid stress, hybrid strain and enhanced strain elements. *Computational Mechanics 24*, 6 (2000), 435–447.

[32] Schoop, H., Taenzer, L., and Hornig, J. Wrinkling of nonlinear membranes. *Computational Mechanics 29*, 1 (2002), 68–74.

[33] Schröder, J., and Neff, P. *Poly-, Quasi- and Rank-One Convexity in Applied Mechanics*. Springer, 2010.

[34] Steigmann, D. J. Tension-field theory. *Proceedings of the Royal Society of London. Series A, Mathematical and Physical Sciences 429*, 1876 (1990), 141–173.

[35] Vandenberghe, L., and Boyd, S. Semidefinite programming. *SIAM Review 38* (1994), 49–95.

[36] Veldman, S. *Design And Analysis Methodologies for Inflated Beams*. DUP Science, 2005.

[37] Vella, D., Ajdari, A., Vaziri, A., and Boudaoud, A. Wrinkling of pressurized elastic shells. *Physical Review Letters 107*, 17 (2011).

[38] Wagner, H. Ebene blechwandträger mit dünnem stegblech. *Zeitschrift fur Flugtechnik Motorluftschiffahrt 20* (1929), 200–314.

[39] Washizu, K. *Variational methods in elasticity and plasticity*. Pergamon Press, 1982.

[40] Weinberg, K., and Neff, P. A geometrically exact thin membrane model - investigation of large deformations and wrinkling. *International Journal for Numerical Methods in Engineering 74*, 6 (2008), 871–893.

[41] Yamashita, M., Fujisawa, K., and Kojima, M. Implementation and evaluation of sdpa 6.0 (semidefinite programming algorithm 6.0). *Optimization Methods and Software 18*, 4 II (2003), 491–505.

[42] Zielke, G. Inversion of modified symmetric matrices. *Journal of the ACM 15*, 3 (July 1968), 402–408.